High Speed Field Oriented Control

AALBORG UNIVERSITET

Board of Studies of Energy

Title:	High Speed Field Oriented Control
Semester:	4th
Semester theme:	Master Thesis
Project period:	01.02.09 to 03.06.09
ECTS:	30
Supervisor:	Kaiyuan Lu
Project group:	PED4-1037

Paweł Stopa

SYNOPSIS:

Presented project focuses on deriving the control algorithm capable of applying it on high speed drive. Introductory analysis allows to show advantages of field oriented control strategy over other control methods. Specific character of high frequency drive and chosen SFOC requests two estimators: for stator flux, and rotational speed. They are included in the design process. Derived algorithm is tested in the simulation. Afterwards, experiments were done with the induction drive.

Lack of the high speed motor at the university laboratory, ends up with adjusting it on the conventional induction motor, supplied with $50Hz$. Eventually, properly working control algorithm would be applied on the high frequency motor, available in Danfoss laboratory. Nevertheless, due to the time limitation, it could not be tested with the objective machine. Therefore, all the conclusions are drawn on basis of tests obtained with the conventional motor.

Copies:	- 3
Pages, total:	- 93
Appendix:	- 3
Supplements:	- 3xCD

Preface

The presented project is done at the Institute of Energy Technology of Aalborg University, and is submitted as Master Thesis. The topic, *'High Speed Field Oriented Control'*, is originally proposed by Danfoss Drives.

It has been observed, that motors operated with higher speeds, generally show improved efficiency. Therefore, proper machine controlling at high speed is an important topic. Literature research allows to distinguish the optimal control solution. Field oriented control presents benefits over other possibilities. Additionally, scope is narrowed to orientation with the stator flux. That choice requires two estimators: actual rotational speed (to fulfil sensorless demand), and the stator flux. The algorithm is designed for an asynchronous motor. Due to the limitation, it could not be tested with the objective machine.

The project is done by one-person group. Through the entire period, subject has been divided into three visible parts: problem analysis, modelling and experimental verification. However, not all of the objectives have been fulfilled. It results in developing additional tests and investigations after thesis submission.

It is crucial to mention about the support given by supervisor - Kaiyuan Lu. His suggestions and advices many times allowed the work to be proceeded. Additionally, hints given by Steffan Hansen and Radu Lazar from Danfoss Drives helped in formulating and evaluating the stated problem.

Information for the reader

In order to follow presented ideas in the report, some extra information are listed for reading convenience:

- bibliography is referred in brackets, using Vancouver style, for example [1];

- all of the figures, equations and tables are enumarated with respect to chapters;

- complete lists of nomenclature and abbreviations are put before the content;

- appendices contains external information, which are helpful to evaluate given objective;

- every possible data are stored in attached CD.

Picture on the cover presents 'high speed grinding to achieve optimum airfoil tip clearance and engine performance.' (*source: www.aerospace-technology.com*)

<div align="right">

Paweł Stopa,
3rd June 2009, Aalborg

</div>

Summary

The main objective of the project is to design the stator field oriented control algorithm, capable of running sensorless, and being fully applied in high speed drive. Nevertheless, the lack of availability that kind of motor in university laboratories, turns the scope into conventional motor supplied with rated frequency $f_N = 50Hz$. In order to fulfil the given goal, it is divided into subtasks.

Introductory chapter consists of necessary information, needed in further researches and analyses. It starts with brief presentation of advantages of high speed drives, and applications in which they are used. As that drives mostly utilises two types of motors, proper comparison is made. Afterwards, methods review, concerning controlling high speed drives, is made. In order to obtain advantages of the high speed drives, it is necessary to overcome specific problems. They are presented, together with challenges. It completes the presentation of the high speed systems. Subsequently, exact scope of the project is made, together with limitation.

In order to create desired algorithm, it is necessary to represent mathematically system to be controlled. Therefore, in the second chapter mathematical model of the drive is presented. First, necessary assumptions are pointed, then formulas describing the system are expressed. Finally it is built and tested with simple V/f control to validate its correctness.

The exact design procedure begins from short presentation of principles of field oriented control. Later on focus is made on deeper analysis of direct stator field oriented control. Afterwards, design of the control strategy is proceeded. Additionally, to fulfil the sensorless demand, flux observer and speed estimator are introduced. Algorithm designing is ended with simulation results.

In order to assure the correctness of obtained conclusions from modelling and simulation process, derived control algorithm has to be tested in the laboratory. Before, the actual experiments can be described, first testbench is introduced. The description is divided into two parts: hardware and software. Afterwards, required tests are presented together with appropriate comments of the results. In the end, general conclusion of the laboratory work is drawn.

Report ends with overall conclusions and suggestions for future analyses.

Contents

List of Figures

Nomenclature

$k_A(t), k_B(t), k_C(t)$	- arbitrary phase quantities in the natural coordinates (A, B, C)
$\overline{1}, \overline{a}, \overline{a}^2$	- unity vectors
u_s	- stator voltage
U_{dc}	- dc-link voltage
u_A, u_B, u_C	- phase voltages
u_{AB}, u_{BC}, u_{CA}	- line-to-line voltages
u_N	- nominal voltage
u_{RMS}	- RMS voltage
$u_{s\psi}$	- voltage placed after the stator resistance, in the typical equivalent circuit of ind. motor
i_s	- stator current
i_{sN}	- nominal stator current
e	- back electromotive force
ψ_s	- stator flux
ψ_{s0}	- compensated stator flux
ψ_{sN}	- nominal stator flux
$\psi_{s(mach)}$	- stator flux generated inside the machine (simulation case)
ψ_r	- rotor flux
C_{dc}	- dc-link capacitance
R_s, R_r	- stator and rotor resistances, respectively
L_s, L_r, L_m	- stator, rotor and magnetizing inductances, respectively
$L_s^{'}$	- transient inductance
l_σ	- equivalent inductance: $L_\sigma = L_r L_s - L_m^2$
X_s, X_r, X_m	- stator, rotor and magnetizing reactances, respectively
f_{stN}	- nominal stator frequency
$T_{1..6}$	- switches of the inverter (from 1 to 6)
$D_{1..6}$	- diodes to protect switches of the inverter (from 1 to 6)
L_1, L_2, L_3	- three phases
D_A, D_B, D_C	- switching states of inverter legs
M_e	- electromagnetic torque
M_{eN}	- nominal electromagnetic torque
M_l	- load torque
M_k	- breakdown torque
J	- inertia
B	- friction constant
n_r	- rotor rotational speed
n_e	- synchronous rotational speed
p_p	- number of pole pairs
s	- slip
C	- constant value resulting from initial conditions of the integral
f_c	- cut-off frequency (Hz)
f_s	- sampling frequency
f_{pwm}	- switching frequency

f_{fund}	- fundamental frequency
$G_{(plant)}$	- transfer function of the plant
$G_{(ol)}$	- open-loop transfer function
$G_{(cl)}$	- close-loop transfer function
K_p, K_i	- proportional and integral PI ragulator gains, respectively
K_a	- antiwindup gain
p	- Laplace operator
p_{pol}, q_{pol}	- degrees of numerator and denominator polynomials, respectively
M_p	- maximum overshoot
$t_{r(10\%-90\%)}$	- rising time
$t_{s(2\%)}$	- settling time
T_d	- time delay of the transportation lag
T_{pwm}	- switching time period
T_s	- sampling time
T_{sim}	- simulation time
T_s'	- time constant of the plant in d-current control loop
T_ψ	- time constant of the plant in the flux control loop
T_σ	- one of the time constants of the plant in flux control loop: $T_\sigma = L_\sigma/(R_r L_s)$
T_r	- rotor time constant
T_{st}	- stator time constant
T_{ol}^{eq}	- equivalent time constant of the open-loop system
T^{eq}	- equivalent time constant of the control loop
X	- input to high-pass filter in the flux observer structure
Y	- output of high-pass filter in the flux observer structure
Z	- output of the pure integrator in the flux observer structure
$Gain$	- stator flux gain compensator output
$Angle$	- stator flux position compensator output
j	- imaginary unit
$\Im$	- indicates imaginary part of the complex number
z	- discrete domain operator
σ	- total leakage factor
γ_m	- angle of the actual rotor displacement
θ_e	- angle of the stator flux
θ_{e0}	- compensated angle of the stator flux
$\theta_{e(mach)}$	- angle of the stator flux generated in the motor (simulation case)
θ_x, θ_y	- angle of back EMF, before and after HPF, respectively
τ	- integral time constant of PI regulator
ζ	- damping ratio
ω_e	- synchronous angular speed
ω_r	- rotor angular speed
ω_r^{el}	- electrical angular rotor speed
ω_{sl}	- slip angular speed
ω_{slk}	- breakdown slip angular speed

ω_{slN}	- nominal slip angular speed
ω_c	- cut-off frequency (rad/s)
$\widehat{x}$	- magnitude of the variable
$\overline{x}$	- vector representation of the variable
x^s	- variable represented in stationary reference frame
x^e	- variable represented in synchronously rotating reference frame
x_d, x_q	- real and imaginary components of the variable, respectively
$x_{i_{sd}}$	- variable of the d-current control loop
x_ψ	- variable of the flux control loop
$x_{i_{sq}}$	- variable of the q-current control loop
x_ω	- variable of the speed control loop
x_{off}	- offset value of the measured variable
x^*	- estimation of the variable
x_{conj}	- conjugated complex number
$x_{(ref)}$	- reference value of the variable
$x_{(err)}$	- error of the variable
$x_{(meas)}$	- measurement of the variable

Abbreviations

AC	-	Alternating Current
AAIA	-	Accurate Adaptive Integration Algorithm
CSI	-	Current Source Inverter
DC	-	Direct Current
DSP	-	Digital Signal Processor (Processing)
DTC	-	Direct Torque Control
EMF	-	Electromotive Force
FOC	-	Field Oriented Control
HPF	-	High-Pass Filter
IM	-	Induction Motor (Machine)
LPF	-	Low-Pass Filter
MFOC	-	Magnetising Field Oriented Control
PCB	-	Printed Circuit Board
PMSM	-	Permanent Magnet Synchronous Motor (Machine)
PWM	-	Pulse-Width Modulation
RFOC	-	Rotor Field Oriented Control
RTI	-	Real Time Implementation
SFOC	-	Stator Field Oriented Control
SVM	-	Space Vector Modulation
VSC	-	Voltage Source Converter
VSI	-	Voltage Source Inverter

1

Introduction

First chapter of the report, consist of necessary information, needed in further researches and analyses. It starts with brief presentation of advantages of high speed drives, and applications in which they are used. As that drives mostly utilises two types of motors, proper comparison is made. Afterwards, methods review, concerning controlling high speed drives, is made. In order to obtain advantages of the high speed drives, it is necessary to overcome specific problems. They are presented, together with challenges. It completes the presentation of the high speed systems. Subsequently, exact scope of the project is made, together with limitation. Report structure is placed at the end of the chapter.

1.1   High speed drives applications

Recently, high frequency drives gain more interest in the industry. It is mostly dictated by several advantages offered by these types of drives. Generally, together with increased speed, rises efficiency, improving operations of the applications. Also, weight and size are reduced significantly, with keeping the same output power. Lower mass, results in lower rotor inertia, what leads to better dynamic responses. That benefits are utilised in applications like micro-turbine generators, centrifugal compressors, pumps, gas turbine drive or machine tool spindles [3]-[6], [8]. In addition, high speed drives are commonly used in applications with PCB drilling machines [1] or in wood industry [18]. Both environments require similar demands: fast working process and improved quality of the manufactured product.

In case of PCB drilling machines is present technology competition between laser shooting and mechanical drilling. With continuous increasing speed of the drillers (drilling machine accessible in the market are in range 30 000 rpm - 200 000 rpm [1]), and reducing drilling diameters it seems that mechanical solution is able to provide more accurate results. Some successful tests were done with speed up to 300 000 rpm [1].

Woodworking machinery is an area where high frequency drives are exploited widely. The main reason of their usage is lack of mechanical gear. It results in reduced frequency of maintenance, much better efficiency (less mechanical losses), and more flexible operating. The last advantage seems to be the most crucial. One drive can operate several tools, by fitting the output frequency of the inverter with required speed of the chosen tool. Moreover, during non-operation time, machine can be slow down, saving energy and reducing acoustic noise. If there is a demand for that particular tool, it can be easily accelerated to the working speed. Two types of high speed drives (one with gearbox, and second utilising frequency

converter) are compared in Fig. 1.1.
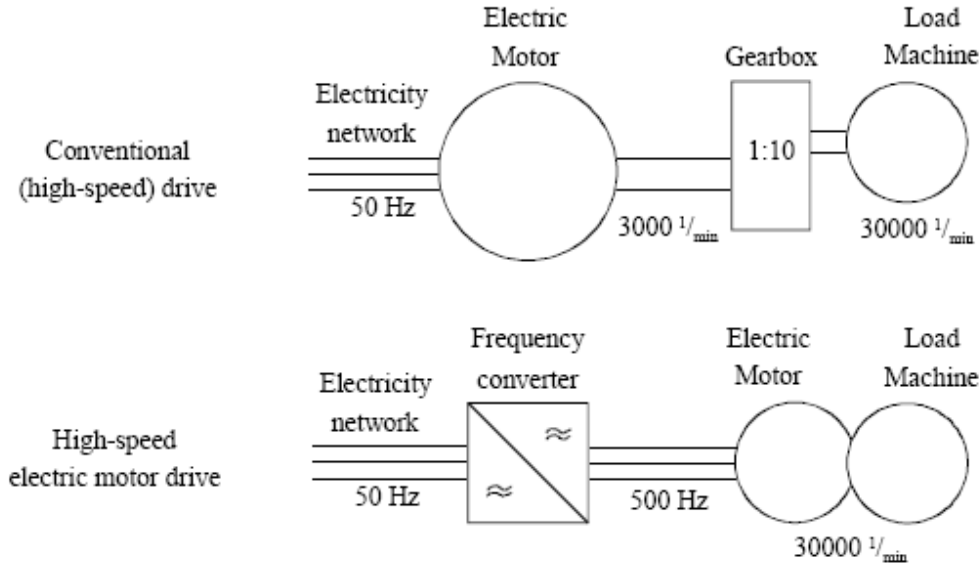
Figure 1.1: *Comparison between conventional high speed drives, consisting of a gearbox, and one using inverter. [8]*

1.2   Induction Motor vs PM Synchronous Motor

In the discussed drives, mostly two kind of motors are employed: induction machine (IM) and permanent magnet synchronous machine (PMSM). Each of them has advantages and drawbacks, which have to be taken into account. Comparison is done, basing on the discussion presented in [5].

Comparison starts from thermal and mechanical characteristics. Construction of IM is very robust, assuring operation in high temperatures. That conditions are commonly present in higher speeds, where temperature rises due to many factors (like eddy currents which are dependent on the speed). In opposite, PMSM has limited temperature range, because of sensitivity of permanent magnet materials to temperature. Their magnetic characteristics are strongly dependent on the heat. It leads to limitations in higher speed capability.

On the other hand, when electrical aspects are considered, PMSM shows better performance. Due to presence of permanent magnet materials mounted on the rotor, synchronous machine provide higher power factor, and high electrical efficiency, respectively. It effects in high power per volume ratio. In case of IM, appears relatively large rotor losses (presence of circulating current in bars). In order to limit higher harmonics in the air gap (causing additional losses), and improve cooling, air gap size is extended. As the rotor cage is magnetized from the stator side, it requires significantly big magnetizing current. Consequences of it, are large resistive losses in stator windings and low power factor.

It is also important to mention, that PMSM delivering the same amount of power as corresponding induction machine, is considerably smaller. However, there are no special

	Induction Motor	**PM Synchronous Motor**
Operation in higher temperature	possible	limited
Mechanical size	bigger	smaller
Power factor	lower	bigger
Efficiency	lower	bigger
Machine cost	comparable	
Drive cost	higher	lower

Table 1.1: *Summarized comparison between Induction Motor and Permanent Magnet Synchronous Motor used in high speed applications.*

mechanical problems with bigger rotor size of IM, as it is strong and robust.

Comparing costs of these two types of motors (producing the same amount of power), they can be roughly equal. Materials needed to construct induction machine are much cheaper. However, as it is mentioned above, to get the same output power, machine has to be bigger. It leads to bigger amount of materials. In case of PMSM, main cost is oriented around expensive permanent magnet materials. Nevertheless, final motor is smaller (less materials are needed). Thus, the rough assumption made above, can be maintained. Besides, it can be added, that due to characteristics of PMSM, it requires smaller and cheaper frequency converters (better power factor), and the cost of used energy is lower (better efficiency). Therefore, total cost of entire drive system seems to be lower for synchronous machine.

Advantages and disadvantages of both motors are collected and summarized in Tab. 1.1.

Considering all the aspects described above, it can be concluded, that induction motors can operate in bigger range of velocity offering robust characteristic, while permanent magnet synchronous machines give higher efficiency, but in limited speed area. It is clearly visible, that PMSM seems to be better solution over similar IM drive. However, speed limitation of PMSM still let IM to be considered. Therefore, eventual choice is made basing on specification of the load to be operated. For sake of that project, focus is done on the induction motor.

1.3   Control techniques

High speed drives is the field, which is still under the examination. Therefore, there is still limited existing literature covering that area. Due to that reason, references focusing on PMSM are also included in the research.

Description presented in the beginning, clearly show advantages of the high speed drives. It determines necessity of develop stable and efficient control. Most proposed algorithms base on the vector control. However, simple open-loop scalar control was also tested with satisfied results - machine was run up to 100 000 rpm [4]. It depicts, that V/f control is an attractive solution. Very simple structure and lack of mechanical sensor for rotor position measuring are the strongest points. Nevertheless, it presents also very strong dependency on machine parameters, which variations cannot be compensated (lack of signals feedback). It results in time consuming process for proper implementation and adjustment.

Control scheme, which gains more interest in low and medium speed applications is direct

torque control (DTC). It assures instantaneous control of torque and flux. However, in high speed case, it becomes very hard to realise DTC. It is caused mainly by necessity of high sampling rate, which is hard to obtain in high velocity range [6].

Drawbacks of scalar control and DTC, moves the scope on the field oriented control (FOC) solution. It is observed, that FOC strategy tested in high speed applications, found in the references, give very good results. Characterising them, it could be noted, that most utilised sensorless control, while only one uses high performance speed sensor [6]. It points out one of the problems existing in that kind of applications - proper speed/position determination (that case is more discussed in the following section). However, presented results are limited only to simulations, which cannot assure similar behaviour in the real setup. It is also visible, that usage of the FOC strategy is divided into two groups: rotor field oriented control (RFOC) [3], [4], [6], [19], and stator field oriented control (SFOC) [1], [14].

Due to better performance offered by PMSM (as it is presented previously), many authors tried to implement the control on this type of machine. Bon-Ho Bae et al in [3] proposed RFOC method to overcome challenging requirements like low stator inductance and high dc-link voltage. Tests which were done, show the comparison between drive operated with and without speed sensor. They suggested also position and speed estimator robust to the measuring noise. The only drawback was problem in low speed range, where back EMF was not big enough to run the algorithm. Machine was successfully run up to 65 000 rpm. Similar challenges, also with PMSM, were met in article written by Longya Xu and Changjiang Wang [4]. They compared vector control with scalar control, concluding better performance of the implemented RFOC. They suggested structure of self-tuning flux observer which provides good position estimation, and speed respectively to overcome resolution problems with speed sensor. They were able to operate setup to the speed of 60 000 rpm. Future research is focused on reaching velocity of 100 000 rpm and higher.

Noteworthy researches were done by Ralph M. Kennel, and documented in [1]. Special design of the entire setup let to run several different machines with speeds up to 300 000 rpm. In case of so big velocity, mechanical movement of the rotor of 1° lasts 555ns. In that very short time period, all control operations should be done. Nowadays, there is no microprocessor to fulfil that demand. Thus, proposed SFOC were hardware based. Obviously, machines were run in the encoderless way. Future works focuses on trying to operate the machine with speed of 600 000 rpm.

Another sensorless stator field oriented control was described in [14] by R. Bojoi et al. Their work concentrate on low cost applications with high torque abilities in field-weakening region. Proposed algorithm differs from standard SFOCs, offering decoupling from torque and flux commands. Also there is no need to employ feedback signal of i_{sd} current, what assure simplicity. Described strategy was tested in dSPACE environment and with fixed point DSP-based control board. Examined induction motor was accelerated successfully to 16 000 rpm.

That short presentation leads to the conclusion, that sensorless strategy should be considered in further algorithm design. However, first SFOC and RFOC have to be compared, to choose best-fitting option for sake of that project. Features and characteristics of both methods are presented basing on [15]. Comparison starts from analyzing rotor field oriented control. It assures linear relationship between control variables(i_{sd}, i_{sq}) and output value

(torque). Simple rotor voltage equations give possibility to employ current controlled PWM inverter, where algorithm can be easily implemented (no decoupling required). However, considerable complexity of stator voltage equations, caused necessity of usage decoupling network when voltage controlled PWM inverter is used. Formula for calculating flux in rotor field coordinates depends on two machine parameters (R_s and σX_s):

$$\overline{\psi}_r = \frac{X_r}{X_m} \left[\int \left(\overline{u}_s - R_s \cdot \overline{i}_s \right) dt - \sigma X_s \overline{i}_s \right] \tag{1.1}$$

where,
$\overline{\psi}_r$ is a rotor flux (in vector representation),
$\overline{u}_s$ and $\overline{i}_s$ are stator voltage and current, respectively (in vector representation),
R_s is stator resistance,
X_s, X_r, and X_m are stator, rotor and magnetizing reactances, respectively,
σ is a totali leakage factor.

In stator field oriented control case, there exists coupling between controlled variables and output, which has to be compensated. Moreover, complexity of rotor voltage equations makes implementation with current controlled inverter more difficult. On the other hand, exploitation of voltage controlled inverter is much easier (very easy decoupling). SFOC provides also very simple expression to get information about stator flux (it depends only on R_s):

$$\overline{\psi}_s = \int \left(\overline{u}_s - R_s \cdot \overline{i}_s \right) dt \tag{1.2}$$

where,
$\overline{\psi}_s$ is a stator flux (in vector representation).

Summarized, easiness in working with voltage source converters (VSC), and simple formula for flux calculation (which is crucial in vector control), are revealed to be most essential in presented project. Therefore, in further analysis direct sensorless field oriented control is chosen.

1.4   Challenges and problems

Opposite to the advantages of high speed drives applications, appear problems and challenges important to reveal. As it is already mentioned, one of the crucial aspect is to obtain reliable position (or speed) information. Normally used mechanical sensors mounted in the shaft, seem to be not trustworthy. Due to big rotational speed, they provide not reliable measuring and not sufficient accuracy of the resolution (angle information given by the Hall-effect sensors is a resolution of $\pm 30^o$)[3]. There appear also difficulty in installing and maintaining the sensors. Additionally, it limits the mechanical design and may cause problems in the aerodynamic design [3]. Alternative solution, could be usage of sensorless control. It overcomes presented difficulties. Furthermore, it significantly reduces costs of the drive [4].

Important issue is capability of fast computation control strategy, in order to obtain real time control [4]. Therefore, it is necessary to use fast digital signal processor. Sometimes, it is even impossible to employ any kind of DSP, because they may not be fast enough to fulfil calculations demands. In case of ultra high speeds, control algorithm is executed by the hardware [1].

Essential becomes choosing proper power converter. It has to be able to operate with appropriately high switching frequency, fulfilling given relationship [4]:

$$\frac{f_{pwm}}{f_{fund}} \geq 10 \tag{1.3}$$

where,
f_{pwm} is a switching frequency,
f_{fund} is a fundamental frequency.

Also, it has to be resistive to high switching frequency losses, appearing during operating high frequency drives.

Analysing existing problems, it is necessary to include non-linear effects, such dead-time or zero-current slumping effect [3]. They can deteriorate current wave, causing additional losses in the system. Because of the character of the high speed drive, there appear extra sources of the heat comparing to conventional drive supplied with $50Hz$. With increasing rotational speed, rise effects of eddy current losses and friction losses (dependant on square and cubic of the speed, respectively)[8]. Therefore, proper compensation of mentioned effects becomes crucial to reduce already high losses.

Another speed dependent value is a back electromotive force. Its rising causing reduction of the supply voltage. Maximum produced electromagnetic torque is proportional to square of that voltage. It is visible, that produced torque reduces rapidly with lowering the voltage. Thus, to get maximum torque under high speed conditions, it is relevant to use field-weakening algorithms [4], [14].

Naturally, similarly to the normal drives (supplied with $50Hz$), there exist parameters variations, due to the several phenomena, like risen temperature, skin effect or saturation. However, in case of high speed applications, that changeability is amplified. Thus, that matter should be taken into consideration in the process of tuning regulators, to have the control working properly.

There exist some additional problems like substantial stress of the stator winding insulation or bearing currents. To overcome them it is suggested to use current source inverters (CSI), instead of normally utilised VSI [2].

To summarize, besides obvious advantages, high frequency drives show several problems and challenges, which have to be overcome in order to obtain reliable operation. Therefore, in the following section, objectives of the project are formulated, and further parts of the reports present solutions to have the system running.

1.5   Objectives and limitations

In the above sections, chosen topic is introduced, together with presentation of problems to be overcome. The main objectives of the project is formulated:

Design of a vector control algorithm for induction machine drive, oriented in a stator field coordinate system, with no velocity sensors and ability to run with higher frequencies.

To fulfil that statement, whole process is divided into few subparts:

- Entire system is going to be represented by mathematical formulas. It allows to prepare a base for further analysis and algorithm design.

- Approach made to get proper parameters of the regulators used in SFOC strategy. Obviously, in real life drive system, controllers have to be tuned again, due to variations of the machine parameters (in the design process constant parameters are used). However, basis of values are determined.

- Focus made on correct flux estimations, which is crucial in field oriented control. Because of the open-loop integration used in the observer, it can lead to inappropriate magnitude and angle values, and eventually to deterioration of the entire control.

- Furthermore, proper estimation of the speed is important to fulfil demand of sensorless control. It is also connected with accuracy of flux model, which can be evaluated together with velocity estimation.

- Eventually, all the components are put together, and tested in a experimental test to check if the proposed solution is able to follow the main objective. First, with the induction machine run at grid frequency. Afterwards, high speed case is going to be emulated. It helps in verification of the theoretical model, as well.

However, scope of the work needs to be limited, due to wide range of depicted challenges:

- Motor parameters variations are not included in the analysis.

- Low speed case is not investigated in evaluation of the derived algorithm. Obtained results are only used for comparisons.

- Field weakening mode is not considered - reference stator flux is kept constant through entire speed range.

1.6   Report structure

In the section outline of the report is presented. Each chapter is introduced shortly.

2.   System Modelling - In that chapter drive system is represented by methametical formulas. Afterwards its correctness is validated with simple scalar control in MAT-LAB/Simulink environment. Afterwards, the system is used for testing the control algorithm.

3. Control Algorithm Design - This chapter consists of entire procedure used to deriving the control strategy. It is made with usage of MATLAB/SISOTool package. Proposed estimators are also included. At the end, the system is tested in simulation with field oriented control. Simulation is also done in MATLAB/Simulink. Results are commented and concluded.

4. Laboratory Implementation - Algorithm is also checked in the real system. Every tests are done in Flexible Drive System Laboratory at Aalborg University. Selected results from experiments are commented and concluded.

5. Conclusions and Future Work - In this chapter results from the entire report are summarised and compared with objectives given in section 1.5. Final conclusions are drawn, and suggestions for further work are presented.

A. Init Data - That appendix consists of every necessary parameters for running used simulations, and the test setup in the lab.

B. Simulation Models - In this appendix chosen models derived in MATLAB/Simulink are presented.

C. Hardware and Software Characteristics - Presentation of the test setup components with rated parameters are given in the appendix. Additionally, brief information about used software is put.

2

System Modelling

In order to create desired algorithm, it is necessary to represent mathematically system to be controlled. Therefore, in the following chapter mathematical model of the drive is presented. First, necessary assumptions are pointed, then formulas describing the system are expressed. Finally it is built and tested with simple V/f control to validate its correctness.

2.1   Asynchronous motor model

For sake of the project, it is decided to employ simple and idealised model of the squirrel cage induction motor. Therefore, it is necessary to present some assumptions to be made [17]:

- machine is considered as a three-phase symmetrical motor;

- only fundamental frequency is taken into account, higher harmonics are neglected;

- effects like saturation, iron losses, eddy currents or temperature dependency are disregarded;

- resistances and reactances are considered constant (results from the previous point);

- three-phase winding (or bars in the cage of the rotor), are represented by coils placed in axes shifted to each other by 120°, as it can be observed on Fig. 2.1.

- due to simpler formulas, stationary reference frame is used to model the motor, while desired control algorithm derived in Chapter 3 is done in rotating reference frame (field oriented control principle).

In order to make the notation easier, three-phase scheme is replaced by the space vector (voltage, current and flux linkage). Space vector can be defined as follows [17]:

$$\overline{k} \stackrel{def}{=} \frac{2}{3} \left[\overline{1} k_A(t) + \overline{a} k_B(t) + \overline{a}^2 k_C(t) \right] \tag{2.1}$$

where,

$$\overline{a} = e^{j2\pi/3} = -\frac{1}{2} + j\frac{\sqrt{3}}{2}; \qquad \overline{a}^2 = e^{j4\pi/3} = -\frac{1}{2} - j\frac{\sqrt{3}}{2} \tag{2.2}$$
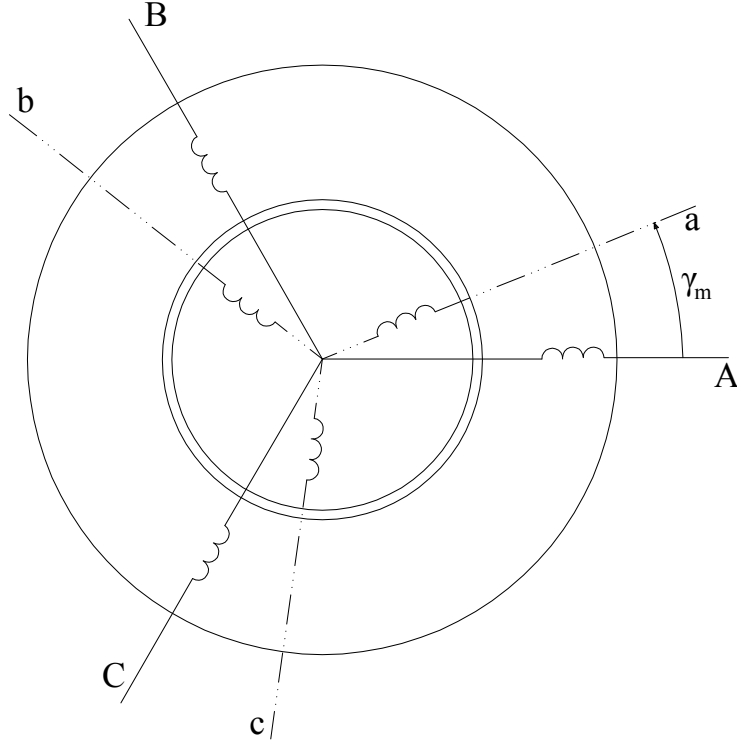
Figure 2.1: *Schematic representation of the three-phase induction motor, by placing single coils on axes shifted by angle of* 120°. *Coils represent stator windings (indicated by uppercase letters - A, B, C) and rotor bars (lowercase letters - a, b, c). Additionally, displacement of the rotor position is marked* (γ_m) *[17].*

and,

$$k_A(t) + k_B(t) + k_C(t) = 0 \tag{2.3}$$

$k_A(t), k_B(t), k_C(t)$ are the arbitrary phase quantities in the natural coordinates (A, B, C).

However, that representation has a strong disadvantage, which is dependence of magnetizing inductance (reactance) to the angle γ_m [17], depicted in Fig. 2.1. In other words, it shows variations with the actual rotor position. Therefore, to overcome that drawback, it is recommended to transform vector equations to the common rotating reference frame. In order to do this, it is decided to employ Clarke transformation, which describes the system in stationary reference frame. The idea of it is presented in Fig. 2.2

Expression for Clarke transformation can be formulated [17]:

$$\begin{bmatrix} k_d^s \\ k_q^s \end{bmatrix} = \frac{2}{3} \begin{bmatrix} 1 & -\frac{1}{2} & -\frac{1}{2} \\ 0 & \frac{\sqrt{3}}{2} & -\frac{\sqrt{3}}{2} \end{bmatrix} \begin{bmatrix} k_A \\ k_B \\ k_C \end{bmatrix} \tag{2.4}$$

where,
k_d^s, k_q^s are real and imaginary components of arbitrary chosen quantity, represented previously
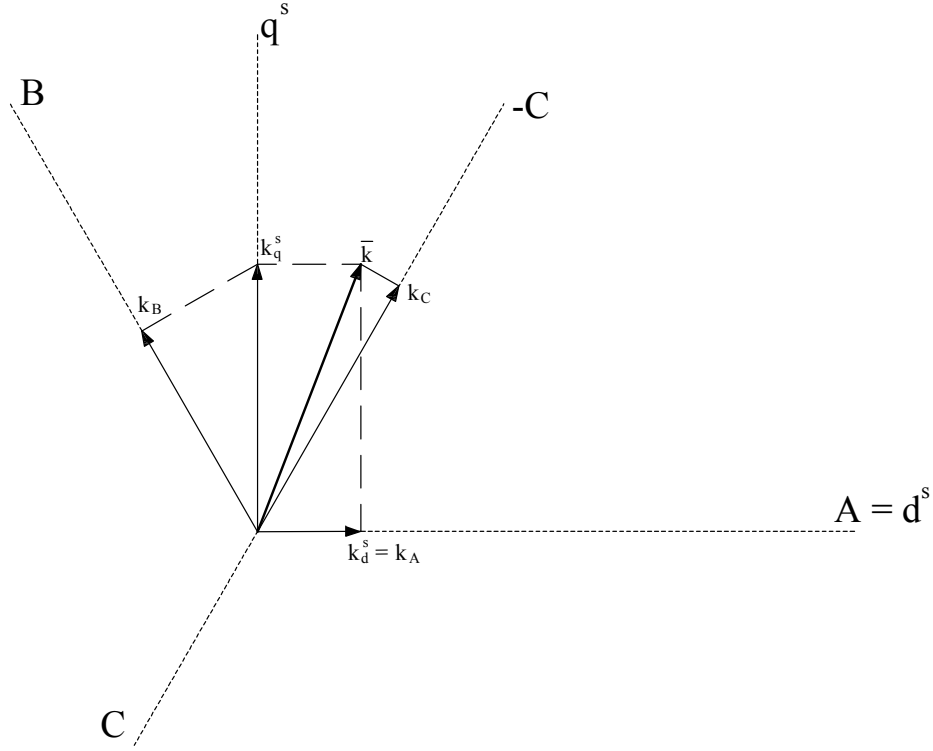
Figure 2.2: *Graphical explanation of the Clarke transformation, transforming values from three-phase natural coordinate system to two-axes stationary reference frame.*

in the natural coordinate system, given in stationary reference frame (denoted by superscript 's').

Now, it is possible to determine voltage and flux equations in the new stationary system:

$$u_{sd}^s = R_s i_{sd}^s + \frac{d\psi_{sd}^s}{dt} \tag{2.5}$$

$$u_{sq}^s = R_s i_{sq}^s + \frac{d\psi_{sq}^s}{dt} \tag{2.6}$$

$$u_{rd}^s = 0 = R_r i_{rd}^s + \frac{d\psi_{rd}^s}{dt} + \omega_r \psi_{rq}^s \tag{2.7}$$

$$u_{rq}^s = 0 = R_r i_{rq}^s + \frac{d\psi_{rq}^s}{dt} - \omega_r \psi_{rd}^s \tag{2.8}$$

$$\psi_{sd}^s = L_s i_{sd}^s + L_m i_{rd}^s \tag{2.9}$$

$$\psi_{sq}^s = L_s i_{sq}^s + L_m i_{rq}^s \tag{2.10}$$

$$\psi_{rd}^s = L_r i_{rd}^s + L_m i_{sd}^s \tag{2.11}$$

$$\psi_{rq}^s = L_r i_{rq}^s + L_m i_{sq}^s \tag{2.12}$$

where,

u_{sd}^s, u_{sq}^s are the real and imaginary stator voltage components, respectively, in stationary reference frame,

u_{rd}^s, u_{rq}^s are the real and imaginary rotor voltage components, respectively, in stationary reference frame,

i_{sd}^s, i_{sq}^s are the real and imaginary stator current components, respectively, in stationary reference frame,

i_{rd}^s, i_{rq}^s are the real and imaginary rotor current components, respectively, in stationary reference frame,

ψ_{sd}^s, ψ_{sq}^s are the real and imaginary stator flux components, respectively, in stationary reference frame,

ψ_{rd}^s, ψ_{rq}^s are the real and imaginary rotor flux components, respectively, in stationary reference frame,

R_s, R_r are the stator and rotor resistances, respectively,

L_s, L_r, L_m are the stator, rotor and magnetizing inductances, respectively,

ω_r is the rotor angular speed (in electrical radians).

In order to complete the model of the motor, expression for the mechanical motion is used:

$$M_e = M_l + J\frac{d\omega_r}{dt} + B\omega_r \tag{2.13}$$

where,

M_e is the electromagnetic torque,

M_l is the load torque,

J is the inertia,

B is the friction constant.

In order to connect input electrical power (defined by the electrical quantities) with the mechanical one, electromagnetic torque can be expressed:

$$M_e = \frac{3}{2} p_p L_m (i_{sq}^s i_{rd}^s - i_{sd}^s i_{rq}^s) \tag{2.14}$$

where,

p_p is the number of pole pairs.

Having all the necessary formulas for mathematical representation of the motor, model is built in MATLAB/SIMULINK environment. Block diagram, showing the model is presented in Fig. 2.3.
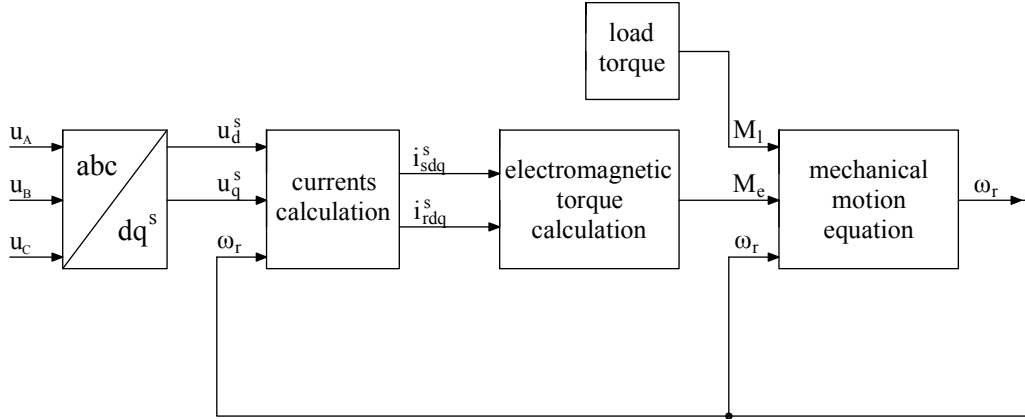
Figure 2.3: *Block diagram presenting complete squirrel cage induction motor model, defined in stationary reference frame.*

2.2 Inverter model

In order to supply the motor, inverter is used. For sake of the modelling process, its idealised model is utilised, given by the sequence of switching states. Topology of the typical three-phase inverter is shown in Fig. 2.4.
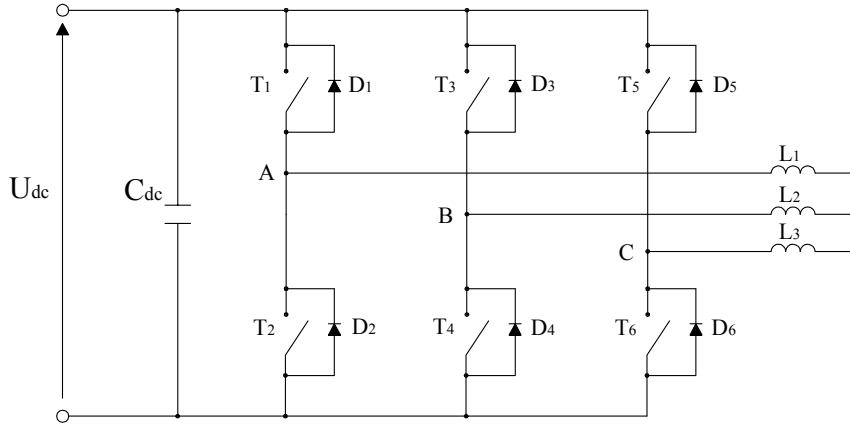
Figure 2.4: *Typical topology of the three-phase inverter.*

Load is supplied with line-to-line voltages, produced by the converter. It yields:

$$u_{AB} = u_A - u_B \tag{2.15}$$

$$u_{BC} = u_B - u_C \tag{2.16}$$

$$u_{CA} = u_C - u_A \tag{2.17}$$

where, u_A, u_B, u_C are phase voltages.

Additionally, it is assumed, that:

$$u_A + u_B + u_C = 0 \tag{2.18}$$

Combining (2.15)-(2.17) and (2.18), proper phase voltages can be formulated:

$$\begin{bmatrix} u_A \\ u_B \\ u_C \end{bmatrix} = \frac{1}{3} \begin{bmatrix} 1 & 0 & -1 \\ -1 & 1 & 0 \\ 0 & -1 & 1 \end{bmatrix} \begin{bmatrix} u_{AB} \\ u_{BC} \\ u_{CA} \end{bmatrix} \tag{2.19}$$

Switching states, mentioned in the beginning of that chapter are represented by three variables: D_A, D_B, D_C. Each of them defines state of one leg of the inverter, and it can take $'0'$ or $'1'$ ($'0'$ means that the switch is turned off, while $'1'$ it is conducting). Thus, line-to-line voltages can be linked with DC voltage supplying the converter:

$$\begin{bmatrix} u_{AB} \\ u_{BC} \\ u_{CA} \end{bmatrix} = U_{dc} \begin{bmatrix} 1 & -1 & 0 \\ 0 & 1 & -1 \\ -1 & 0 & 1 \end{bmatrix} \begin{bmatrix} D_A \\ D_B \\ D_C \end{bmatrix} \tag{2.20}$$

Minus in (2.20) determines direction of the current flow (turning on lower or upper switch, in other words). Inserting (2.20) into (2.19), relationship between switching states, and phase voltages feeding the motor is obtained:

$$\begin{bmatrix} u_A \\ u_B \\ u_C \end{bmatrix} = \frac{U_{dc}}{3} \begin{bmatrix} 2 & -1 & -1 \\ -1 & 2 & -1 \\ -1 & -1 & 2 \end{bmatrix} \begin{bmatrix} D_A \\ D_B \\ D_C \end{bmatrix} \tag{2.21}$$

Modelled electrical drive is controlled with space vector modulation (SVM) strategy [16]. The results of simulations are shown in the following section.

2.3 Drive model validation

In order to verify correctness of the modelled system, it is decided to run it using simple V/f algorithm. For sake of the simplicity, carrier-based modulation is omitted, generated duty cycles are directly supplied to the converter. Tests are done for $f_{fund} = 50Hz$ (nominal frequency of the motor under examination). Necessary parameters for running the simulation are listed in Appendix A

In the following graphs, results from tests are shown. First, velocity response is presented (Fig. 2.5). It can noticed that, in the beginning machine rotates with the synchronous speed, what indicates no-load conditions. Immediately after the load torque is applied to the shaft, actual rotor velocity is reduced to $n_r = 1431rpm$.

In the next graph, phase voltages fed to the motor, are depicted (Fig. 2.6). Magnitude of the signals is spotted: $\widehat{u} = 311.1V$. That information allows to compare with rated voltage given by the manufacturer ($u_N = 220V$). Below, RMS value is calculated (that expression
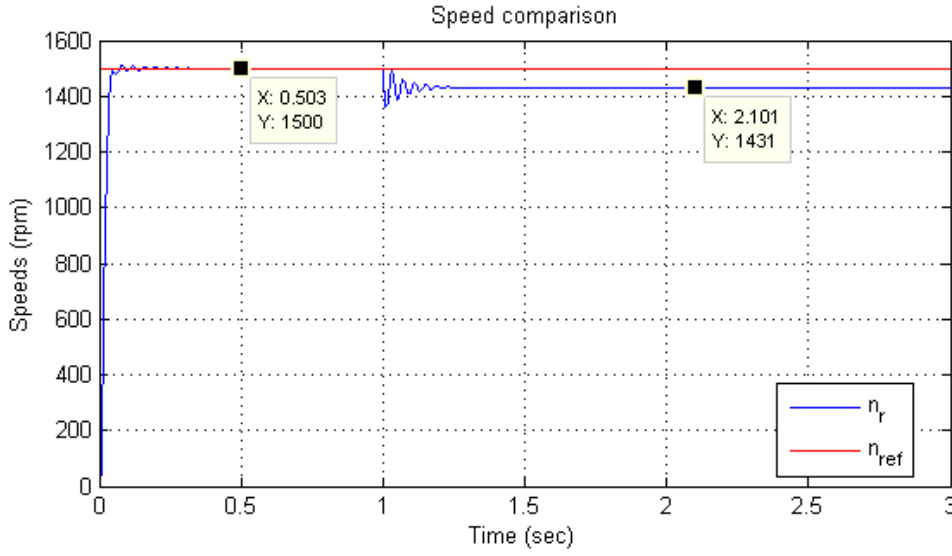
Figure 2.5: *Speed response of the system. Until $T_{sim} = 1s$ drive is run without load, just after, nominal torque is applied.*

for RMS computation is valid, as it is assumed, that motor is supplied with ideal, sinusoidal voltage):

$$u_{RMS} = \frac{\widehat{u}}{\sqrt{2}} = 219.98V \approx u_N = 220V \tag{2.22}$$

The error introduced in (2.22) is negligibly small. Additionally, in Fig. 2.6 zoom on the scope is made in order to expose sinusoidal character of the supplied voltages. It shows, that modulation technique, together with the simple inverter representation, work as expected.
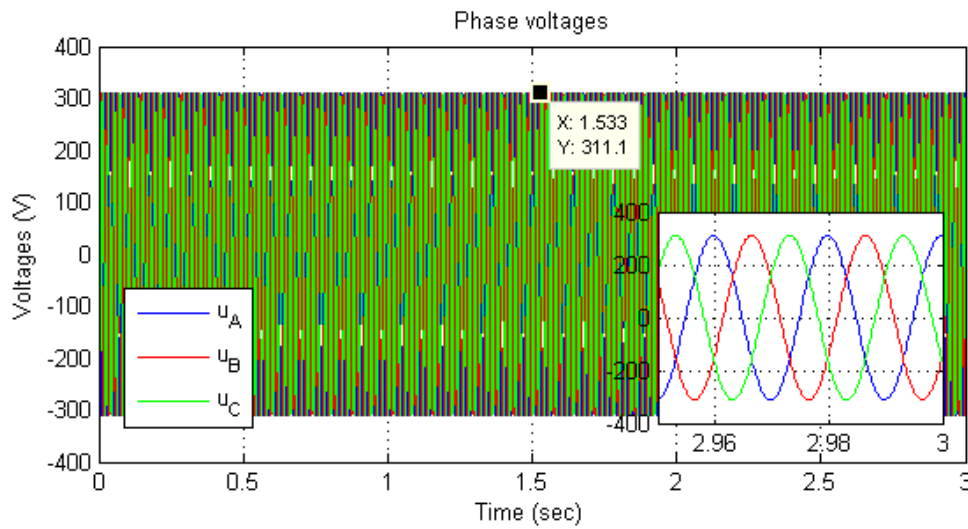
Figure 2.6: *Overall presentation of the phase voltages waves. Magnitude is marked: $\widehat{u} = 311.1V$. Additionally, waves are zoomed in particular portion of time - shape of the signals is exposed.*

Eventually, current waves are depicted in Fig. 2.7. Obtained results easily show, that current waves can be divided into three periods:

- $T_{simI} \approx 0..0.05sec$ - high current presence (demand for producing electromagnetic torque to overcome the rotor inertia);

- $T_{simII} \approx 0.05..1sec$ - stabilisation at $\widehat{i} = 4.063A$ (sufficient current to spin the motor with its inertia - no-load conditions);

- $T_{simIII} \approx 1..3sec$ - stabilisation at $\widehat{i} = 6.944A$ (necessary current to operate the machine with applied torque).

Analysis of the correctness of given results is similar to the analysis of voltages - obtained RMS value is compared with rated one ($i_N = 5.0A$):

$$i_{RMS} = \frac{\widehat{i}}{\sqrt{2}} = 4.91V \approx i_N = 5.0A \tag{2.23}$$

It is easy to note that error introduced in current measurements is higher than one obtained from voltage comparison. The reason of that situation is assumption made in the beginning, about neglecting iron losses. As that energy consumption is not taken into account, it is requested lower current for the same torque level. Therefore, obtained current is a bit lower than expected one.
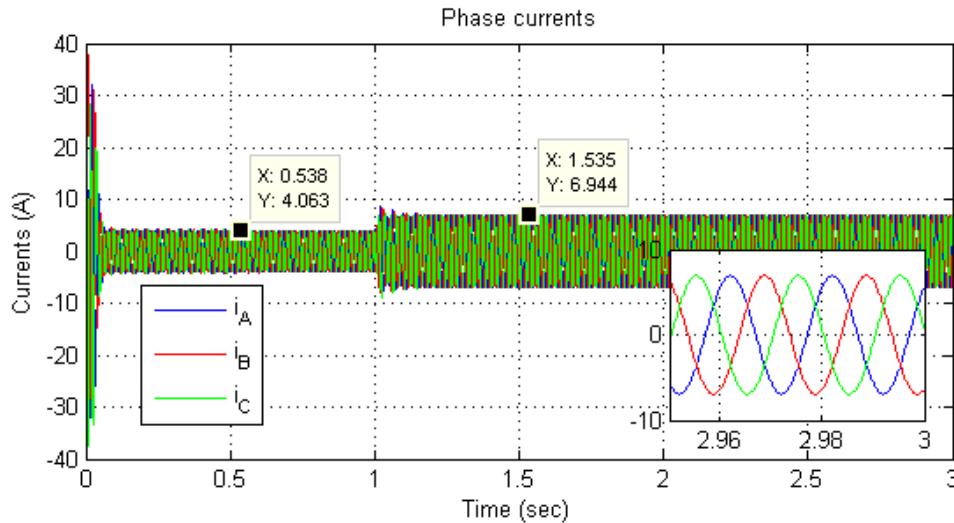
Figure 2.7: *Overall presentation of the phase current waves. There are noticeable difference between two spotted values. First is related to magnitude of current under no-load conditions ($\widehat{i} = 4.063A$), while the second one after applying rated torque ($\widehat{i} = 6.944A$). When the machine is started, high current presence is visible. Additionally, waves are zoomed in particular portion of time - shape of the signals is exposed.*

2.4   Summary

In that chapter, two main parts of the application (motor and inverter) are analysed and represented by mathematical formulas. They are going to be utilised later in testing exact algorithm. Therefore, first it is necessary to validate, if the system is defined correctly. That is done with running the drive with simple scalar control. It is decided to run the inverter with space vector modulation. Results obtained from the tests, confirm sufficient accuracy of modelled parts. Hence, desired control strategy can be examined.

3

Control Algorithm Design

In the following chapter design process of the chosen strategy is described. It starts from short presentation of principles of field oriented control. Later on focus is made on deeper analysis of direct stator field oriented control. Afterwards, exact design procedure begins. Additionally, to fulfil the sensorless demand concluded in Chapter 1, flux observer and speed estimator are introduced. Chapter ends with simulation results, verified using the developed system presented in Chapter 2.

3.1 Field oriented control principles

The idea hidden behind using field oriented control, is to obtain the ease of controlling the machine, like in case of DC motors. Torque produced by the direct current machine, is regulated by varying the armature current, while excitation current is set to be constant, giving constant flux. To emulate that behaviour in AC machine, it is necessary to employ mathematical representation of the motor. Similarly to model presented in Chapter 2, instead of stationary reference frame, it is possible to utilise rotating coordinate system. Obviously, it can rotate with an arbitrary speed, but for sake of FOC, it is chosen the synchronous speed. However, it is not enough - it has to be oriented with one of the spinning flux space vectors. Because the flux space vector rotates with the synchronous speed, therefore speed for mentioned reference frame is selected to be synchronous, as well. Hence, there are three types of FOCs: stator field oriented control (SFOC), rotor field oriented control (RFOC) and magnetising field oriented control (MFOC). Name of the strategy easily shows, which space vector is chosen to oriented.

Orientation enables to decouple currents into two components: flux component (aligned with d-axis, the same as the reference space vector), and torque component (aligned with q-axis). That components are commanded by reference torque and flux, respectively. Reference torque can be determined by feedback of the actual rotational speed of the motor - through PI regulator. By keeping reference flux at the constant, at nominal value, formula of produced torque is reduced (which is going to be presented in subsequent section), which results in a proportional relationship to the reference q-axis current. It clearly depicts similarity to controlling the DC motor.

3.2 Principle of stator field oriented control

As it is mentioned previously, to obtain the advantages from any field oriented control, it is necessary to decouple stator currents (represented by the space vector, rotating in the complex plain) into flux and torque components. In case of stator field oriented control, it is done in synchronously rotating reference frame, aligned with the space vector of the stator flux. Therefore, precise knowledge about its actual position, and magnitude, becomes crucial. As the stator flux cannot be measured, it has to be estimated based on mathematical formulas describing the machine. However, the very simple expression, which is presented in section 1.3 - (1.2), suffers from dc-offset and drift, which causes difficulties in realising it in the real setup. Thus, it is necessary to employ the observer, to overcome that drawbacks and obtain reliable information about the flux. Deeper analysis of the problems and proposed solutions are described further in the chapter (section 3.4). Now, it is assumed that position and magnitude are perfectly known, hence SFOC can be implemented. Representation of discussed current space vector in chosen reference frame, is shown in Fig. 3.1.
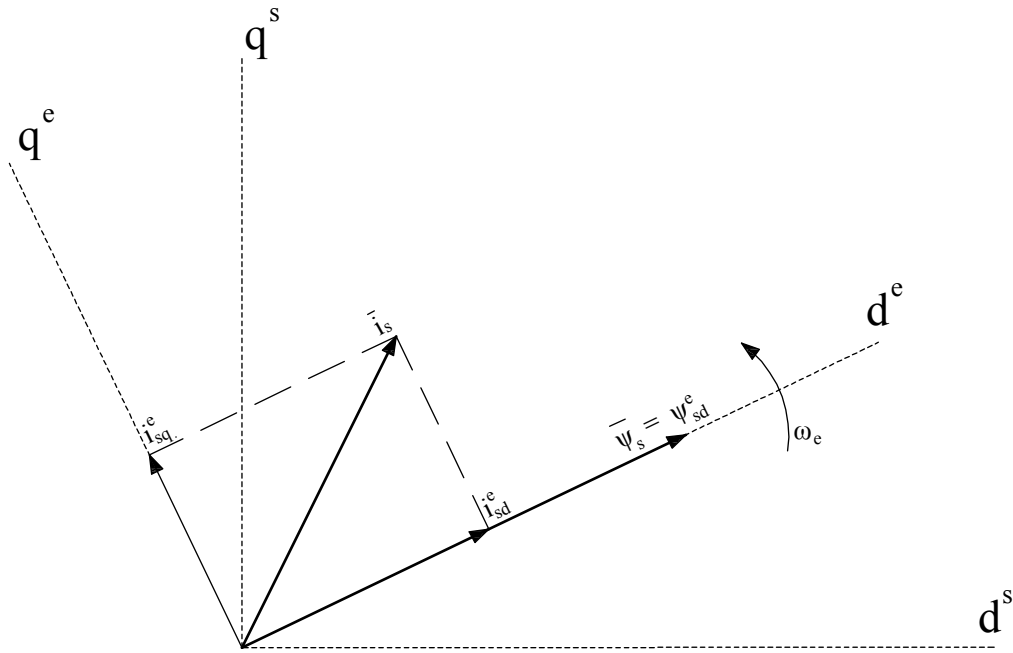
Figure 3.1: *Representation of current space vector in synchronously rotating reference frame, with d-axis alignment with stator flux space vector. Stator flux space vector contains only real component.*

Formulas used to build induction motor model, represented in complex form, are as following:

$$\overline{u}_s = R_s \overline{i}_s + \frac{d\overline{\psi}_s}{dt} + j\omega_e \overline{\psi}_s \tag{3.1}$$

$$0 = R_r \overline{i}_r + \frac{d\overline{\psi}_r}{dt} + j(\omega_e - \omega_r)\overline{\psi}_r \tag{3.2}$$

$$\overline{\psi}_s = L_s \overline{i}_s + L_m \overline{i}_r \tag{3.3}$$

$$\overline{\psi}_r = L_r \overline{i}_r + L_m \overline{i}_s \tag{3.4}$$

Besides ability to utilise field oriented control, orientation rotating reference frame with the chosen flux space vector, reduces significantly complexity of the expressions. It is due to the elimination of imaginary component of the flux, $\psi_{sq}^e = 0$, consequently $\overline{\psi}_s^e = \psi_{sd}^e + j\psi_{sq}^e = \psi_{sd}^e$ (as it can be observed in Fig. 3.1). Hence, motor equations, given in stator flux synchronous frame, are:

$$u_{sd}^e = R_s i_{sd}^e + \frac{d\psi_{sd}^e}{dt} \tag{3.5}$$

$$u_{sq}^e = R_s i_{sq}^e + \omega_e \psi_{sd}^e \tag{3.6}$$

$$u_{rd}^e = 0 = R_r i_{rd}^e + \frac{d\psi_{rd}^e}{dt} - (\omega_e - \omega_r)\psi_{rq}^e \tag{3.7}$$

$$u_{rq}^e = 0 = R_r i_{rq}^e + \frac{d\psi_{rq}^e}{dt} + (\omega_e - \omega_r)\psi_{rd}^e \tag{3.8}$$

$$\psi_{sd}^e = L_s i_{sd}^e + L_m i_{rd}^e \tag{3.9}$$

$$\psi_{sq}^e = 0 = L_s i_{sq}^e + L_m i_{rq}^e \tag{3.10}$$

$$\psi_{rd}^e = L_r i_{rd}^e + L_m i_{sd}^e \tag{3.11}$$

$$\psi_{rq}^e = L_r i_{rq}^e + L_m i_{sq}^e \tag{3.12}$$

where,
ω_e is the angular synchronous speed.

'e' superscript denotes synchronously rotating reference frame.

Calculation of the produced torque is also reduced, as it is shown below:

$$M_e = \frac{3}{2} p_p i_{sq}^e \psi_{sd}^e \tag{3.13}$$

Characteristic of the discussed drive causes consideration of running the motor sensorless. The reasons of this are presented in section 1.4. Therefore algorithm structure is supplemented with estimation of the rotational speed (section 3.5). Finally, algorithm can be constructed. Its overall structure is represented in Fig. 3.2.
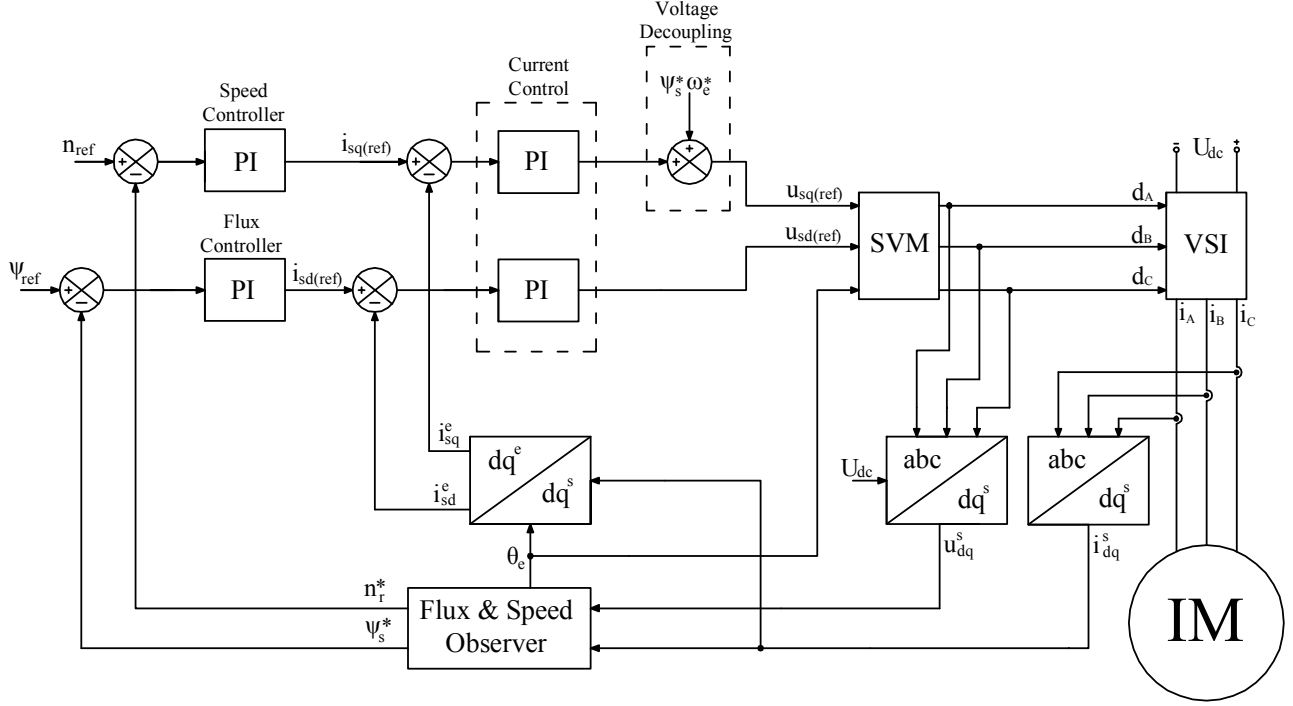
Figure 3.2: *Block diagram presenting stator field oriented control, run sensorless. The only measurements are phase currents. Voltages required for flux and speed estimations, are calculated with U_{dc} and duty cycles feedbacks. Feedback of the stator flux and rotational speed is obtained with respective estimators - placed together in one block 'Flux & Speed Observer'. [15]*

System shown in Fig. 3.2 consists of four PI controllers: two for speed and flux regulation, and two for dq^e currents regulation. Feedback signals for speed and flux regulators come from respective estimators (placed together in one block 'Flux & Speed Observer'). Inputs to the observers are voltages and currents represented in stationary reference frame. Current signals come from sensors mounted on wires supplying the machine. Voltage signals are estimated with usign dc-link voltage and duty cycles fed to the converter. Additionally, flux observer provides the information about actual position of the stator flux, utilised to transform the currents from stationary to rotating reference frame. Transformed signals are used as feedbacks for current regulators. Current controllers generate reference voltages, and together with stator flux angle estimation, they are used for space vector modulation technique. Additionally, coupling component existing in q-axis voltage (3.6), is added to the control structure.

Principle in implementation of field oriented control is representation stator current space vector in a rotating reference frame. It is realised with stator flux position information, provided by the flux observer (Fig. 3.2). Transformation is done with utilisation of Park transformation [17]:

$$
\begin{bmatrix} i_{sd}^e \\ i_{sq}^e \end{bmatrix} = \begin{bmatrix} cos\theta_e & sin\theta_e \\ -sin\theta_e & cos\theta_e \end{bmatrix} \begin{bmatrix} i_{sd}^s \\ i_{sd}^s \end{bmatrix}
\tag{3.14}
$$

where,
i_{sd}^e, i_{sq}^e, are the real and imaginary components of the stator current space vector, respectively, represented in synchronously rotating reference frame,
θ_e, is the stator flux angle (determining its actual position in the plain).

The idea of the Park transformation is presented in Fig. 3.3.
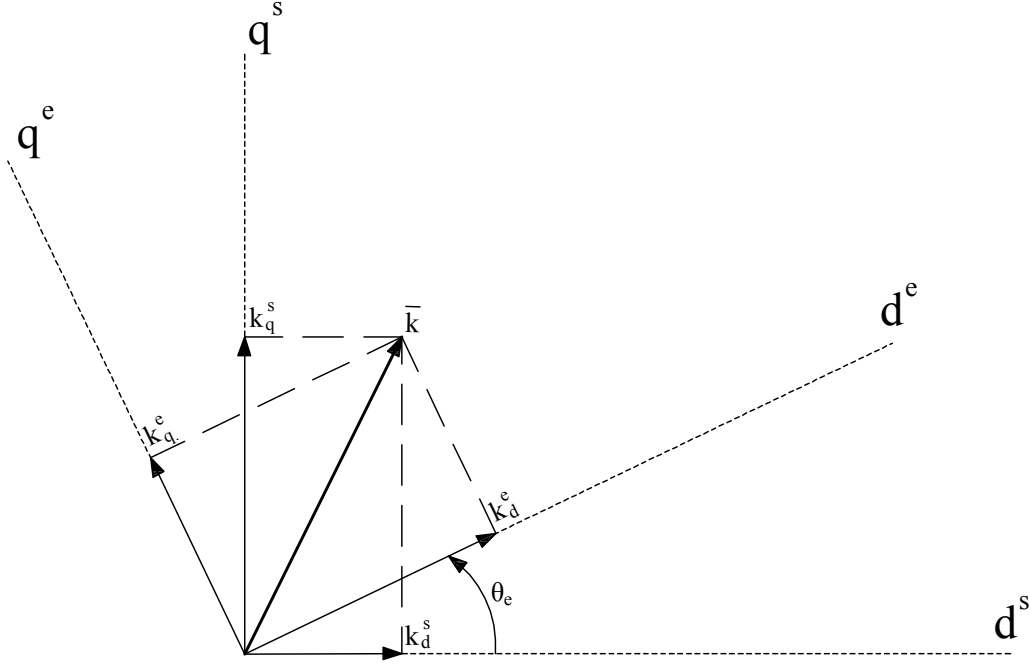
Figure 3.3: *Graphical realisation of the Park transformation. $\overline{k}$ denotes arbitrary chosen space vector. dq^s and dq^e are stationary and rotating reference frames, respectively. θ_e determines actual placement of dq^e.*

3.3 PI controllers

Control diagram presented in Fig. 3.2 contains four PI controllers: two for speed and flux regulation, and two for dq^e currents regulation. Their general aim is to provide proper and stable operations of the drive. In order to obtain that, their parameters have to be selected appropriately to controlled drive system. Also, they have to fulfil particular requirements:

- inner (current) regulators: overshoot no more than 4% ($M_p < 4\%$).

- outer regulators: slower than current controllers - it is demanded to maintain the stability of the system.

Transformation to synchronous orientation assures that converted currents become as dc components in steady state. It leads to achieving zero error of the fundamental component. [7], [9]. Therefore, current regulators are defined in the synchronous reference frame.

The ordinary PI regulator is expressed by the following formula:

$$PI(p) = K_p + \frac{K_i}{p} = K_p \frac{1 + \tau p}{\tau p} \tag{3.15}$$

where,
K_p, K_i are proportional and integral gains, respectively,
τ is the integral time constant,
p is the Laplace operator.

Entire tuning process is divided into four parts:

- d-axis current loop

- d-axis flux loop

- q-axis current loop

- q-axis speed loop

Regulators are adjusted with usage of MATLAB/SISOTOOL package. After the tuning process, antiwindup solution is presented to overcome nonlinearity effects in the control system (reason of their presence is also explained).

3.3.1 d-axis current loop

Before the exact tuning procedure can start, it is necessary to determine the object to be controlled by the regulator (it is named 'plant'). In case of controlling i_{sd}^e, (3.5) is chosen, together with (3.9):

$$u_{sd}^e = R_s i_{sd}^e + \frac{d}{dt} \left(L_s i_{sd}^e + L_m i_{rd}^e \right) \tag{3.16}$$

From (3.11), one can obtain:

$$i_{rd}^e = \frac{\psi_{rd}^e - L_m i_{sd}^e}{L_r} \tag{3.17}$$

After placing it into (3.16), and utilising few mathematical manipulation, the result is:

$$u_{sd}^e = i_{sd}^e \left(R_s + pL_s' \right) + p \frac{L_m}{L_r} \psi_{rd}^e \tag{3.18}$$

where,
$L_s' = L_s - (L_m^2/L_r)$ is the transient inductance,
p is the Laplace operator, replacing d/dt.

Component: $p \frac{L_m}{L_r} \psi_{rd}^e$ in (3.18) is considered as a disturbance, and is neglected in further analysis. Nevertheless, its presence in the real system is not avoidable, unless it is compensated. Thus, the behaviour of the regulator defined on the basis of the simplified transfer

function, is verified during tests of entire control algorithm. Eventually transfer function of the plant can be formulated:

$$G_{i_{sd}(plant)}(p) = \frac{i_{sd}^e}{u_{sd}^e} = \frac{1}{R_s + pL_s'} = \frac{1}{R_s\,(pT_s' + 1)} \tag{3.19}$$

where,
$T_s' = L_s'/R_s$

In order to represent better the real system, certain delays are introduced [10], [11], with respective times:

- **control algorithm** - delay corresponding to time needed for necessary calculations (time constant: T_s);

- **zero-order-hold (ZOH)** - delay given by holding element keeping the same value during sample period (time constant: $0.5T_s$);

- **inverter** - delay emulating presence of the inverter driven by pulse-width modulation (time constant: $0.5T_{pwm}$);

- **sensor** - delay introduced by the current sensor, which samples and holds read value (time constant: $0.5T_s$).

where,
$T_s = 1/f_s$, $T_{pwm} = 1/f_{pwm}$, and f_s, f_{pwm}, are sampling and switching frequencies, respectively (they are chosen to be equal to $5kHz$.).

Existing delays (called 'transportation lags', as well) cause, that no change occurs in the plant until corresponding time delays elapse. In time domain, arbitrary delay can be defined, as [27]:

$$y(t) = x(t - T_d) \tag{3.20}$$

where,
$x(t)$ is the input of the transportation lag,
$y(t)$ is the output of the transportation lag,
T_d is the time delay of the transportation lag.

Its transfer function is then:

$$G_{lag}(p) = \frac{Y(p)}{X(p)} = \frac{X(p)e^{-T_d p}}{X(p)} = e^{-T_d p} \tag{3.21}$$

In order to proceed the transportation lag in the analysis, instead of exponential form, it is preferable to have it defined with a rational function. It is possible to achieve, employing (p_{pol}, q_{pol}) *Padé approximant* [11], where (p_{pol}, q_{pol}) are degrees of numerator and denominator polynomials, respectively. The idea is to define exponential and rational functions by the *McLauren series*, and after that find the coefficients of the numerator and denominator of the rational function. The higher order of polynomials of the rational function, the better

precision of the approximant. However, in case of small delays introduced previously, it is acceptable to use (0,1) Padé approximant, which yields [11]:

$$e^{-T_d p} \cong \frac{1}{1 + T_d p} \tag{3.22}$$

Block diagram of the current close-loop, with regulator, presented delays and the plant to be controlled, is shown in Fig. 3.4.
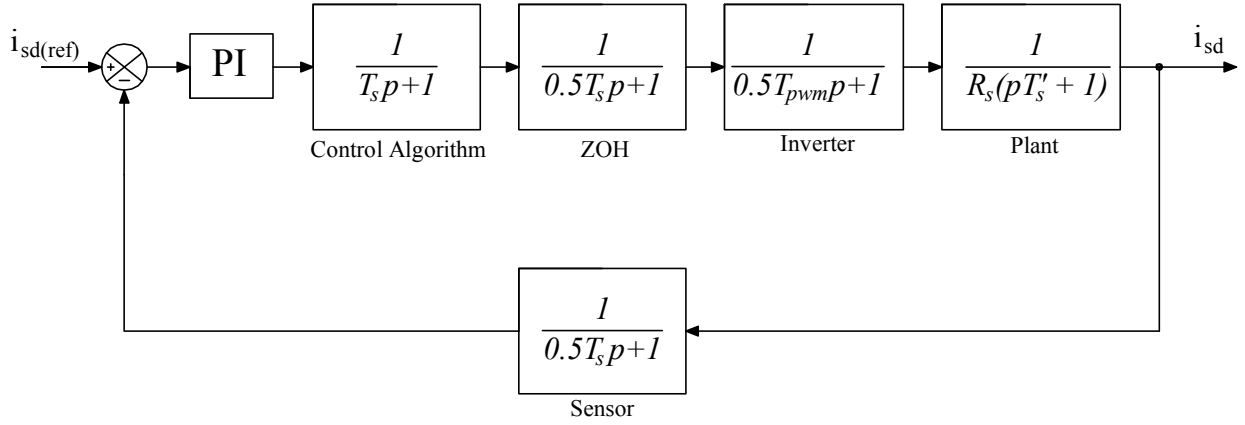
Figure 3.4: *Block diagram of the i_{sd} current close-loop with regulator to be tuned.*

As the sensed current signal is sampled, it is necessary to prevent it from possible aliasing. Usually, it is done with analog anti-alias prefilter put between sensor and A/D converter [11]. However, as the current algorithm is designed for conventional motor (with nominal stator frequency $f_{stN} = 50Hz$), and sampling frequency is chosen to be $f_s = 5kHz$, *sampling theorem of Nyquist and Shannon* is satisfied. The theorem states, that sampled signal is reconstructed appropriately, if it does not contain frequency components higher than half sample rate. Therefore, mentioned prefilter might be avoided.

To simplify further analysis, it is desired to have unity feedback, thus, diagram in Fig. 3.4 can be reformulated, as it is depicted in Fig. 3.5.
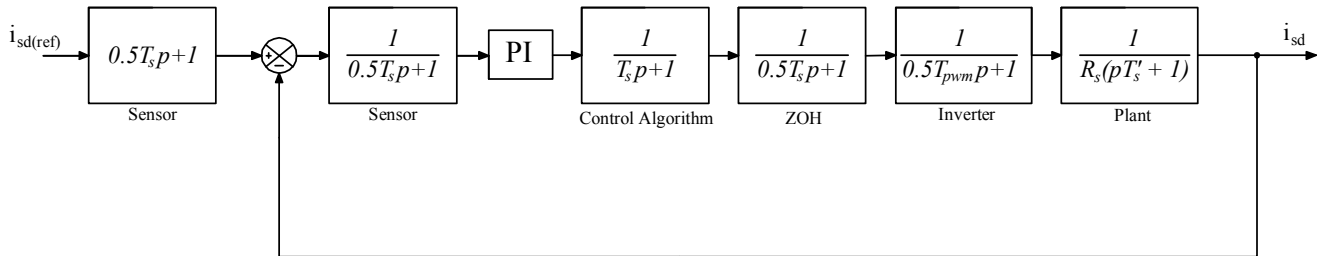
Figure 3.5: *Block diagram of the i_{sd} current close-loop with regulator to be tuned. Unity feedback is obtained.*

On the basis of Fig. 3.5, open-loop transfer function of the system can be expressed:

$$G_{i_{sd}(ol)}(p) = K_{pi_{sd}} \frac{1 + p\tau_{i_{sd}}}{p\tau_{i_{sd}}} \frac{1}{0.5T_s p + 1} \frac{1}{T_s p + 1} \frac{1}{0.5T_s p + 1} \frac{1}{0.5T_{pwm} p + 1} \frac{1}{R_s (pT_s' + 1)} \quad (3.23)$$

Now, coefficients of the PI regulator can be determined. First zero of the controller is chosen to neutralize the effect of the smallest pole, to improve dynamic of the controlled system. Smallest pole is related to the plant, so:

$$\tau_{i_{sd}} = T_s' \quad (3.24)$$

Afterwards, proportional gain is found on the basis of *magnitude optimum criterion*, where the damping ratio is set $\zeta = \frac{\sqrt{2}}{2} = 0.707$ [13]. Finally, parameters are tuned to the following values:

$$K_{pi_{sd}} = 20.1264, \quad K_{ii_{sd}} = 3530.9, \quad \tau_{i_{sd}} = 0.0057 \quad (3.25)$$

The response of the d-current control system (considered with the designed controller) to the step command is investigated. The result is shown in Fig. 3.6.
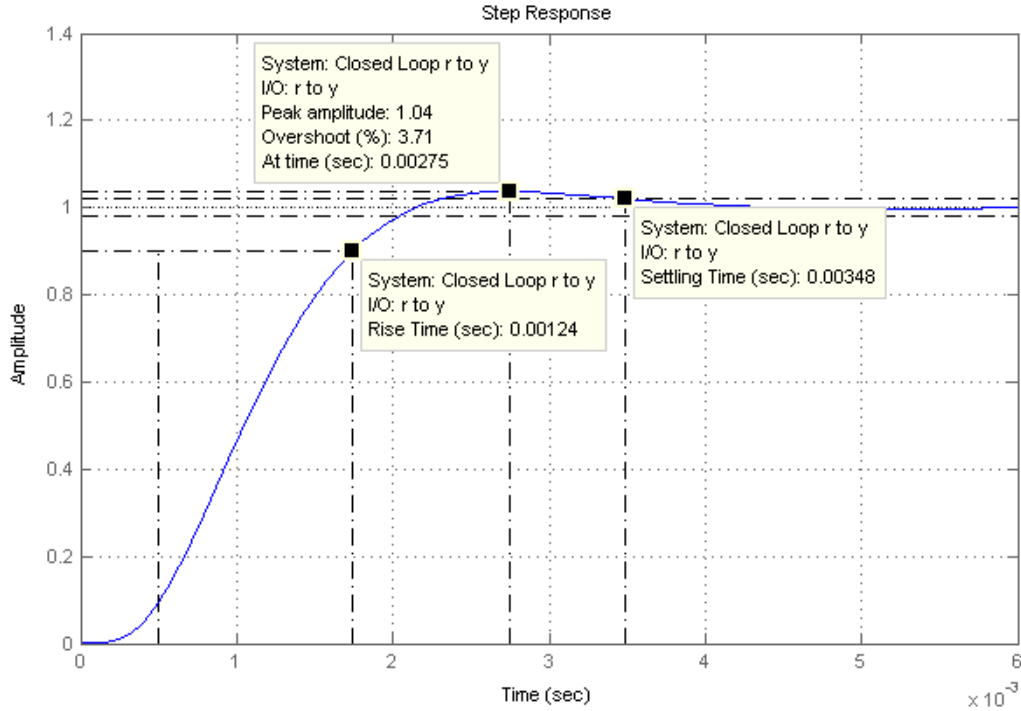
Figure 3.6: *Step response of the system with designed $PI_{i_{sd}}$ controller. Typical characteristics are marked: rising time $(t_{r(10\%-90\%)}) = 1.24ms$, settling time $(t_{s(2\%)}) = 3.48ms$ and the maximum overshoot $(M_p) = 3.71\%$. Value '1' on the 'Amplitude' axis denotes arbitrary chosen d-current reference, applied to the control system.*

Obtained controller leads to the following properties of the system:

$$t_{r(10\%-90\%)} = 1.24ms, \quad t_{s(2\%)} = 3.48ms, \quad M_p = 3.71\% \tag{3.26}$$

where,
$t_{r(10\%-90\%)}$ is a rising time,
$t_{s(2\%)}$ is a settling time,
M_p is a maximum overshoot.

Step response of the system (Fig. 3.6) shows that regulator acts stable. Additionally, zero-pole map of the close-loop system, with added regulator, is plotted in Fig. 3.7. It proves stability, as well, since every poles and zero are placed on the left half of the complex plain.
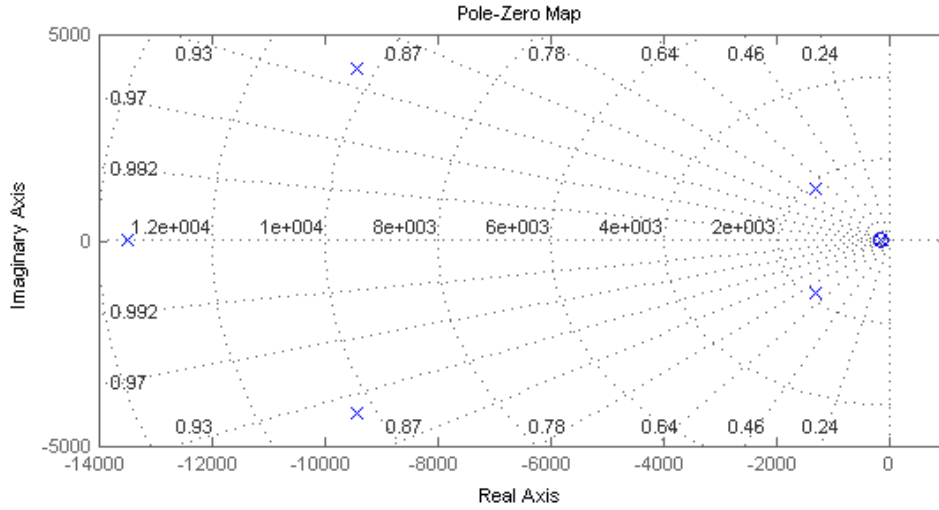
Figure 3.7: *Pole-zero map of the d-current close-loop, including designed regulator. Result indicates stability of the system - all zeros and poles are placed on the left half of the complex plain. Zeros are determined by circles, while poles by crosses.*

The condition for current controllers, stated in the beginning of the section, is fulfilled.

3.3.2 d-axis flux loop

Regulator used to keep the stator flux at the desired level is tuned by following the similar procedure utilised previously. Therefore, first it is necessary to evaluate transfer function of the plant to be controlled. The evaluation starts from placing (3.11) and (3.12) into (3.7), which yields:

$$0 = R_r i^e_{rd} + p(L_r i^e_{rd} + L_m i^e_{sd}) - (\omega_e - \omega_r)(L_r i^e_{rq} + L_m i^e_{sq}) \tag{3.27}$$

Rotor current components, can be obtained with utilisation of (3.9) and (3.10). It results in:

$$0 = R_r \frac{\psi^e_{sd} - L_s i^e_{sd}}{L_m} + p\left(L_r \frac{\psi^e_{sd} - L_s i^e_{sd}}{L_m} + L_m i^e_{sd}\right) - (\omega_e - \omega_r)\left(-\frac{L_r L_s}{L_m} + L_m\right) i^e_{sq} \quad (3.28)$$

After computation process, (3.28) can be reduced:

$$i^e_{sd}(pL_\sigma + R_r L_s) = \psi^e_{sd}(R_r + pL_r) + L_\sigma s\omega_e i^e_{sq} \quad (3.29)$$

where,
$L_\sigma = L_r L_s - L_m^2$
$s\omega_e = (\omega_e - \omega_r) = \frac{(R_r L_s + pL_\sigma)i^e_{sq}}{L_r \psi^e_{sd} - L_\sigma i^e_{sd}}$

Component: $L_\sigma s\omega_e i^e_{sq}$ in (3.29) is considered as a disturbance, and is ignored in the design process. Similarly to coupling component in the plant of d-current loop control, given in (3.18), its presence in the real system is not avoidable, unless it is compensated. Thus, the behaviour of the regulator defined on the basis of the simplified transfer function, is verified during tests of entire control algorithm.

After utilisation of some mathematical manipulation, transfer function of the plant is formulated:

$$G_{\psi(plant)}(p) = \frac{\psi^e_{sd}}{i^e_{sd}} = \frac{\left(\frac{L_\sigma}{R_r L_s}p + 1\right) R_r L_s}{\left(\frac{L_r}{R_r}p + 1\right) L_r} = \frac{R_r L_s}{L_r} \frac{(T_\sigma p + 1)}{(T_r p + 1)} \quad (3.30)$$

where,
$T_\sigma = L_\sigma/(R_r L_s)$
$T_r = L_r/R_r$ is a rotor time constant.

Once, the transfer function of the plant is known, it is necessary to determine the transfer function of the inner loop. Referring to Fig. 3.5, equivalent time constant of the open-loop system can be formulated, as the sum of every small time constants [17]:

$$T^{eq}_{i_{sd}(ol)} = 0.5T_s + T_s + 0.5T_s + T_{pwm} = 0.5ms \quad (3.31)$$

According to used criterion to design the current loop, its close-loop transfer function can be expressed [13]:

$$G_{i_{sd}(cl)}(p) = \frac{1}{2\left(T^{eq}_{i_{sd}(ol)}p\right)^2 + 2T^{eq}_{i_{sd}(ol)}p + 1} \quad (3.32)$$

And the transfer function of entire i_{sd} current control loop, is given:

$$G_{i_{sd}}(p) = (0.5T_s p + 1)\frac{1}{2\left(T^{eq}_{i_{sd}(ol)}p\right)^2 + 2T^{eq}_{i_{sd}(ol)}p + 1} \quad (3.33)$$

Assuming, that:

$$(1 + 0.5T_sp)(1 - 0.5T_sp) = 1 - 0.25T_s^2p^2 \approx 1 \quad \Rightarrow \quad 0.5T_sp + 1 = \frac{1}{1 - 0.5T_sp} \quad (3.34)$$

transfer function given in (3.33), can be rewritten:

$$G_{i_{sd}}(p) = \frac{1}{1 - 0.5T_sp} \frac{1}{2\left(T_{i_{sd}(ol)}^{eq}p\right)^2 + 2T_{i_{sd}(ol)}^{eq}p + 1} \quad (3.35)$$

Second order term in (3.35) is much smaller than unity, therefore it is reasonable to neglect it. Hence, equivalent time constant of entire current control loop can be determined:

$$T_{i_{sd}}^{eq} = -0.5T_s + 2T_{i_{sd}(ol)}^{eq} = 0.9ms \quad (3.36)$$

Approximated transfer function of the inner loop is expressed, eventually:

$$G_{i_{sd}}(p) = \frac{1}{T_{i_{sd}}^{eq}p + 1} \quad (3.37)$$

According to controlled system given in case of current control loop, flux loop consists of only one delay, related to digital calculation. Block diagram presenting the system, is depicted in Fig. 3.8.
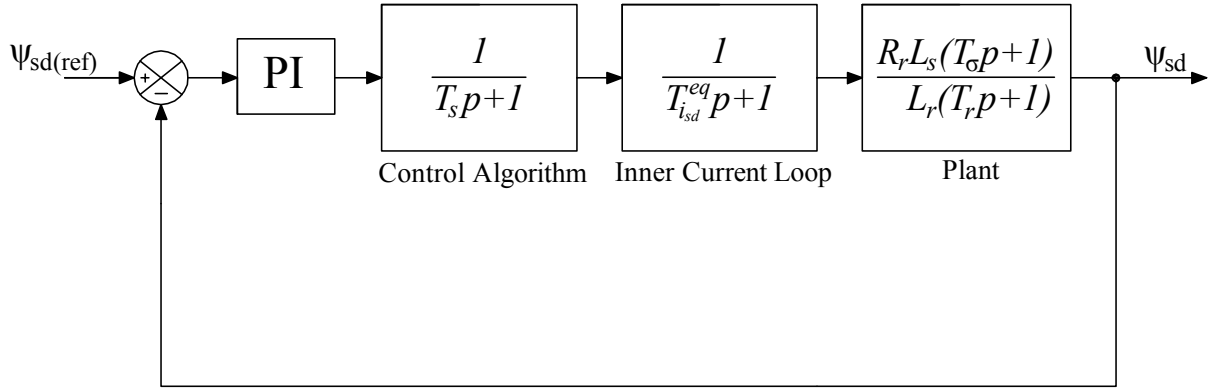
Figure 3.8: *Block diagram of the flux close-loop with regulator to be tuned.*

Corresponding to Fig. 3.8, open-loop transfer function is given:

$$G_{\psi(ol)}(p) = K_{p\psi} \frac{1 + p\tau_\psi}{p\tau_\psi} \frac{1}{T_sp + 1} \frac{1}{T_{i_{sd}}^{eq}p + 1} \frac{R_r L_s}{L_r} \frac{(T_\sigma p + 1)}{(T_r p + 1)} \quad (3.38)$$

In order to analyse the system, and find coefficient of the controller, transfer function is simplified. Its numerator can be expressed similarly to (3.34):

$$(1 + T_\sigma p)(1 - T_\sigma p) = 1 - 0.25T_\sigma^2p^2 \approx 1 \quad \Rightarrow \quad T_\sigma p + 1 = \frac{1}{1 - T_\sigma p} \quad (3.39)$$

Hence, transfer function of the plant becomes of a form:

$$G_{\psi(plant)}(p) = \frac{R_r L_s}{L_r} \frac{1}{T_r p + 1} \frac{1}{1 - T_\sigma p} = \frac{R_r L_s}{L_r} \frac{1}{T_r T_\sigma p^2 + (T_r - T_\sigma)p + 1} \approx \frac{R_r L_s}{L_r} \frac{1}{T_\psi p + 1}$$
(3.40)

where,

$$T_\psi = T_r - T_\sigma$$

Now, the open-loop transfer function (3.38), can be reformulated, and be a basis for further analyses:

$$G_{\psi(ol)}(p) = K_{p\psi} \frac{1 + p\tau_\psi}{p\tau_\psi} \frac{1}{T_s p + 1} \frac{1}{T_{i_{sd}}^{eq} p + 1} \frac{R_r L_s}{L_r} \frac{1}{T_\psi p + 1}$$
(3.41)

In order to determine coefficients of the PI_ψ, *symmetric optimum criterion* ([13], [17]) is applied. Since equivalent time constant of the plant T_ψ is large ($T_\psi = 97.5 ms$), expression for the plant can be reduced further [17]:

$$G_{\psi(ol)}(p) = K_{p\psi} \frac{1 + p\tau_\psi}{p\tau_\psi} \frac{1}{T_s p + 1} \frac{1}{T_{i_{sd}}^{eq} p + 1} \frac{R_r L_s}{L_r} \frac{1}{T_\psi p}$$
(3.42)

In the open-loop transfer function of the system (3.41), exist two more defined components: $1/(T_s p + 1)$ and $1/(T_{i_{sd}}^{eq} p + 1)$ which time constants are much smaller than one of the plant (T_ψ). Thus, these two first-order elements can be reduced, accordingly [17]:

$$G_{\psi(ol)}(p) = K_{p\psi} \frac{1 + p\tau_\psi}{p\tau_\psi} \frac{1}{T_\psi^{eq} p + 1} \frac{R_r L_s}{L_r} \frac{1}{T_\psi p}$$
(3.43)

where,

$$T_\psi^{eq} = T_s + T_{i_{sd}}^{eq}$$

Consequently, integral time constant of the PI_ψ is obtained, as:

$$\tau_\psi = 4 T_\psi^{eq}$$
(3.44)

Subsequently, proportional gain is tuned, and set of the controller coefficients is found:

$$K_{p\psi} = 19.3398, \quad K_{i\psi} = 4395.4, \quad \tau_\psi = 0.0044$$
(3.45)

In order to study the behaviour of the regulator, response of the flux control loop to the step command is plotted (Fig. 3.9).

Properties of the control loop are obtained:

$$t_{r(10\%-90\%)} = 6.89 ms, \quad t_{s(2\%)} = 93.10 ms, \quad M_p = 50.1\%$$
(3.46)

Comparing (3.46) to characteristics of corresponding current regulator ($PI_{i_{sd}}$), given in (3.26), rising time is about seven times larger. Its time reaction is in an appropriate level. In

Figure 3.9: *Step response of the system with designed stator flux controller. Typical characteristics are marked: rising time $(t_{r(10\%-90\%)}) = 6.89ms$, settling time $(t_{s(2\%)}) = 93.10ms$ and the maximum overshoot $(M_p) = 50.1\%$. Value '1' on the 'Amplitude' axis denotes arbitrary chosen stator flux reference, applied to the control system.*

Figure 3.10: *Pole-zero map of the stator flux close-loop, including designed regulator. Result indicates stability of the system - all zeros and poles are placed on the left half of the complex plain. Zeros are determined by circles, while poles by crosses.*

the given step response (Fig. 3.9) is observed very high overshoot, which is the consequence of the chosen criterion [13], [17]. However, that drawback is overcome by current limitation.

Similarly to the current controller, it can be concluded, that the system and designed regulator work stable. Response to the step input stabilises. For additional confirmation, pole-zero map of the flux control loop is plotted in Fig. 3.10.

3.3.3   q-axis current loop

Like in previous subsections, transfer function of the object to be controlled has to be determined. Solution starts with (3.6), however, ψ_{sq}^e is not omitted:

$$u_{sq}^e = R_s i_{sq}^e + p\psi_{sq}^e + \omega_e \psi_{sd}^e \tag{3.47}$$

Then (3.10) is placed into (3.47):

$$u_{sq}^e = R_s i_{sq}^e + p(L_s i_{sq}^e + L_m i_{rq}^e) + \omega_e \psi_{sd}^e \tag{3.48}$$

In order to get rid of the rotor current component, (3.8) is used:

$$u_{sq}^e = (R_s + pL_s)i_{sq}^e - p^2\frac{L_m}{R_r}\psi_{rq}^e - p\frac{L_m}{R_r}(\omega_e - \omega_r)\psi_{rd}^e + \omega_e \psi_{sd}^e \tag{3.49}$$

Rotor flux q-component appearing in (3.49), can be determined by q-component of stator current: $\psi_{rq}^e = i_{sq}^e(L_m - L_r L_s/L_m)$. Putting that expression into (3.49), yields:

$$u_{sq}^e = (R_s + pL_s)i_{sq}^e - p^2\frac{L_m}{R_r}\left(L_m - \frac{L_r L_s}{L_m}\right)i_{sq}^e - p\frac{L_m}{R_r}(\omega_e - \omega_r)\psi_{rd}^e + \omega_e \psi_{sd}^e \tag{3.50}$$

Phrase: $p(L_m/R_r)(\omega_e - \omega_r)\psi_{rd}^e + \omega_e\psi_{sd}^e$ from (3.50) is considered as a disturbance, and is omitted in the analysis. However, the coupling exists in the real system, therefore the behaviour of the regulator defined on the basis of the simplified transfer function, is verified during tests of entire control algorithm.

After several mathematical computational steps, the following result can be obtained:

$$u_{sq}^e = i_{sq}^e R_s \left(\frac{L_\sigma}{R_r R_s}p^2 + \frac{L_s}{R_s}p + 1\right) \tag{3.51}$$

Finally, transfer function of the plant is found:

$$G_{i_{sq}(plant)}(p) = \frac{i_{sq}^e}{u_{sq}^e} = \frac{1}{R_s}\frac{1}{\sigma T_{st}T_r p^2 + T_{st}p + 1} \tag{3.52}$$

where,
$T_{st} = L_s/R_s$ is the stator time constant.

System modelled in q-axis current loop, consist of exactly the same delays presented in section 3.3.1. Hence, it might be also represented in the block diagram, as it is shown in Fig. 3.11 (system with sensor delay in the feedback is already replaced by its equivalency with unity feedback).
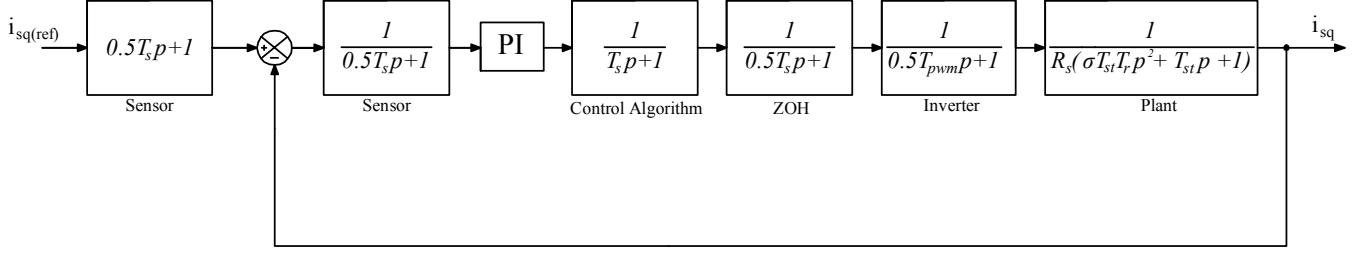
Figure 3.11: *Block diagram of the i_{sq} current close-loop with regulator to be tuned.*

Similarly to conclusion obtained in section 3.3.1, anti-alias prefilter is not required, and its presence can be avoided.

From structure of the system given in Fig. 3.11, open-loop transfer function can be formed:

$$G_{i_{sq}(ol)}(p) = K_{pi_{sq}} \frac{1 + p\tau_{i_{sq}}}{p\tau_{i_{sq}}} \frac{1}{0.5T_s p + 1} \frac{1}{T_s p + 1} \frac{1}{0.5T_s p + 1} \frac{1}{0.5T_{pwm} p + 1} \frac{1}{R_s \left(\sigma T_{st} T_r p^2 + T_{st} p + 1\right)}$$

(3.53)

Determining parameters of the $PI_{i_{sq}}$, starts with zero selection. As in previous cases, it is used to cancel the slowest pole of the system (to make the dynamic response improved). In the discussed loop, it is one of poles of the plant ($T_{i_{sq}(1)} = 10.9ms$, $T_{i_{sq}(2)} = 55.6ms$). It yields:

$$\tau_{i_{sq}} = T_{i_{sq}(2)}$$

(3.54)

Proportional gain is determined with utility of *magnitude optimum criterion*, where the damping ratio is set $\zeta = \frac{\sqrt{2}}{2} = 0.707$ [13]. Eventually, all the parameters are chosen:

$$K_{pi_{sq}} = 8.4409, \quad K_{ii_{sq}} = 150.7304, \quad \tau_{i_{sq}} = 0.056$$

(3.55)

In order to examine the controller behaviour, response of the system to the step command is checked, and the result is presented in Fig. 3.12. It results in the control loop characteristics:

$$t_{r(10\%-90\%)} = 36.1ms, \quad t_{s(2\%)} = 94.7ms, \quad M_p = 3.35\%$$

(3.56)

Verification of the stability is made on the basis of pole-zero map of the control loop, presented in Fig. 3.13. Since all the poles and zero are placed on the left half of the complex plain, it is concluded that system is driven stably. Also demand for the controller is fulfilled, as $M_p = 3.35\% < 4\%$. However, comparing properties of two current control loops, (3.26) and (3.56), it is easily to note, that $PI_{i_{sq}}$ acts slower than $PI_{i_{sd}}$. Any trials of improving its reaction lead to instability. The reason of that situation, might be much higher affect of the applied load on q-current component (as it is the torque-producing one). Additionally, its
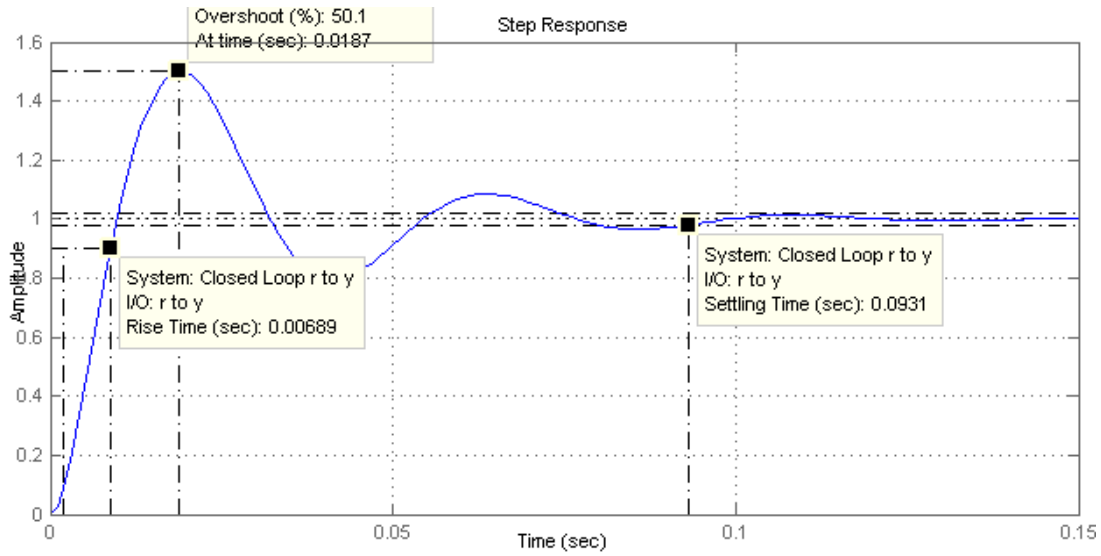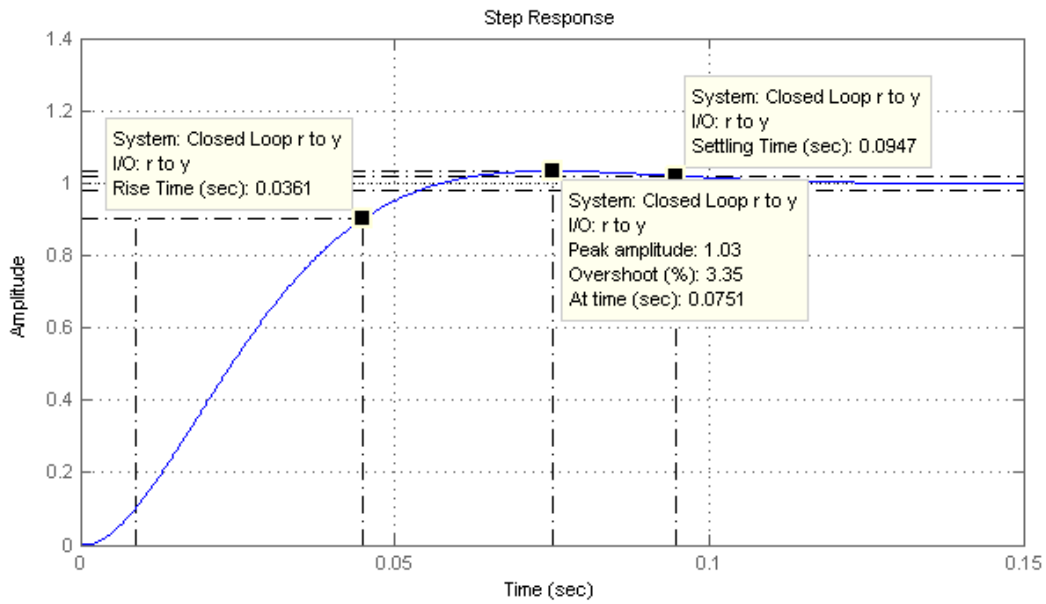
Figure 3.12: *Step response of the system with designed $PI_{i_{sq}}$ controller. Typical characteristics are marked: rising time $(t_{r(10\%-90\%)}) = 36.1ms$, settling time $(t_{s(2\%)}) = 94.7ms$ and the maximum overshoot $(M_p) = 3.35\%$. Value '1' on the 'Amplitude' axis denotes arbitrary chosen q-current reference, applied to the control system.*
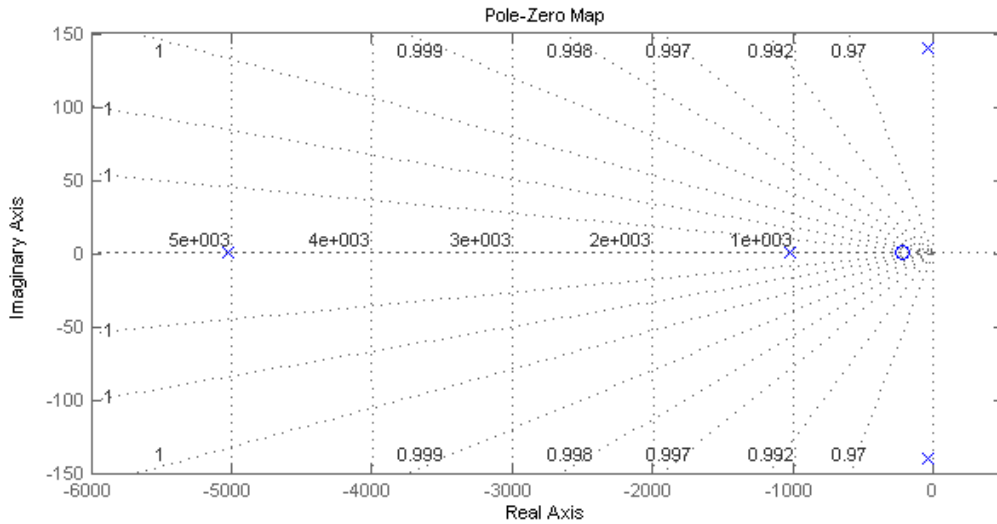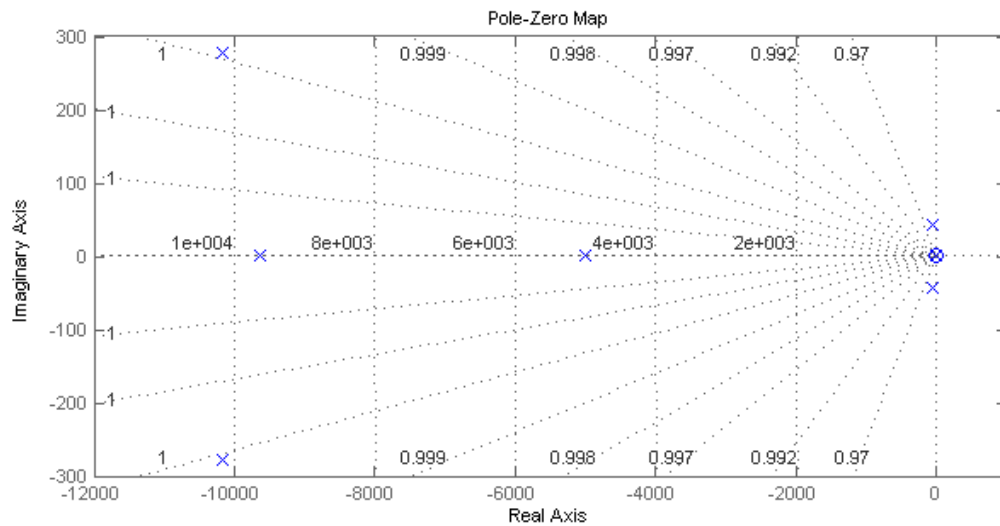

Figure 3.13: *Pole-zero map of the q-current close-loop, including designed regulator. Result indicates stability of the system - all zeros and poles are placed on the left half of the complex plain. Zeros are determined by circles, while poles by crosses.*

controller is designed with *magnitude optimum criterion*, which is not the optimal solution for systems with presence of disturbances [13]. Nevertheless, *symmetric optimum criterion*, which overcomes above drawback, is characterised by very big overshoot, what, in case of current controllers criteria set in the beginning of the section, is unacceptable.

3.3.4   q-axis speed loop

The controlled plant for speed regulator is formulated from (3.13):

$$G_{\omega(plant)}(p) = \frac{M_e}{i_{sq}^e} = \frac{3}{2}p_p\psi_{sd}^e \tag{3.57}$$

To obtain the feedback signal for the speed command, (2.13) is used. Actual design is made for conventional induction motor, which friction constant is negligibly small. Thus, the formula can be reduced:

$$M_e = M_l + Jp\frac{\omega_r^{el}}{p_p} \quad \Rightarrow \quad \omega_r^{el} = (M_e - M_l)\frac{p_p}{Jp} \tag{3.58}$$

where,
$\omega_r^{el} = \omega_r p_p$ is an electrical angular rotor speed.

However, the resulting speed depends also on the load torque, which is treated as the disturbance. Therefore, the procedure applied to design speed controller, slightly differ from previously utilised. Nevertheless, first, transfer function of the inner current loop has to be formulated. It begins from calculating equivalent open-loop time constant. As, only the slowest pole of the plant of q-current loop is cancelled by its regulator, the second one is included in equivalent time constant computation:

$$T_{i_{sq}(ol)}^{eq} = T_{i_{sq}(1)} + 0.5T_s + T_s + 0.5T_s + T_{pwm} = 11.4ms \tag{3.59}$$

Close-loop transfer function of the system given in Fig. 3.11, with calculated equivalent time constant is formulated, as:

$$G_{i_{sq}(cl)}(p) = \frac{1}{2\left(T_{i_{sq}(ol)}^{eq}p\right)^2 + 2T_{i_{sq}(ol)}^{eq}p + 1} \tag{3.60}$$

Including the system element appeared before the node (Fig. 3.11) into to transfer function of entire q-current loop, yields:

$$G_{i_{sq}}(p) = (0.5T_sp + 1)\frac{1}{2\left(T_{i_{sq}(ol)}^{eq}p\right)^2 + 2T_{i_{sq}(ol)}^{eq}p + 1} \tag{3.61}$$

Accordingly to the assumption (3.34), (3.61) can be rewritten:

$$G_{i_{sq}}(p) = \frac{1}{1 - 0.5T_sp}\frac{1}{2\left(T_{i_{sq}(ol)}^{eq}p\right)^2 + 2T_{i_{sq}(ol)}^{eq}p + 1} \tag{3.62}$$

Second order component in (3.62) is much smaller than unity, and can be neglected. Thus, $G_{i_{sq}}(p)$ is reduced to first-order system. Time constant of entire q-current loop is computed:

$$T_{i_{sq}}^{eq} = -0.5T_s + 2T_{i_{sq}(ol)}^{eq} = 22.7ms \tag{3.63}$$

And resulting, approximated transfer function is:

$$G_{i_{sq}}(p) = \frac{1}{T_{i_{sq}}^{eq}p + 1} \tag{3.64}$$

As the system is run sensorless (Fig. 3.2), there is no sensor providing feedback for the control algorithm (no delay in the feedback). The only one time delay considered in actual process is related to digital calculations. But, as it is mentioned previously, system and the design procedure differ, due to disturbance signal consideration, as it is visible in Fig. 3.14.
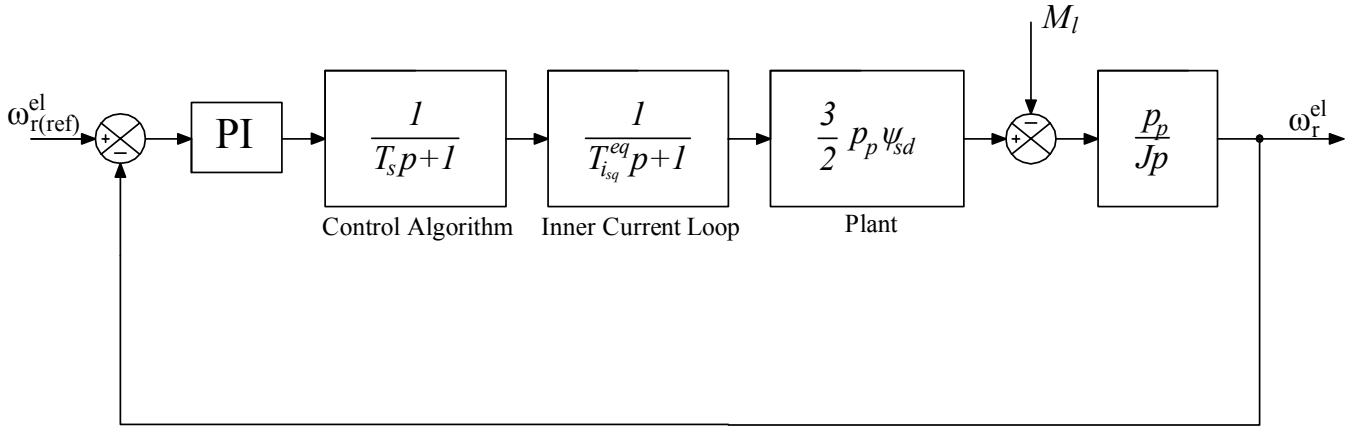
Figure 3.14: *Block diagram of the speed close-loop with regulator to be tuned. Load torque disturbance is added to the system.*

Analysed system is considered linear, thus it is resolved with superposition usage [10]. First ω_r^{el} is treated as an input of the system, and M_l is set to zero. Afterwards, input torque is examined, while the speed is kept zero.

In the first case, only proportional part of the regulator is utilised [10], as it is shown in Fig. 3.15.

Open-loop transfer function of the system given in Fig. 3.15, is formulated:

$$G_{\omega(ol)}(p) = K_{p\omega} \frac{1}{T_s p + 1} \frac{1}{T_{i_{sq}}^{eq}p + 1} \frac{3}{2} p_p^2 \psi_{sd}^e \frac{1}{Jp} \tag{3.65}$$

By defining equivalent time constant,

$$T_\omega^{eq} = T_s + T_{i_{sq}}^{eq} \tag{3.66}$$

transfer function in (3.65), can be simplified to the first-order system:
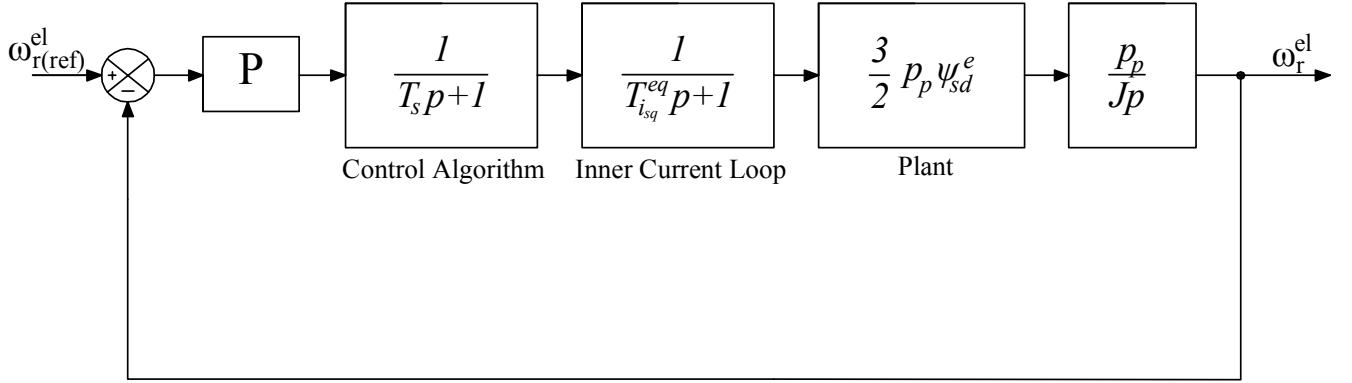
Figure 3.15: *Block diagram of the speed close-loop with regulator to be tuned. Only speed input is taken into account.*

$$G_{\omega(ol)}(p) = K_{p\omega} \frac{1}{T_\omega^{eq} p + 1} \frac{3}{2} p_p^2 \psi_{sd}^e \frac{1}{Jp} \tag{3.67}$$

In order to find optimal solution, *magnitude optimum criterion* is used. Tuned coefficient of the controller is given:

$$K_{p\omega} = 0.0383 \tag{3.68}$$

In order to find the parameters of the integral part of the regulator, second case is studied (load torque is considered as an input to the system, while speed is set to zero). That situation is observed in Fig. 3.16
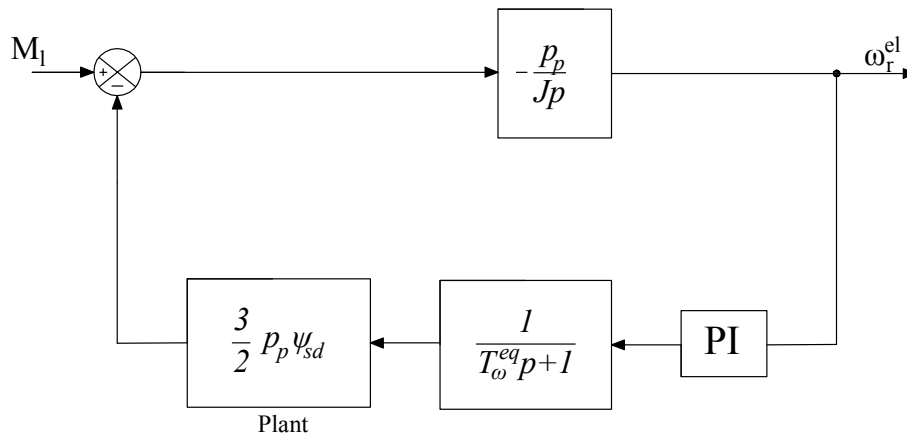
Figure 3.16: *Block diagram of the speed close-loop with regulator to be tuned. Load torque is considered as an input to the system, while speed is set to zero.*

Control scheme presented in Fig. 3.16, is described by the following transfer function:

$$\frac{\omega_r(p)}{M_l(p)} = \frac{-\frac{p_p}{Jp}}{1 + \left(-\frac{p_p}{Jp}\right)\left(-\frac{3}{2}p_p\psi_{sd}^e\frac{1}{T_\omega^{eq}p+1}K_\omega\frac{1+\tau_\omega p}{\tau_\omega p}\right)} \tag{3.69}$$

After several mathematical manipulations (3.69) is reduced to:

$$\frac{\omega_r(p)}{M_l(p)} = -\frac{p_p}{J}\frac{2\tau_\omega T_\omega^{eq}p\left(T_\omega^{eq}p+1\right)}{2\left(T_\omega^{eq}\right)^2\tau_\omega p^3 + 2T_\omega^{eq}\tau_\omega p^2 + \tau_\omega p + 1} \tag{3.70}$$

Due to the character of the studied system, *symmetric optimum criterion* is chosen to determine the time constant of the integral controller:

$$\tau_\omega = 4T_\omega^{eq} \tag{3.71}$$

Complete set of sought coefficients of PI_ω is given:

$$K_{p\omega} = 0.0383, \quad K_{i\omega} = 0.4163, \quad \tau_\omega = 0.0920 \tag{3.72}$$

In order to examine the stability in case of disturbance (load torque) presence, pole-zero map of (3.70) is plotted, and presented in Fig. 3.17. It shows that, all poles (determined by the crosses) are placed in the left part of the plain, what indicates stability of the system.

Figure 3.17: *Pole-zero map of the speed close-loop with consideration of the load torque. Result indicates stability of the system. Zeros are determined by circles, while poles by crosses.*

Properties of the designed speed regulator are studied with step response of control loop, while disturbance is not considered. The result is shown in Fig. 3.18. Characteristics of the loop, are listed below:

$$t_{r(10\%-90\%)} = 49.2ms, \quad t_{s(2\%)} = 380ms, \quad M_p = 43.2\% \tag{3.73}$$

Figure 3.18: *Step response of the system with designed controller, without load torque input consideration. Typical characteristics are marked: rising time $(t_{r(10\%-90\%)}) = 49.2ms$, settling time $(t_{s(2\%)}) = 380ms$ and the maximum overshoot $(M_p) = 43.2\%$. Value '1' on the 'Amplitude' axis denotes arbitrary chosen speed reference, applied to the control system.*
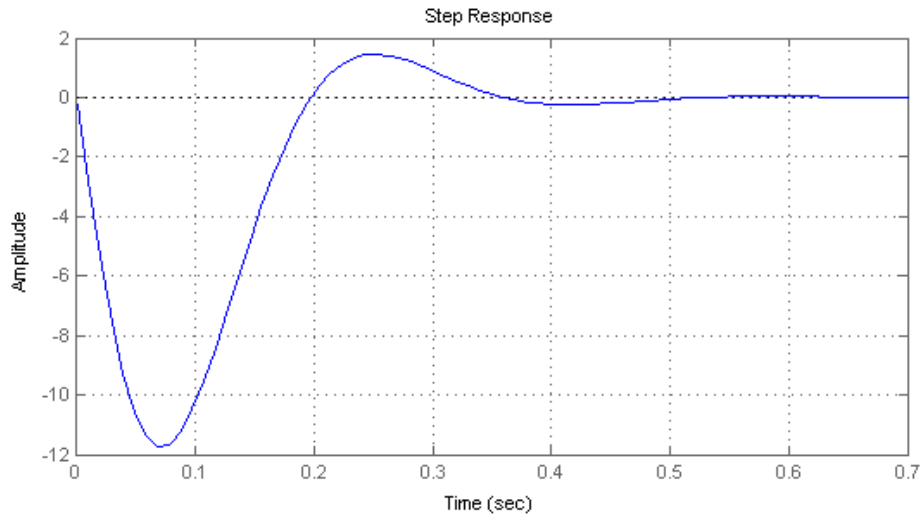

Figure 3.19: *Step response of the system with designed controller. Speed input is set to zero, while command signal is applied to the load torque (disturbance) input. 'Amplitude' axis denotes speed command. Proper rejection of the disturbance is presented, as the signal finally stabilises at zero, which is the set reference speed.*

Requirement for the outer-loop regulators (so does the speed one) is to be slower than corresponding current regulator. Comparing characteristics of speed control loop - (3.73), and corresponding q-current loop - (3.56) , it is noticeable that the current one acts faster.

In order to observe reaction of the controller to the step command in the load torque input, the response is plotted (according to the system given in Fig. 3.16), and presented in Fig. 3.19. It is visible that control loop is characterised by very big, negative overshoot. However, it eventually reaches steady state, what indicates stability and ability to reject disturbance signals.

3.3.5 Integrator antiwindup

Each of the designed controller outputs has to be limited, to prevent the hardware from damaging (for example from overcurrent or overvoltage appearance). That limitations causes nonlinearities in the system. When output of the regulator is high enough, signal sent to the controlled object becomes equal to the saturation level. That situation leads to keeping the integral part integrating the supplied error. It results in rising (winding up) the output of the controller. It lasts until plant feedback exceeds reference value, and negative error appears in the input of PI. That change effects in high output of the integral part compensating previously grown error. It causes overshoots in the responses, and if the signal was saturated for significant amount of time, it would even deteriorate the control, and system would become unstable.

Therefore to overcome that situation, antiwindup part is added to each controller [11]. Its basic structure is presented in Fig. 3.20.
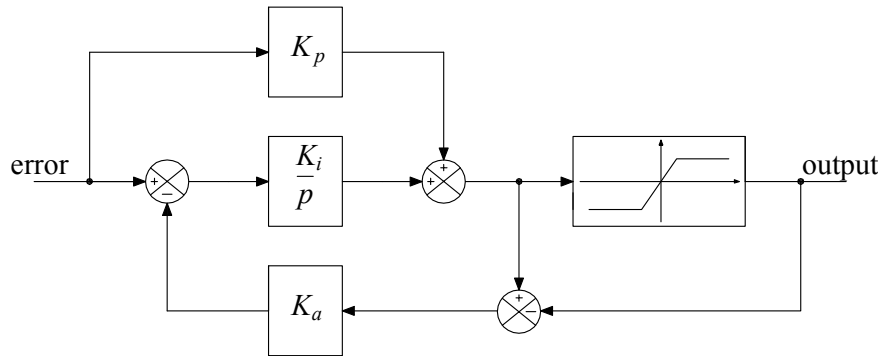
Figure 3.20: *Integrator antiwindup technique, to cancel the effect of the saturations.*

Antiwindup gains should be selected to keep the input of the integrator relatively small, whenever the saturation occurs [11]. Hence, respective gains are chosen:

$$K_{ai_{sd}} = 5 \tag{3.74}$$
$$K_{a\psi} = 10 \tag{3.75}$$
$$K_{ai_{sq}} = 100 \tag{3.76}$$
$$K_{a\omega} = 90 \tag{3.77}$$

3.4 Stator flux observer

Introduction to the chapter indicates that the crucial part of the stator field oriented control is precise knowledge about stator flux magnitude and its actual position. As the design is focused on preparing the algorithm able to run the motor sensorless, flux information can be estimated. In case of stator field orientation, it is realised by simple expression - (1.2). Beside its simplicity, problems related to the signal integration are known. In physical implementation, the result of the ideal integration is affected by the dc-offset, and dc-drift [20]-[24]. Source of the first problem comes from non-perfect measurements of current or/and voltages, while the second one exists because of the initial conditions of the integral. Considering $x(t)$ as the ideal, arbitrary signal to integrate, corresponding measured one is always introduced with dc-offset (due to imperfection of used sensors). Therefore, after its integration, one can obtain:

$$\int x_{meas}(t)dt = \int \left[x(t) + x_{off} \right] dt = y(t) + t x_{off} + C \qquad (3.78)$$

where,
$y(t)$ is the integral of $x(t)$,
x_{off} is the offset value of the measured signal,
C is the constant value resulting from initial conditions of the integral.

Also, in order to obtain desired flux information, it is required to know exact value of the stator resistance. However, its influence is dominating at low speed range, while in high speed case the problem vanishes.[20]. Thus, it is not investigated any further.

There are several solutions discussed in the literature, proposed to overcome described drawbacks. Among them, three are picked:

- low-pass filter (LPF) based model,

- high-pass filter (HPF) based model,

- voltage-current model.

All of them present good results over wide speed range. However, there are few specific characteristics, which are taken into account. In case of LPF-based, in order to compensate phase and magnitude distortions, interior feedback loop is designed together with PI regulator [21]. It leads to another tuning procedure, what rises complexity of the process. Suggestion for avoiding that, is using programmable LPF, with its pole dependency on the actual speed [20], [22]. Nevertheless, that solution is not studied deeper.

Voltage-current model provides very good estimation [12], [21]. But, again it consists of PI controller. Additionally, it requires rotor speed/position feedback, which in case of sensorless control needs very precise estimator. Small errors in the velocity estimation would be amplified further in the flux calculations.

Solution applied by HPF-based model, similarly to LPF-base one, requires phase and magnitudes compensators. However, there is no need for feedback loop, neither the additional

controller [21], [23]. Therefore, for final investigation and eventual implementation, HPF-based model is chosen.

Among the proposed structures of the estimator, basic architecture is adopted [23]. Its representation is shown in Fig. 3.21.
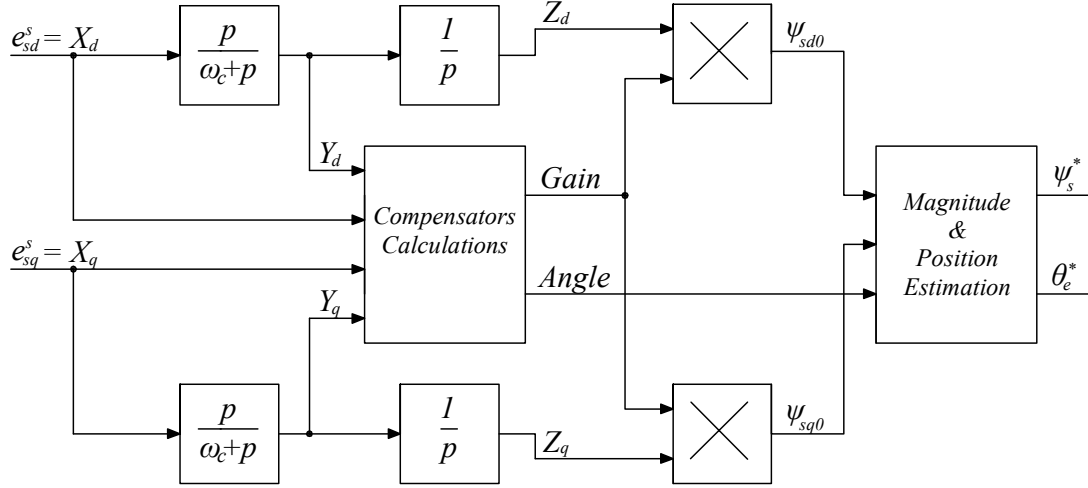
Figure 3.21: *Basic structure of the HPF-based model of the stator flux estimator [23].*

The reason of usage high-pass filters is to get rid of the dc-offset in the signal to be integrated. Applied filters are first order filters, hence signal with lower frequencies than cut-off frequency are not completely attenuated. Therefore, after passing filtered out signal through pure integrator, flux can be reconstructed with phase and gain compensators, as it is visible in Fig. 3.21.

In order to evaluate the observer, set of formulas has to be introduced. First, the high-pass filter is defined. It can be given by means of transfer function:

$$HPF(p) = \frac{p}{p + \omega_c} \tag{3.79}$$

where,
$\omega_c = 2\pi f_c$
and,
f_c is the cut-off frequency.

Afterwards, parameters of the compensators, are calculated:

$$Gain = \sqrt{\frac{X_d^2 + X_q^2}{Y_d^2 + Y_q^2}} \tag{3.80}$$

$$Angle = atan2\left(sin\left(\theta_y - \theta_x\right), cos\left(\theta_y - \theta_x\right)\right) \tag{3.81}$$

where,
X_d, X_q are the signals applied to HPFs (back EMFs),

Y_d, Y_q are the outputs of HPFs,
θ_x, θ_y are the angles of back EMF, before and after HPFs, respectively.

Positions: θ_x, θ_y, used in (3.81), are given as:

$$\theta_x = atan2\left(X_q, X_d\right) \tag{3.82}$$

$$\theta_y = atan2\left(Y_q, Y_d\right) \tag{3.83}$$

Calculated compensators (3.80), (3.81) are used to determine the desired stator flux information:

$$\widehat{\psi_s^*} = \sqrt{\psi_{sd0}^2 + \psi_{sq0}^2} \tag{3.84}$$

$$\theta_e^* = atan2\left(sin\left(\theta_{e0} - Angle\right), cos\left(\theta_{e0} - Angle\right)\right) \tag{3.85}$$

where,
$\psi_{sd0} = Gain \cdot Z_d$
$\psi_{sq0} = Gain \cdot Z_q$
$\theta_{e0} = atan2\left(\psi_{sq0}, \psi_{sd0}\right) = atan2(Z_q, Z_d)$
and,
Z_d, Z_q are the outputs of pure integrator of d and q axis, respectively.

Besides its simplicity, simulation tests give unaccepted results. The reason of that, might be presence of derivations in the inputs of the observer (caused by the HPFs). As it is suggested to avoid any derivative parts, idea presented in [24] is utilised. Looking again into transfer function of high-pass filter, it can be rephrased, in a certain way:

$$HPF(p) = \frac{p}{p + \omega_c} = \frac{p + \omega_c - \omega_c}{p + \omega_c} = 1 - \frac{\omega_c}{p + \omega_c} \tag{3.86}$$

Simple mathematical manipulation introduced in (3.86), shows that HPF can be introduced by its equivalency containing low-pass filter. In that way, undesirable derivatives disappear.

Proper working of the estimator is assured, when cut-off frequency of filters fulfil two conditions [23]. It has to be much higher than inverse of stator time constant of the motor to be driven, and it ought to be lower than sampling frequency. Observing responses for few values of cut-off frequency, finally it is set to $\omega_c = 1500 rad/s$, what corresponds to $f_c = 238.73Hz$. Below, comparison with fulfilled requirements is done:

$$\frac{1}{T_{st}} = \frac{R_s}{L_s} = 15.03Hz \ll f_c = 238.73Hz < f_s = 5000Hz \tag{3.87}$$

The performance of the derived observer is shown together with drive simulation, which is done in section 3.6.

3.5   Speed estimator

Next to observer described in previous subsection, there is a request for speed estimator, in order to fulfil sensorless control demand. As in case of asynchronous motor exists slip, which introduces difference between rotor speed and synchronous speed, sought estimation of the velocity can be determined:

$$\omega_r^* = \omega_e^* - \omega_{sl}^* \tag{3.88}$$

where,
$\omega_r^*, \omega_e^*, \omega_{sl}^*$ are the rotor, synchronous and slip angular speed estimations, respectively.

Synchronous speed estimation can be obtained from steady-state approximation [28]:

$$p\overline{\psi}_s \approx j\omega_e\overline{\psi}_s \Rightarrow \omega_e = \frac{1}{j\overline{\psi}_s}p\overline{\psi}_s \tag{3.89}$$

After mathematical manipulation, final formula for synchronous angular speed is achieved:

$$\omega_e^* = \frac{\psi_{sd}^{s*}p\psi_{sq}^{s*} - \psi_{sq}^{s*}p\psi_{sd}^{s*}}{(\widehat{\psi}_s^*)^2} = \frac{\psi_{sd}^{s*}e_{sq}^{s*} - \psi_{sq}^{s*}e_{sd}^{s*}}{(\widehat{\psi}_s^*)^2} \tag{3.90}$$

where,
$\psi_{sd}^{s*}, \psi_{sq}^{s*}$ are the estimated stator flux d and q components, respectively,
e_{sd}^{s*}, e_{sq}^{s*} are the estimated back EMF d and q components, respectively.

Similarly to synchronous angular speed, slip has to be introduced by typical, electrical measurements. Therefore, analysis begins from *simplified Kloss formula*, linking slip and the produced torque [17]:

$$M_e = M_k\frac{2}{\left(\frac{\omega_{sl}}{\omega_{slk}}\right)^2 + \left(\frac{\omega_{slk}}{\omega_{sl}}\right)^2} \tag{3.91}$$

where,
M_k is the breakdown torque,
ω_{slk} is the breakdown angular slip velocity.

In case of high speeds, actual slip becomes much smaller than the breakdown one: $\omega_{sl} \ll \omega_{slk}$. Thus, expression (3.91) can be further simplified [17]:

$$\frac{M_e}{M_k} = \frac{2\omega_{sl}}{\omega_{slk}} \tag{3.92}$$

Breakdown torque is given by the relation:

$$M_k \sim \left(\frac{u_s}{\omega_e}\right)^2 \approx \psi_s = const \tag{3.93}$$

It is valid, if $R_s = 0$. In high speed region, effect of the resistance diminishes, therefore (3.93) provides that breakdown torque remains constant. Additionally, (3.91) is applicable to any torque, also, the nominal one [25]. It yields:

$$\frac{M_e}{M_{eN}} = \frac{\omega_{sl}}{\omega_{slN}} \tag{3.94}$$

where,
M_{eN} is the nominal electromagnetic torque,
ω_{slN} is the nominal slip angular speed.

In order to determine the actual torque of the motor, utilising only standard measurements, method described in [26] is used. The idea of the solution is to determine stator flux space vector in the rotating reference frame oriented with $\overline{u}_{s\psi}$ space vector ($\overline{u}_{s\psi}$ is aligned with its d-component), which is defined as following:

$$\overline{u}_{s\psi} = j\omega_e \overline{\psi}_s \tag{3.95}$$

Chosen orientation, yields:

$$\overline{u}_{s\psi} = u^e_{sd\psi} \Rightarrow u^e_{sd\psi} = -\omega_e \psi^e_{sq} \Rightarrow \psi^e_{sq} = -\frac{u^e_{sd\psi}}{\omega_e} \tag{3.96}$$

Now, torque can be related to obtained flux, according to the relation:

$$M_e = \frac{3}{2}p_p \Im\left(\overline{\psi}_{s_{conj}} \cdot \overline{i}_s\right) = \frac{3}{2}p_p \Im\left[j\frac{u^e_{sd\psi}}{\omega_e} \cdot \left(i^e_{sd} + ji^e_{sq}\right)\right] = \frac{3}{2}p_p \frac{u^e_{sd\psi}}{\omega_e}i^e_{sd} = const \cdot i^e_{sd} \tag{3.97}$$

where,
$\Im$ indicates imaginary part of the complex number,
$\overline{\psi}_{s_{conj}}$ is the conjugated stator flux space vector.

Result obtained in (3.97), leads to the final solution for the slip angular estimation:

$$\frac{M_e}{M_{eN}} = \frac{i^e_{sd}}{i^e_{sdN}} \Rightarrow \frac{\omega_{sl}}{\omega_{slN}} = \frac{i^e_{sd}}{i^e_{sdN}} \Rightarrow \omega_{sl} = \frac{i^e_{sd}}{i^e_{sdN}}\omega_{slN} \tag{3.98}$$

Additionally, low-pass filters are placed before each estimation ($\omega_r^*, \omega_e^*, \omega_{slip}^*$). Cut-off frequencies are selected by observations of the plotted results of the signals. It yields:

$$LPF_{\omega_e}(p) = \frac{50}{p + 50} \tag{3.99}$$

$$LPF_{\omega_r}(p) = \frac{100}{p + 100} \tag{3.100}$$

$$LPF_{\omega_{slip}}(p) = \frac{100}{p + 100} \tag{3.101}$$

Presented method relies only on the current measurements, and voltage estimations from inverter states, what definitely fulfils sensorless objective.

3.6   Simulation results

Entire designing process is held in continuous domain. However, in order to implement it in the real system, it has to be represented in the discrete domain. Therefore, algorithm is transformed, using *Tustin's method* [11]:

$$p = \frac{2}{T_s} \left(\frac{1 - z^{-1}}{1 + z^{-1}} \right) \tag{3.102}$$

where,
z is the discrete domain operator.

To examine functionality of the algorithm, shown results come from the test of the digitised model. It is tested with the system developed in Chapter 2. Additionally, specific procedure is applied, setting exact working condition of the drive at the particular moment. Below, steps of the procedure are described:

- $T_{sim} = 0..3sec$: motor is started up (with a ramp) to the nominal speed ($n_N = 1430rpm$) - fully loaded;

- $T_{sim} = 3sec$: speed of the motor is reduced to: $n_r = 1000rpm$ - fully loaded;

- $T_{sim} = 6sec$: speed is decreased further, down to: $n_r = 200rpm$ - fully loaded;

- $T_{sim} = 9sec$: speed increases again, up to: $n_r = 1430rpm$ - fully loaded;

- $T_{sim} = 12sec$: speed kept constant: $n_r = 1430rpm$ - no-load test;

- $T_{sim} = 14sec$: speed kept constant: $n_r = 1430rpm$ - full load again.

Middle values for speed reference: $n_r = 1000rpm$ and $n_r = 200rpm$, are arbitrary chosen, to observe behaviours at different speed regions.

Reference stator flux is set to its nominal value:

$$\widehat{\psi}_{s(ref)} = \widehat{\psi}_{sN} = 0.92Wb \tag{3.103}$$

Necessary parameters for running the simulation are listed in Appendix A.

Even if the focus is made on the high speed case, algorithm is also checked with reduced velocity. Additionally, reaction on the disturbance signal (changes in the load torque) is studied. Examinations begins with speed response of the system, plotted in Fig. 3.22.

Waveform shown in Fig. 3.22(a) presents speeds responses to the command one. It is easy to note, that motor, after finite transient time, rotates accordingly to the reference value (blue curve). Additionally, sensorless control is depicted, showing that estimated speed follows the one applied to the control input (green curve). Estimation of synchronous speed is respectively larger (pink curve). In Fig. 3.22(b)-(1) transient during starting up the motor is zoomed. Presence of the oscillations are caused by the load torque. Nevertheless, they diminish, when system reaches steady-state. Fig. 3.22(b)-(2) presents disturbance (load torque) rejection. It takes less than $T_{sim} = 0.1sec$ to track again the command speed. Steady-state error between measured and reference speed is equal to: $n_{r(err)} = 2rpm$.
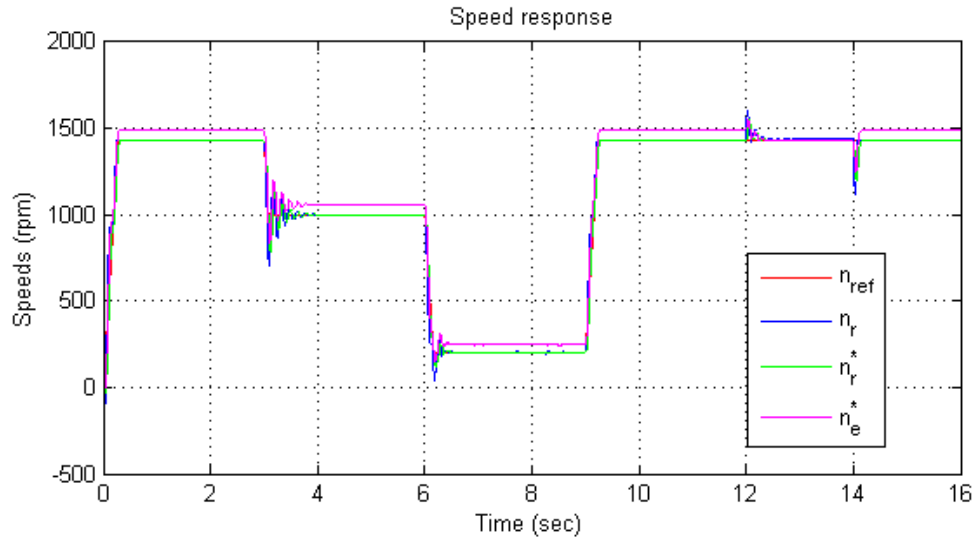
(a) Presentation of overall speed response. Each colour is related to the particular signal: red - reference rotational speed (n_{ref}), blue - measured rotational rotor speed (n_r), green - estimated rotational rotor speed (n_r^*), pink - estimated synchronous rotational speed (n_e^*).
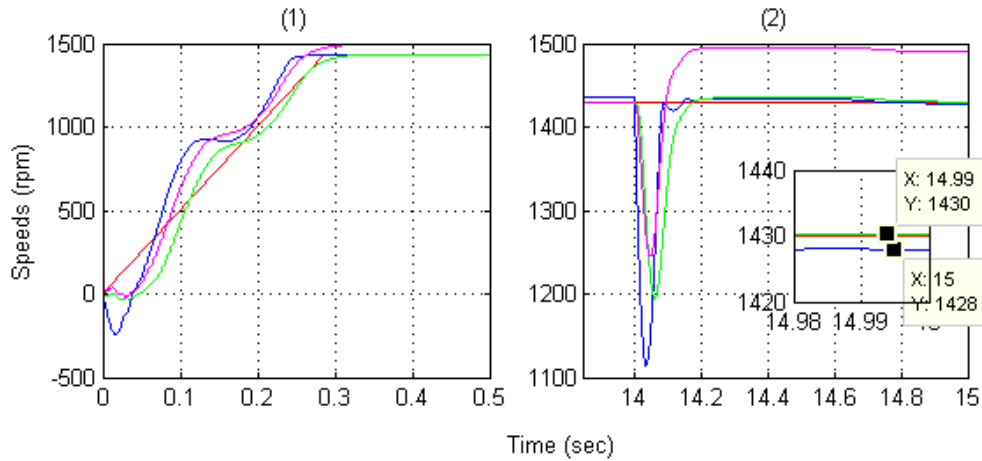
(b) Zooms made on the above plot: (1) - presence of the transient during starting up the motor; visible oscillation due to load torque appearance. (2) - transient after applying again the load torque (in $T_{sim} = 12sec$, load is unplugged), as well the steady-state error.

Figure 3.22: *Speed changes according to applied test procedure.*

In period $T_{sim} = 12..14sec$, motor runs with no-load. However, the rotor speed keeps tracking the reference velocity, what indicates proper work of the regulator. Additionally, synchronous speed decreases, down to the level of the mechanical speed. It is caused by its dependency on currents and voltages. During no-load running, current torque-component diminishes almost to zero, while flux-component remains approximately constant to provide the desired stator flux. It results in significant change of the measured phase currents used to executing the speed estimator.
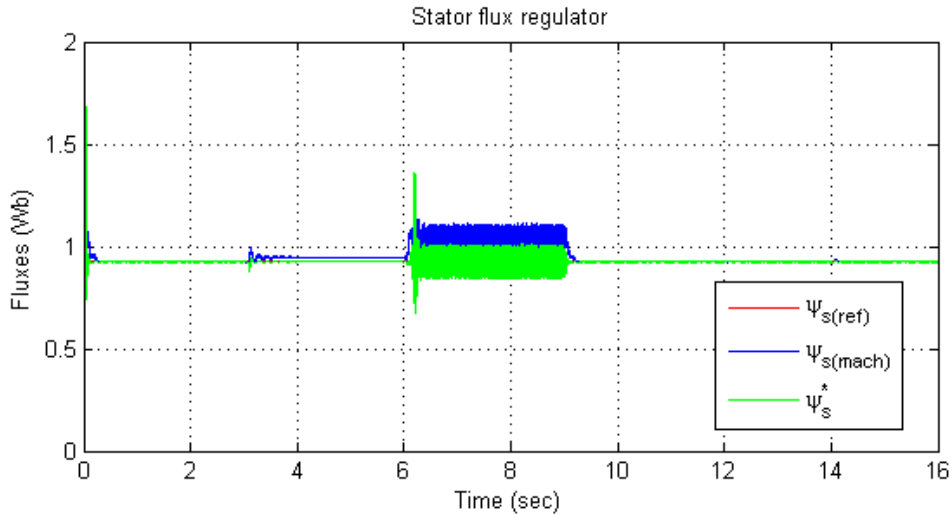
(a) Presentation of overall stator flux changes. Each color is related to the particular signal: red - reference (rated) stator flux ($\psi_{s(ref)}$), blue - stator flux generated inside the motor ($\psi_{s(mach)}$), green - estimated stator flux (ψ_s^*). Signals correspond to their magnitude values.
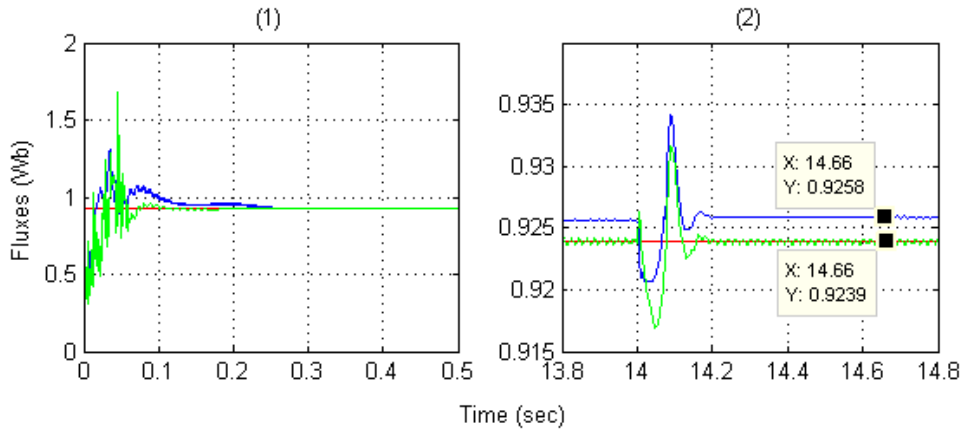
(b) Zooms made on the above plot: (1) - presence of the transient durign starting up the motor; (2) - transient after applying again the load torque (in $T_{sim} = 12sec$, load is unplugged), together with steady-state error.

Figure 3.23: *Stator flux magnitude changes according to applied test procedure.*

Afterwards, work of the flux regulator is studied. Proper graph is presented in Fig. 3.23.

Behaviour through entire test period is shown in Fig. 3.23(b). It is clearly visible, that observed flux is able to track the reference signal, assuring the proper control. Additionally, relation between the speed and the level of accuracy is noticeable - the lower the speed, the worse correctness (it is especially pointed out, when motor is slown down to 200rpm). Nevertheless, steady-state error, for the rated speed becomes negligibly small ($\psi_{s(err)} = 0.0019Wb$), what is seen in Fig. 3.23(b). In future algorithm tests, much higher speeds would be expected, thus it can be concluded, that designed regulator provides stable control.
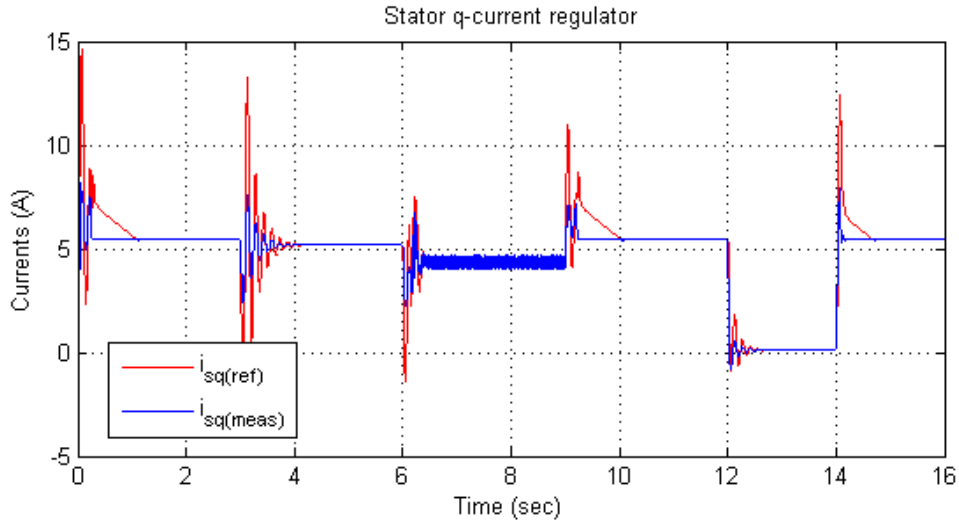
(a) Presentation of overall q-current component changes. Each color is related to the particular signal: red - reference current ($i_{sq(ref)}$), blue - measured current ($i_{sq(meas)}$).

(b) Zooms made on the above plot: (1) - presence of the transient durign starting up the motor; (2) - transient after applying again the load torque (in $T_{sim} = 12s$, load is unplugged).

Figure 3.24: *Stator q-current component changes according to applied test procedure.*

Current regulator analysis begins from presentation responses of the q-current component (Fig. 3.24). Its changes during entire test, are depicted in Fig. 3.24(b). Controlled signal

perfectly tracks command current, what is especially visible in steady-states (proper zooms of two transients and steady-states are shown in Fig. 3.24(b)-(1) and Fig. 3.24(b)-(2)). Small decaying ramps of the reference current (observed in: $T_{sim} \approx 0.3..1.1sec$, $T_{sim} \approx 9.3..10.0sec$ and $T_{sim} \approx 14.2..14.7sec$), are caused by the integrator antiwindups. To avoid overvoltage faults in the inverter, outputs of the current regulators are limited. In that three periods, reference voltages saturates. However, applied antiwindup prevents the signals from getting stuck to the set limitations, providing stable control.
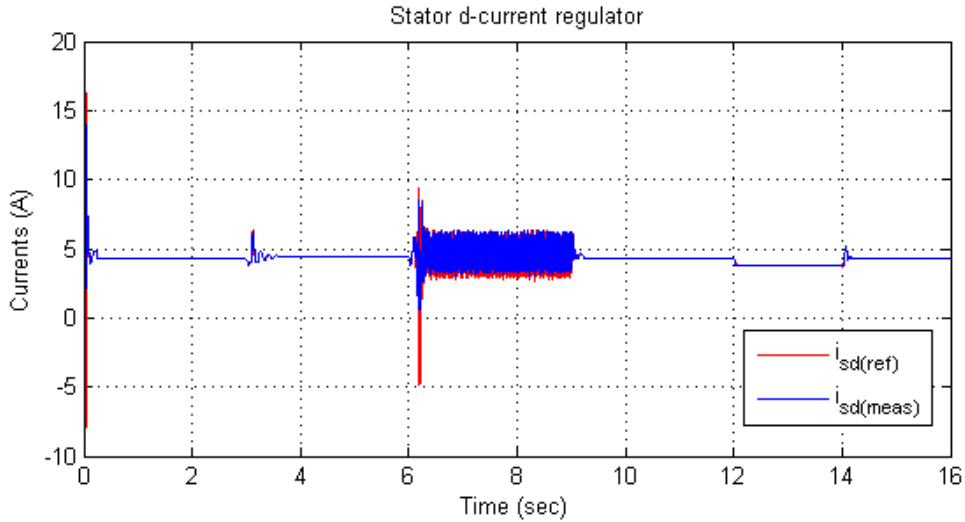
(a) Presentation of overall d-current component changes. Each color is related to the particular signal: red - reference current ($i_{sd(ref)}$), blue - measured current ($i_{sd(meas)}$).
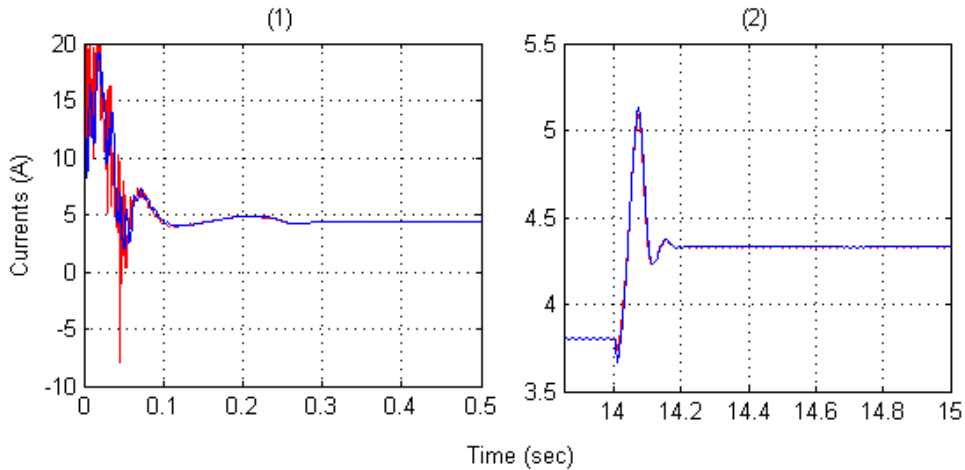
(b) Zooms made on the above plot: (1) - presence of the transient durign starting up the motor; (2) - transient after applying again the load torque (in $T_{sim} = 12s$, load is unplugged).

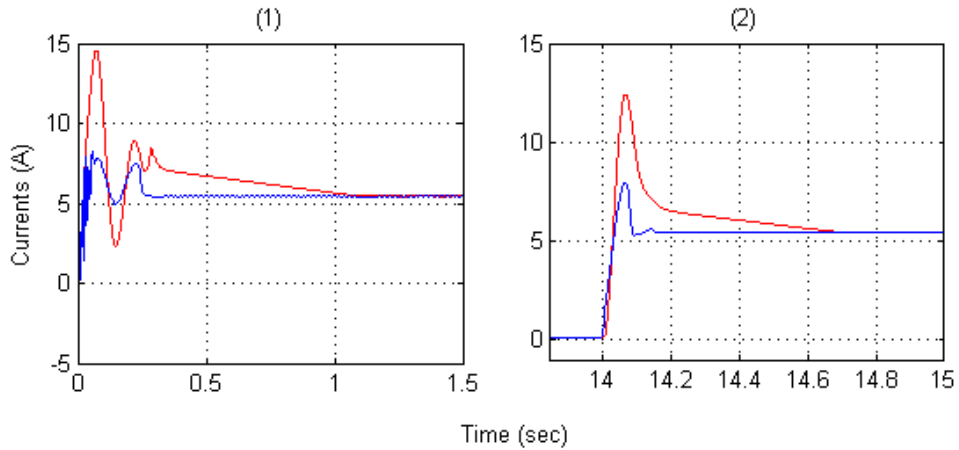**Figure 3.25:** *Stator d-current component changes according to applied test procedure.*

Flux-current component behaviour is examined on the basis of waveforms given in Fig. 3.25. Its variation according to the test scheme is presented in Fig. 3.25(a). The main

objective of the controller is to keep the current level according to the flux reference. Thus, there are almost no changes in steady-state (just small difference, during the motor runs with no load), besides big oscillations in: $T_{sim} = 6..9sec$, when the speed of the machine is reduced down to: $n_r = 200rpm$. That is the consequence of the flux observer dependency on the speed, mentioned previously, which influences in all controlled signals. Besides, regulator acts very good, even during transients (what is pointed out in Fig. 3.25(b)-(1), and Fig. 3.25(b)-(2), respectively).

In case of stator field oriented control, it is important to obtain proper stator flux magnitude and position. The amplitude correctness is shown together with flux regulator analysis in Fig. 3.23, while the position is depicted in Fig. 3.26. Estimated flux angle follows the angle measured in the motor. It is clearly visible in the small window, where positions are indicated when motor is in the steady-state, rotating with the rated speed.
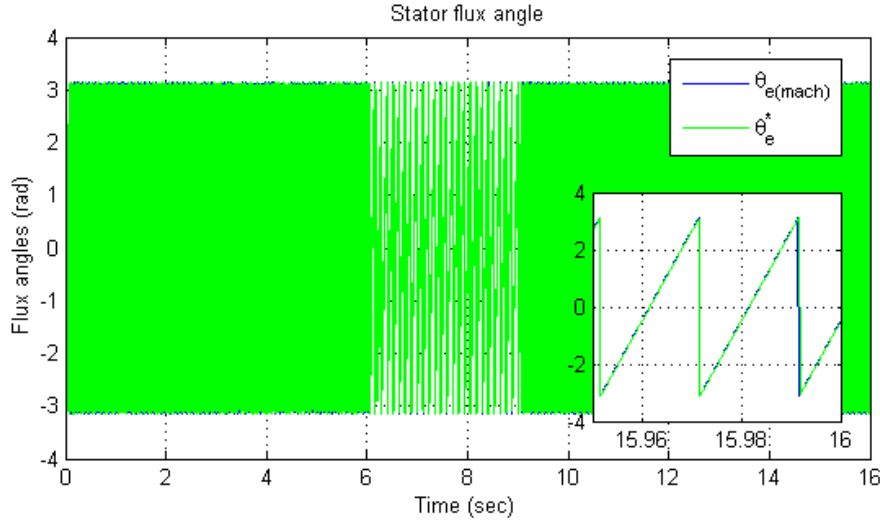
Figure 3.26: *Stator flux angle changes according to applied test procedure. Each color is related to the particular signal: blue - position of the stator flux generated inside the motor ($\theta_{e(mach)}$), green - position of the estimated stator flux (θ_e^*)*

Eventually, presentation of phase voltages and currents is plotted in Fig. 3.27 and Fig. 3.28, respectively. In order to validate correctness of the system, run with the designed algorithm, obtained results are compared with nameplate data. In Fig. 3.27, there are pointed out three values, related to different working points:

- $\widehat{u}_1 = 232.1V$: for $n_r = 1000rpm$, with full load;

- $\widehat{u}_2 = 278.5V$: for $n_r = 1430rpm$, with no load;

- $\widehat{u}_3 = 310.1V$: for $n_r = 1430rpm$, with full load.

It shows the variation of the voltage with changes in speed, so does the torque. However, the examination is done for nominal conditions:

$$u_{RMS(3)} = \frac{\widehat{u}_3}{\sqrt{2}} = 219.27V \approx u_N = 220V \qquad (3.104)$$

Difference between the obtained voltage, and the rated one is negligible small, hence the correctness of the system is deduced.
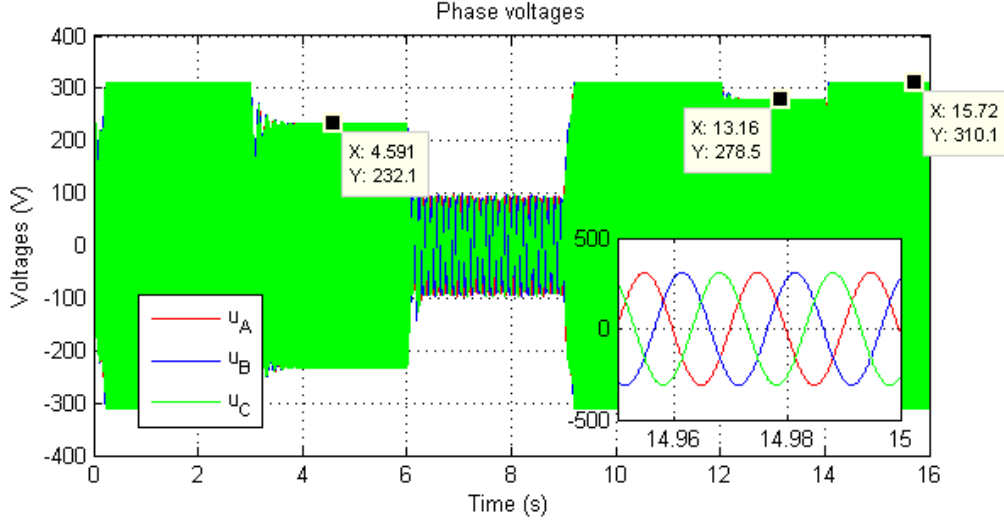
Figure 3.27: *Phase voltages changes according to applied test procedure. Three different magnitude values are spotted: $\widehat{u}_1 = 232.1V$ (for $n_r = 1000rpm$, with full load), $\widehat{u}_2 = 278.5V$ (for $n_r = 1430rpm$, with no load), and $\widehat{u}_3 = 310.1V$ (for $n_r = 1430rpm$, with full load).*

In case of current confirmation, in Fig. 3.28, just two different values are spotted (it is noticeable, that current is kept approximately constant through entire test, except the period, when motor runs with no load):

- $\widehat{i}_1 = 3.806V$: for $n_r = 1430rpm$, with no load;

- $\widehat{i}_2 = 6.949V$: for $n_r = 1430rpm$, with full load.

Similarly, only result got at the nominal conditions is verified:

$$i_{RMS(2)} = \frac{\widehat{i}_2}{\sqrt{2}} = 4.91A \approx i_N = 5.0V \tag{3.105}$$

Comparing the voltage and current errors, the current one is visibly higher. The reason of that is due to the assumption made during modelling the system in Chapter 2. The same situation occurs during its validation, presented in section 2.3. Therefore, it is concluded, finally, that designed algorithm acts properly, presenting very good characteristics.

3.7 Summary

The aim of the chapter is presentation of developing the procedure of chosen control algorithm. Analytical discussion shown in Chapter 1, distinguishes stator field oriented control, as the operating strategy. Therefore, brief introduction of the idea hidden behind FOC is described in the beginning. After that, design process begins. It focuses on finding optimal coefficients of PI regulators. It is done with usage of two control criteria: *magnitude optimum*
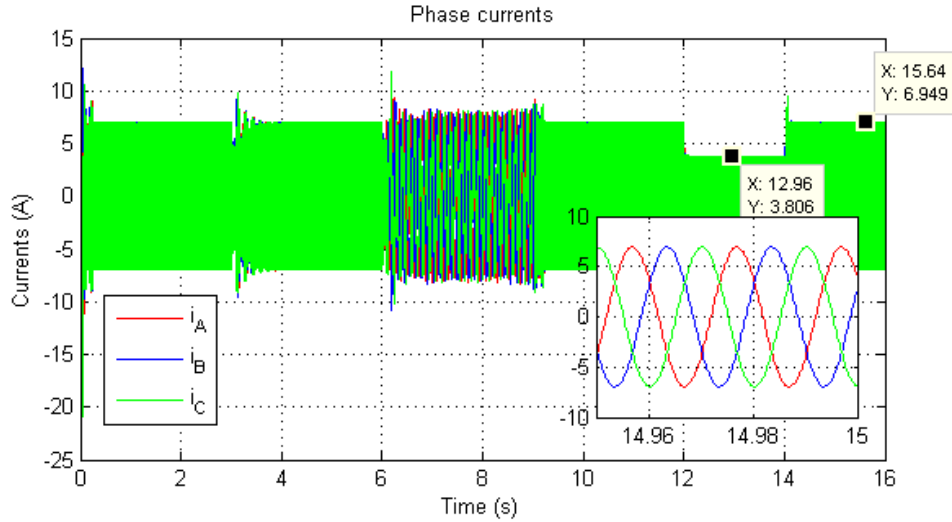
Figure 3.28: *Phase currents changes according to applied test procedure. Two different magnitude values are spotted: $\widehat{i}_1 = 3.806V$ (for $n_r = 1430rpm$, with no load) and $\widehat{i}_2 = 6.949V$ (for $n_r = 1430rpm$, with full load).*

and *symmetric optimum*. Correct choices assure stability of the controlled system, what is proved by tests done in MATLAB/SISOTool package.

Besides, the same theoretical analysis shows strong advantage of sensorless control over the one utilising rotor position sensor. Therefore, two necessary estimators are introduced: for stator flux, and rotor speed. Deeper study on the possible solutions for observing the flux, allows to choose the optimal one: *accurate adaptive integration algorithm (AAIA)* [23]. The fact is, even close-loop SFOC requires precise knowledge about the flux (to execute the strategy properly), while presence of speed estimator is caused only by sensorless demand. Simple velocity observer is designed, and tested afterwards with entire control algorithm.

Eventually, control strategy is implemented on the system derived in Chapter 2. System is run accordingly to the test procedure. Set of plots shows its overall behaviour. Additionally, detailed discussion validates its correctness. Nevertheless, due to the chosen path, control algorithm is precisely designed for the conventional motor available in the lab. Therefore, presented procedure should be applied and verified with the machine operates at higher frequencies.

4

Laboratory Implementation

In order to assure the correctness of obtained conclusions from modelling and simulation process, derived control algorithm has to be tested in the laboratory. Before, the actual experiments can be described, first testbench is introduced. The description is divided into two parts: hardware and software. Afterwards, required tests are presented together with appropriate comments of the results. In the end of the chapter, general conclusion of the laboratory work is drawn.

4.1 Test hardware

In the following section short presentation of the test setup is made. The motor under control is the ABB three-phase induction motor type M2AA100LA loaded with Siemens PMSM type ROTEC 1FT6084-8SH7. Machines are supplied separately. Asynchronous motor is supplied with Danfoss VLT5004 frequency inverter, while synchronous machine with Siemens SIMOVERT MC DC inverter type 6SE7022-6TC51-ZC23. Voltage applied to Siemens inverter is previously rectified by Siemens SIMOVERT MC RRU regenerative rectifier type 6SE7028-6EC85-1AA0. Control algorithm is implemented on the DS1103 controller board based on the Motorola PowerPC 604e/333MHz processor (PPC). All hardware specifications are listed in Appendix C. Overall structure of the testbench is depicted in Fig. 4.1.

All experiments were held in *Flexible Drive System Laboratory* at Aalborg University.

4.2 Test software

The strong advantage of DS1103 PPC system is ability to real-time code execution. That characteristic is obtained with SIMULINK interface, which allows to test developed models directly in the real system. Compiling and downloading procedures are done automatically. Additionally CONTROLDESK provides on-line management of carried out experiments. All the control manipulations are done from the host PC, connected with DS1103 PPC controller, where necessary software is installed.

Next to the derived control algorithm, certain connection with the controller has to be provided. It is done, in MATLAB/SIMULINK, as well, where specific blocks of the interface are used. Additionally, blocks responsible for measurements and protection execution are included. Everything is placed in the data acquisition subsystem *MEASURE & CONTROL*. Its general overview is given in Appendix C.
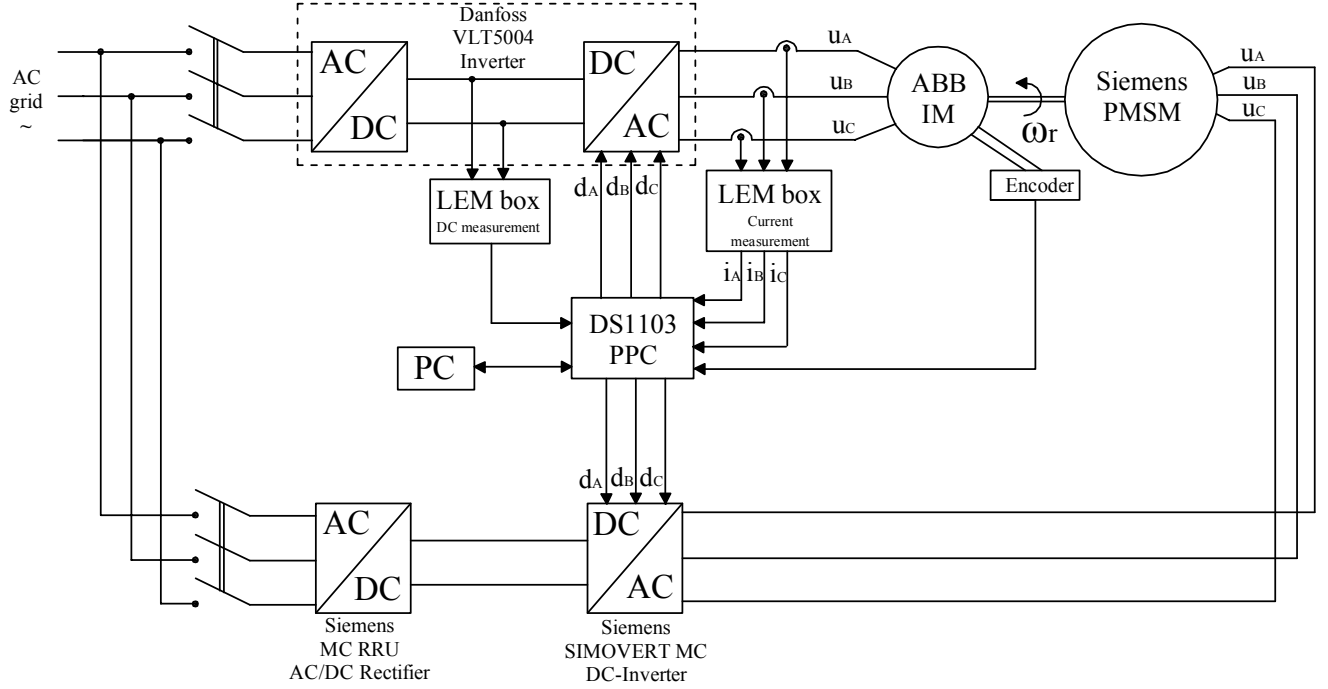
Figure 4.1: *Overall structure of the testbench, mounted in Flexible Drive Systems Laboratory.*

4.3   Experiment results

The purpose of the presented tests is to confirm correctness of the designed algorithm. Scalar control was implemented to observe estimators in open-loop tests, and check their responses. Additionally it is important to mention about the test conditions. Switching frequency was the same as chosen for designing process, $f_{pwm} = 5kHz$. Likewise the acquisition subsystem, space vector modulation strategy was adopted from version available in *Flexible Drive System Laboratory*. Similarly was with the dead-time compensation, which based on the method described in [29]. Machine was run with no load.

As it is mentioned, both, flux and speed estimators were checked in an open-loop test, when motor was run with scalar control. First, observations were focused on the flux observer. Motor was accelerated up to half of rated speed. Naturally, the main objective is to check its capability to run at high speeds. However to compare laboratory tests with simulation results, its speed dependency is also verified. Actual estimated flux is shown in Fig. 4.2.

In the Fig. 4.2, proposed algorithm used for the flux estimation is compared with pure integrator utilisation. Dc drift, due to the imperfection of current measurements, caused the estimation rising. HPF-model overcome that drawback, keeping flux magnitude at the same level. As the scalar control assured constant ratio between applied voltage and frequency, also actual stator flux resulted in constant value. Its magnitude value, given in (3.103). Comparing that to the results from graph in Fig. 4.2, proper flux estimating is deduced.

In addition, observation of the flux loci was done. Their results are depicted in Fig. 4.3. Steady-state shows that loci are enclosed in the circle of unity. It assures that both, real and imaginary components are sinusoidal, shifted to each other by 90°. Additionally,

Figure 4.2: *Comparison of stator flux magnitudes estimations, blue curve represents stator flux obtained with pure integrator, while red one is the flux obtained with proposed algorithm. DC drift, due to the imperfection of current measurements is visible in utilisation of pure integrators. In case of AAIA algorithm, that effect is overcome.*
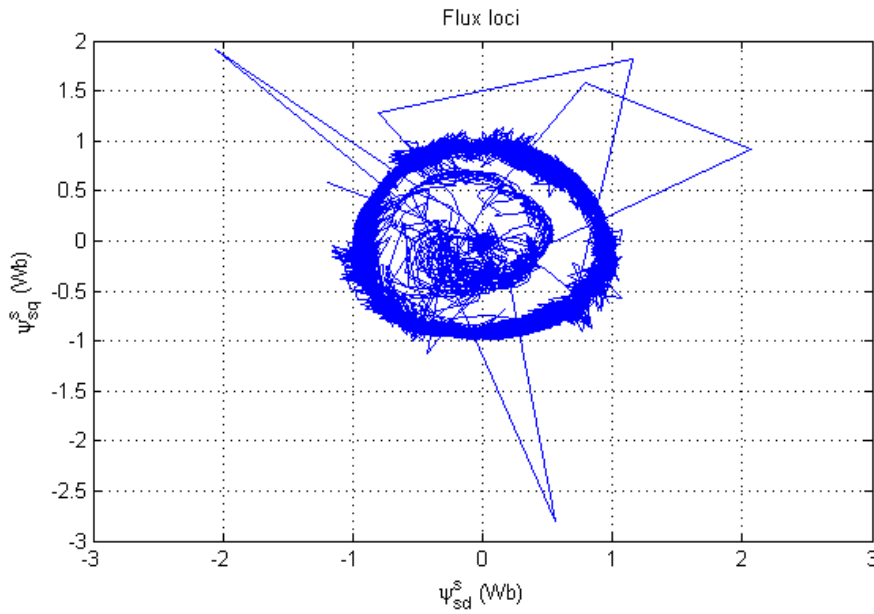
Figure 4.3: *Loci of the stator flux estimation. Steady-state shows that loci is enclosed in the circle of unity. It assures that both, real and imaginary components are sinusoidal, shifted to each other by 90°. Additionally, middle point is placed in the origin, which indicates, that there are no DC components in the estimated values.*

middle point is placed in the origin, which indicates, that there are no dc components in the estimated values. During transient appeared peaks deteriorating the circle. They probably come from the period when the motor was started. Back electromotive force had small magnitude and almost zero frequency. Thus, signals obtained after high-pass filters, were about completely attenuated. It could have resulted in very high gain compensation, according to (3.80), influencing not symmetrically on the flux components. Eventually, motor accelerated, causing the back EMF to rise, and the algorithm to be less sensitive.

Another important objective of the flux observer is to assure correct flux position. Similarly to Fig. 4.2, comparison of the respective angles is presented in Fig. 4.4. Angle obtained from open-loop integration attenuated preventing the control from being appropriate. It is much better visible in the zoom, done in steady-state, where pure integrator case resulted in almost flat estimation.
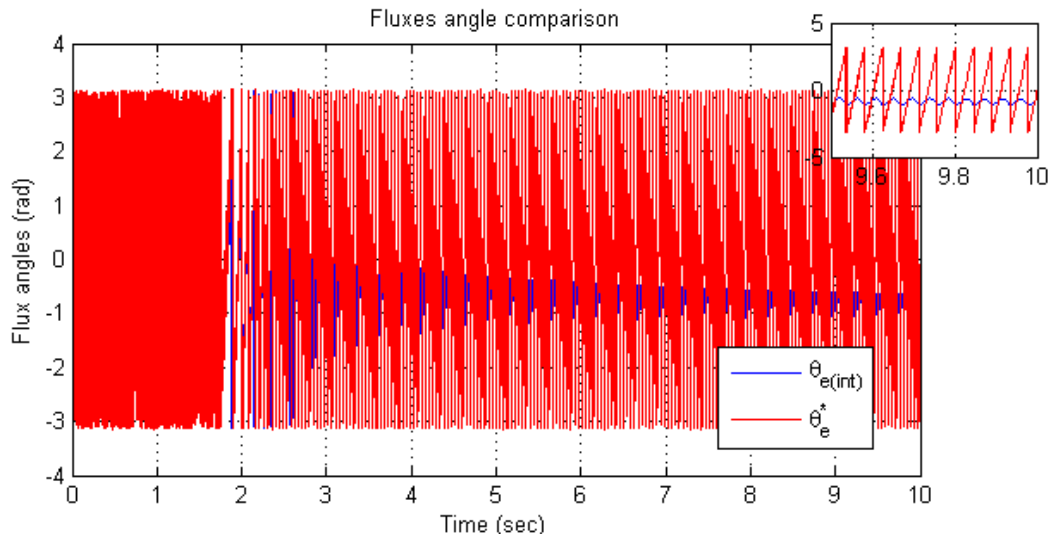
Figure 4.4: *Comparison of stator flux position estimations, blue curve represents flux position obtained with pure integrator, while red one is the position obtained with proposed algorithm. Angle obtained from open-loop integration attenuated preventing the control to be appropriate. Proposed algorithm assured constant position estimation.*

Simulation results of the observer clearly show that it operates much better in higher speed range. In order to check that feature, motor was accelerated up to nominal speed. Angle and magnitude of the flux were improved. Comparisons between that two cases are presented in Fig. 4.5 and Fig. 4.6, respectively. At lower speed (Fig. 4.5-(1)), variation of the angle are noticeable. They vanished at higher speed (Fig. 4.5-(2)), estimation is smoother. In the magnitude estimation, the oscillations were present in both cases, however they were more attenuated when the motor rotated with higher speed (Fig. 4.6-(2)), than with the half of rated velocity (Fig.4.5). The reason of better performance at higher speeds might be caused by reduced sensitivity to stator resistance variations. Since in high speed region, voltage drop on the stator impedance is mainly caused by the frequency-dependant reactance (which does not influence stator flux value), the estimation became more and more independent from the stator resistance. Additionally, higher fundamental frequency of the back EMF, approached closer to the cut-off frequency of HPF, resulting in its lower
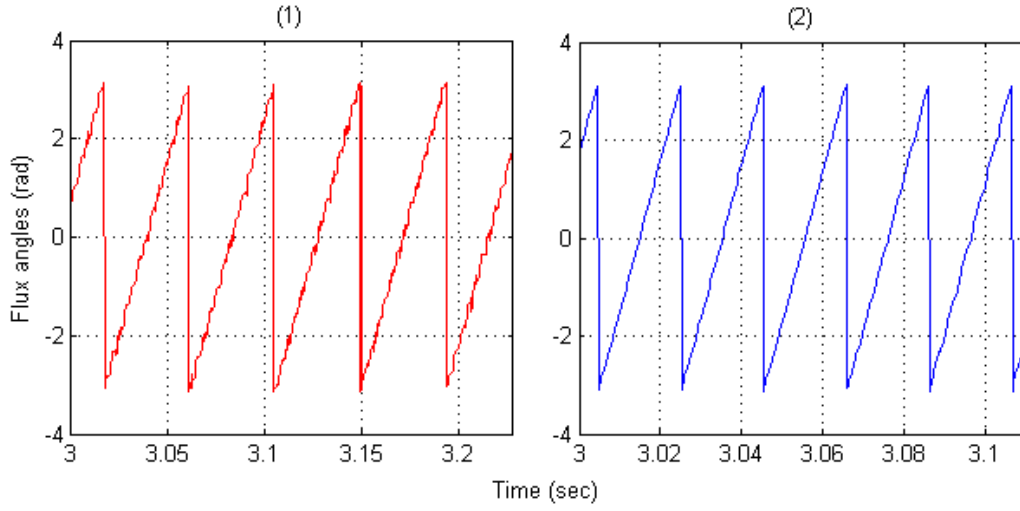
Figure 4.5: *Comparison of stator flux position estimations: (1) - position of the stator flux while motor was rotating with half of the rated speed, (2) - position of the stator flux, when motor was accelerated to the nominal velocity. At lower speed - (1) variation of the angle are noticeable. They vanished at higher speed - (2), estimation is smoother.*
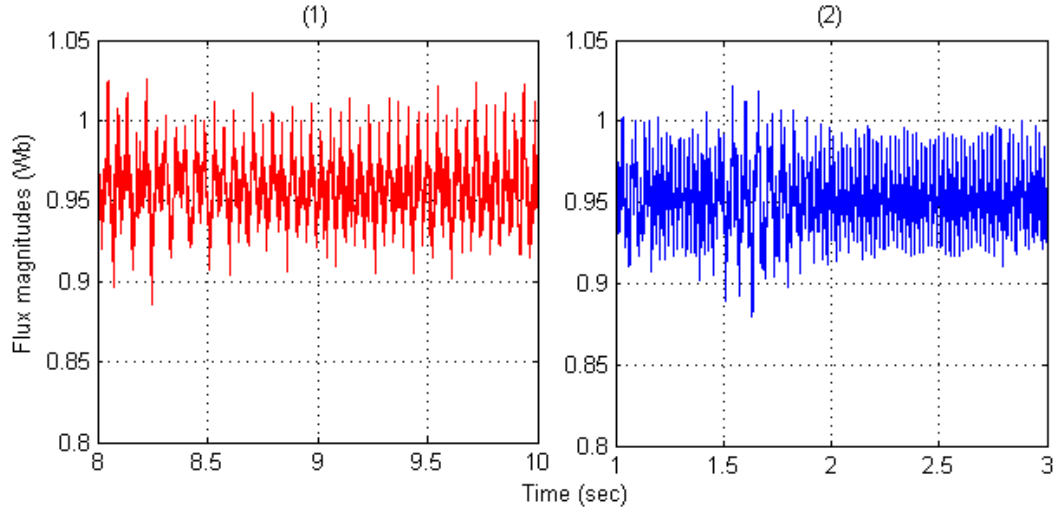
Figure 4.6: *Comparison of stator flux magnitude estimations in steady-states: (1) - magnitude of the stator flux while motor was rotating with half of the rated speed, (2) - magnitude of the stator flux, when motor was accelerated to the nominal velocity. At lower speed - (1) oscillations of the magnitude are noticeably bigger, comparing the results obtained with higher rotational speed (2).*

attenuation. Therefore, gain compensator computation (3.80), which also influences the final position estimation (3.85), varied less (ratio of numerator to denominator in (3.80) was reduced). Hence, it allows to confirm the conclusions obtained during simulations results. Even, if the observer was checked in an open-loop test, its similar behaviour can be expected in a close-loop case.

Speed estimator was validated with single test, when motor was accelerated from zero speed up to $n_r = 1500rpm$, and afterwards speed was decreased down to $n_r = 0rpm$. The result is shown in Fig. 4.7. In the moments of the experiment, when motor started to accelerate or reached again zero speed, negative spikes in estimations are visible. However, as the low speed case is not of the interest, that fact is not examined further. Both, synchronous and rotor speed estimations follow the measurement, during transient and steady-state, as well. In the zoom is visible that estimations oscillate. It might be caused by its dependency on slip and, previously described, flux estimations. To make them smoother, simple digital low-pass filter, with lower cut-off frequency, can be utilised. It shows also, that motor rotates approximately with synchronous speed, as it was operated without load. Open-loop test proved correctness of the speed estimation, therefore its appropriate work in vector control depends on properly tuned regulators.
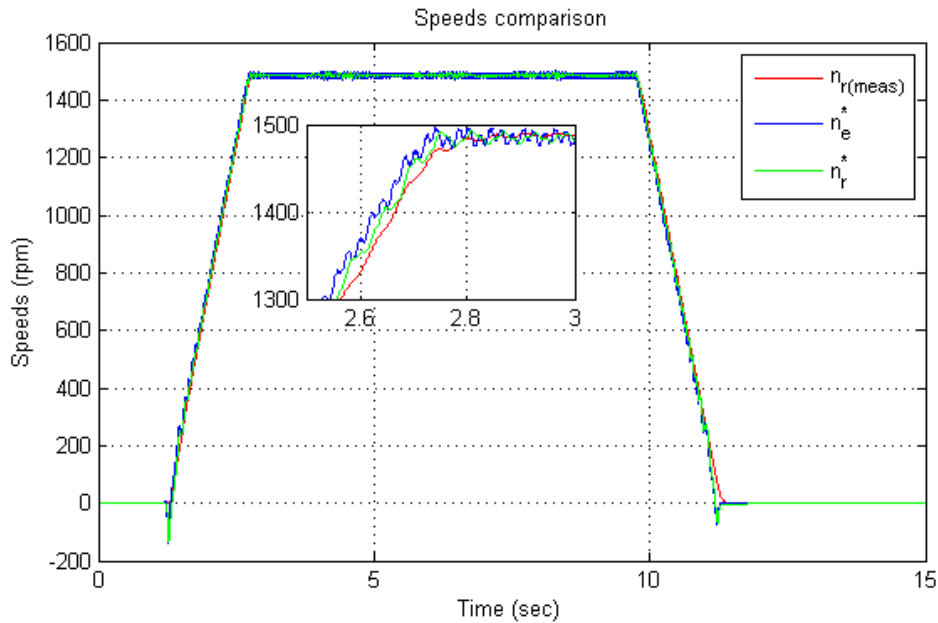
Figure 4.7: *Comparison of speeds, red curve represents rotational speed measured by the encoder, blue represents its estimation, while green one is the estimation of the synchronous speed. Both, synchronous and rotor speed estimations follow the measurement. It shows also, that motor rotates approximately with synchronous speed, as it was operated without load.*

4.4 Summary

General objective of laboratory experiments is evaluation of ideas based on theoretical analysis. Control algorithm derived in Chapter 3, is first checked in the simulation. Afterwards, it

was applied in the real system. Evaluation began with verification of estimators correctness, crucial parts of the chosen control. They were checked in an open-loop test, when the motor was operated with scalar control. Stator flux observer estimation led to similar observation obtained in the simulation. Magnitude remained constant (since scalar control assured, that stator flux is kept constant). Flux angle does not deteriorate with time, changing periodically in constant amplitude range. Additionally, proper observer work was emphasized by comparing it with results obtained from pure integrator, affected by DC offset in current measurements. Similarly to conclusions got from computer simulation, observer tended to present dependence on the actual speed - behaviour improved with risen velocity. Hence, it can be deduced, that similar reaction would be expected in the close-loop test, and even more improved estimation in objective high speed range.

Sensorless control requires proper speed estimation, therefore speed estimator was also verified during laboratory evaluation. Obtained results show its capability of tracking actual rotational speed, during transient and steady-state, as well. However, small oscillations appeared, which might be caused by variations in the flux magnitude estimation (which influences on the synchronous speed estimation), and the slip estimation. However, as it is concluded above, flux observer features become better with increased speed. Hence, improved velocity estimation would be expected, as well.

Nevertheless, due to the limited time, it was not possible to develop more tests in the lab. Therefore, rest parts of the algorithm should be examined further, including tuning PI regulators, running the motor with close-loop (with the advantage of presence of the encoder), and eventually close-loop, sensorless. Then, complete conclusion could be formulated.

5

Conclusions and Future Work

The main objective of the project is to design the stator field oriented control algorithm, capable of running sensorless, and being fully applied in high speed drive. Nevertheless, the lack of availability that kind of motor in university laboratories, has turned the scope into conventional motor supplied with rated frequency $f_N = 50Hz$. In order to fulfil the given goal, it is divided into subtasks.

Before laboratory verification of the algorithm, it is necessary to check its theoretical performance by simulating it with the modelled system. Therefore, the drive is introduced, and validated with previously mentioned conventional motor. Besides, derived motor model can be applied to any asynchronous motor, since set of necessary machine parameters are available. Additionally, ideal representation of the inverter does not depend on any variables, besides the ones obtained during the simulation. Hence, entire system, can be easily adopted in future verification of the objective high frequency drive.

In order to achieve stability in the derived control strategy, utilised PI controllers have to be tuned properly. It is done with usage of two optimal criteria: *magnitude optimum* and *symmetry optimum*. First one is used for parameters selection of current regulators, while the second one for tuning flux and speed controllers. The process ends up with reliable results, fulfilling design conditions. Nevertheless, they are obtained with simplification applied during the process, therefore proper work of the controllers has to validated. It is done with the derived system. Their responses confirm appropriate selection of controllers coefficients.

Another crucial aspect of stator field oriented control is precise knowledge about the flux magnitude and its position. Few reasons determine the necessity: accurate field orientation, further speed estimation, voltage decoupling or utilisation of flux regulator, eventually. After brief survey, appropriate observer is selected. It is verified in simulation, in close-loop system, running sensorless. Obtained results confirm its correctness, since the outputs of the estimator track the actual flux information. Additionally, its dependence on the speed variation is noticeable, the higher the velocity, the better is the performance. In order to validate further the observer, experiment in the laboratory was proceed. It presented similar behaviour, like the one obtained from simulation. Therefore, it can be concluded, that flux estimator is designed accurately. Additionally, its feature allow to expect even better precision with desired high speed range.

Presence of second utilised estimator is caused by the sensorless demand, thus speed estimator is included in the design process. As the objective motor is of an asynchronous type, actual rotational speed depends on two estimations: slip and the synchronous velocity. Furthermore, synchronous speed is derived on basis of flux magnitude estimation. Hence,

that dependency would effect in amplifying errors of previously estimated variables. Thus, speed estimator has to be also validated. Since, simulation runs sensorless, it can be stated, that estimator behaves properly. Additionally, comparison with actual rotational speed is plotted, showing its tracking capabilities. Similarly to flux observer, speed estimator performance was also checked in the laboratory test setup. Obtained results confirmed it correctness. In addition, since speed estimation is dependent on flux observer output, it can be expected, that with risen rotational speed, velocity estimation would be improved, as well.

Nevertheless, due to the time limitation, main goal of the project, could not be fully achieved. All the drawn conclusions based on the presumptions. In order to complete the task, additional tests should be proceeded in the future.

Future Work

Several tests and examination could be included in the future work, improving derived control algorithm:

- Further examination of the designed control strategy. It might contain of retuning PI controllers, tests with motor running in close-loop, first taking advantage of the presence of encoder, and finally sensorless.

- Since the algorithm is fully validated with conventional motor, respective test could be done with objective high speed machine.

- Extension the scope on limitation drawn in section 1.5:

  - Analysis of variation of the motor parameters.
  - Reduction the stator flux in the field weakening region, to extend the speed range.

Bibliography

[1] R. M. Kennel, *Ultra High Speed Drive with Permanent magnet Synchronous Motors and Hardware Based Field Oriented Control*, IEEE

[2] S. Rees, U. Ammann, *Field-oriented Control of Current-Source Inverter fed High Speed Induction Machines using Steady-state Stator Voltages*, SPEEDAM 2006, International Symposium on Power Electronics, Electrical Drives, Automation and Motionp, p. 14-21

[3] Bon-Ho Bae, Seung-Ki Sul, Jeong-Hyeck Kwon, Ji-Seob Byeon, *Implementation of Sensorless Vector Control for Super-High-Speed PMSM of Turbo-Compressor*, IEEE Transactions on Industry Applications, May/June 2003, p. 811-818

[4] L. Xu, C. Wang, *Implementation and Experimental Investigation of Sensorless Control Schemes for PMSM in Super-High Variable Speed Operation*, IEEE, 1998, p. 483-489

[5] A. Arkkio, T. Jokinen, E. Lantto, *Induction and Permanent-Magnet Synchronous machines for High-Speed Applications*, IEEE, p. 871-876

[6] K. Jalili, S. Bernet, M. Malinowski, B. J. Cardoso Filho, *Design and Characteristics of a Rotor Flux Controlled High Speed Induction Motor Drive Applying Two-Level and Three-Level NPC Voltage Source Converters*, IEEE, 2005, p. 1820-1826

[7] M. P. Kaźmierkowski, L. Malesani, *Current Control Techniques for Three-Phase Voltage Source PWM Converters: A Survey*, IEEE Transactions on Industrial Electronics, Vol. 45, No. 5, October 1998, p. 691-703

[8] J. Lähteenmäki, *Design and Voltage Supply of High-Speed Induction Machines*, PhD Thesis, Helsinki University of Technology (Espoo, Finland), 2002

[9] T. L. Andersen, B. S. Henriksen, *Field Oriented Control of Saturated Induction Machine*, student project, 2000

[10] M. Valentini, T. Ofeigsson, A. Raducu, *Control of Variable Speed Variable Pitch Wind Turbine With Full Scale Power Converter*, student project, 2007

[11] G. F. Franklin, J. D. Powell, A. Emami-Naeini, *Feedback Control of Dynamic Systems*, 5-th edition, Pearson Prentice Hall, 2006, ISBN: 0-13-149930-0

[12] P. L. Jansen, R. D. Lorenz, *A Physically Insightful Approach to the Design and Accuracy Assessment of Flux Observers for Field Oriented Induction Machine Drives*, IEEE Transactions on Industry Applications, Vol. 30, No 1, January/February 1994, p. 101-110

[13] J. W. Umland, M. Safiuddin, *Magnitude and Symmetric Optimum Criterion for the Design of Linear Control Systems: What Is It and How Does It Compare with the Others?* IEEE Transaction on Industry Applications, may/june 1990, p. 489-497

[14] R. Bojoi, P. Guglielmi, G. Pellegrino, *Sensorless Stator Field-Oriented Control for Low Cost Induction Motor Drives with Wide Field Weakening Range*, IEEE, 2008, p. 1-7

[15] M. P. Kaźmierkowski, R. Krishnan, F. Blaabjerg, *Control in Power Electronics - Selected Problems*, Academic Press, 2002, ISBN: 0-12-402772-5

[16] J. Holtz, *Pulsewidth Modulation for Electronic Power Conversion*, IEEE, Vol. 82, No. 8, August 1994, p. 1194-1214

[17] M. P. Kaźmierkowski, H. Tunia, *Automatic Control of Converter-Fed Drives*, PWN - Polish Scientific Publishers, 1994, ISBN: 83-01-11228-X

[18] B. Drury, *The Control Techniques Drives and Controls Handbook*, The Institution of Electrical Engineers, London 2001, ISBN: 0-85296-793-4

[19] G. Pellegrino, R. Bojoi, P. Guglielmi, *Performance Comparison of Sensorless Field Oriented Control Techniques for Low Cost Three-Phase Induction Motor Drives*, IEEE, 2007, p. 281-288

[20] M. Kaliamoorthy, S. Himavathi, A. Muthuramalingam, *DSP Based Implementation of High Performance Flux Estimators for Speed Sensorless Induction Motor Drives Using TMS320F2812*, IEEE, Proceedings of India International Conference on Power Electronics 2006, p. 104-109

[21] A. W. F. V. Silveira, D. A. Andrade, C. A. Bissochi, T. S. Tavares, L. C. Gomes, *A Comparative Study Between Three Philosophies of Stator Flux Estimation for Induction Motor Drive*, IEEE, 2007, p. 1171-1176

[22] Myoung-Ho Shin, Dong-Seok Hyun, Soon-Bong Cho, Song-Yul Choe, *An Improved Stator Flux Estimation for Speed Sensorless Stator Flux Orientation Control of Induction Motors*, IEEE Transactions on Power Electronics, Vol. 15, No. 2, March 2000, p. 312-318

[23] M. Zerbo, P. Sicard, A. Ba-Razzouk, *Accurate Adaptive Integration Algorithms for Induction Machine Drive over a Wide Speed Range*, IEEE, 2005, p. 1082-1088

[24] L. Mihalache, *A Flux Estimator for Induction Motor Drives Based on Digital EMF Integration wit Pre- and Post- High Pass Filtering*, 2005, IEEE, p. 713-718

[25] A. Muñoz-García T. A. Lipo, D. W. Novotny, *A New Induction Motor Open-Loop Speed Control Capable of Low Frequency Operation*, IEEE Industry Applications Society, Annual Meeting, New Orleans, Louisiana, October 5-9, 1997, p. 579-586

[26] Kaiyuan Lu, *Control of AC Machines*, lecture slides, Institute of Energy Technology, Aalborg University. *www.iet.aau.dk/ ∼ klu/*

[27] K. Ogata, *Modern Control Engineering*, 4-th edition, Prentice Hall Inc., 2002, ISBN: 978-81-203-2045-1

[28] J. Holtz, *Sensorless Control of Induction Motor Drives*, Proceedings of the IEEE, Vol. 90, No. 8, August 2002, p. 1359-1394

[29] R. Teodorescu, *Gettind Started with dSPACE system*, Aalborg University, Institute of Energy Technology, 2003

A

Init Data

```
% -------------------------------------------------- %
% Initial file for Field Oriented Control Simulation %
% -------------------------------------------------- %
clear all;
clc;

%% Parameters of ABB MT100LA28-4 Induction Motor, ratings:
% 3*380-420/440-480VY, 50/60Hz 2.2/2.5kW, 2 pole pairs

Rs = 3.67;                % Stator electrical resistance
Rr = 2.32;                % Rotor electrical resistance
Lm = 235.0e-3;            % Magnetization inductance
Lsl = 9.2e-3;             % Stator leakage inductance
Ls = Lsl+Lm;              % Stator inductance
Lrl = 12.29e-3;           % Rotor leakage inductance
Lr = Lrl+Lm;              % Rotor inductane
Lst = Ls - (Lm^2/Lr);     % Transient inductance
L_sigma = Ls*Lr-Lm^2;
sigma = 1-(Lm^2/(Ls*Lr));% Dispersion factor
p = 2;                    % Number of pole pairs
pb = p;
Un = 220;                 % Stator nominal voltage
fn = 50;                  % stator frequency
J = 0.0069;               % rotor moment of inertia
B = 0;                    % friction constant (here is neglected...)
Isn = 5.0;                % rated stator current
n_r = 1430;               % rated shaft speed
n = 1500;                 % rated synchronous speed
Ml = 14.6912;             % load torque
cosfi = 0.81;             % power factor of the machine
psi_d_ref = 0.6533;       % calculated reference stator flux
Isd_ref = 4.5359;         % calculated reference d component of the current..
                          % ..(stator flux ref. frame)
Isq_ref = 5.6077;         % calculated reference q component of the current..
                          % ..(stator flux ref. frame)
```

```
k = Ml/1430^2;            % torque constant
k_half=0.5*Ml/1468^2;     % half torque constant

k25 = Ml/667^2;           % torque constant at 25Hz frequency supply

%% Control parameters
%Time constants got from machine characteristics:
Tst = Lst/Rs;             % time constant obtained from stator resistance..
                          % ..and transient inductance
T_s = Ls/Rs;              % stator time constant
Tr = Lr/Rr;               % rotor time constant

%Frequencies & periods
fs = 5000;                % sampling frequency
fpwm = 5000;              % switching frequency
Ts = 1/fs;                % sampling period
Tpwm = 1/fpwm;            % switching period

% Currend i_d inner loop parameters:
T_eq_id_o = 0.5*Ts+Ts+0.5*Ts+0.5*Tpwm;         % equivalent time constant..
                                               % ..of the current open loop
T_eq_id_c = -0.5*Ts+2*T_eq_id_o;               % equivalent time constant..
                                               % ..of the current (entire) loop

% Currend i_q inner loop parameters:
Tiq1 = 10.9e-3;                                % 1st time constant of the plant
Tiq2 = 55.6e-3;                                % 2nd time constant of the plant
T_eq_iq_o = 0.5*Ts+Ts+0.5*Ts+0.5*Tpwm+Tiq1;    % equivalent time constant..
                                               % ..of the current open loop
T_eq_iq_c = -0.5*Ts+2*T_eq_iq_o;               % equivalent time constant..
                                               % ..of the current (entire) loop

% Flux psi_d outer loop parameters:
T_psi_d_plant = L_sigma/(Rr*Ls);               % numerator time constant of the plant
Te_psi_plant = Tr - T_psi_d_plant;             % equivalent time constant of the plant
TeF = Ts + T_eq_id_c;                          % equivalent time constant in flux loop

% Speed outer loop parameters:
Tew = Ts + T_eq_iq_c;                          % equivalent time constant in speed loop
K_eq = (3*p^2*psi_d_ref)/(2*J);                % equivalent constant obtained..
                                               % ..from plant parameters
T_eq_w_o = T_eq_iq_c + Ts;                     % equivalent time constant..
                                               % ..of the speed open loop
T_eq_w_c = 2*T_eq_w_o;                         % equivalent time constant..
                                               % ..of the speed loop (closed)..
                                               % ..used for torque disturbance
                                               % ..input
```

```
% -------------------------------------------------------------------------
% PI regulators are of the forms:
%      1 + tau*s
% K * ---------
%        tau*s
%
% In case of this topology of the controller Kx = Kp_x
% -------------------------------------------------------------------------
% When all parameters of PI regulators are found, they are listed below:

Kp_id = 20.1264;                      % proportional gain of PI id current regulator
Ki_id = 3530.9;                       % integral gain of PI id current regulator
tau_id = 0.0057;                      % integral time constant of PI id reg.
% --- Transfer function: c2d --- %
num_id = [Kp_id*tau_id Kp_id];
den_id = [tau_id 0];
G_id_cont = tf(num_id,den_id);
G_id_d = c2d(G_id_cont,Ts,'tustin');


Kp_iq = 8.4409;                       % proportional gain of PI iq current regulator
Ki_iq = 150.7304;                     % integral gain of PI iq current regulator
tau_iq = 0.056;                       % integral time constant of PI id reg
% --- Transfer function: c2d --- %
num_iq = [Kp_iq*tau_iq Kp_iq];
den_iq = [tau_iq 0];
G_iq_cont = tf(num_iq,den_iq);
G_iq_d = c2d(G_iq_cont,Ts,'tustin');


Kp_psi = 19.3398;                     % propotional gain of PI flux regulator
Ki_psi = 4395.4;                      % integral gain of PI iq current regulator
tau_psi = 0.0044;                     % integral time constant of PI flux reg.
% --- Transfer function: c2d --- %
num_psi = [Kp_psi*tau_psi Kp_psi];
den_psi = [tau_psi 0];
G_psi_cont = tf(num_psi,den_psi);
G_psi_d = c2d(G_psi_cont,Ts,'tustin');


Kp_w = 0.0383;                        % proportional gain of PI speed regulator
Ki_w = 0.4163;                        % integral gain of PI speed regulator
tau_w = 0.0920;                       % integral time constant of PI speed reg.
% --- Transfer function: c2d --- %
num_w = [Kp_w*tau_w Kp_w];
den_w = [tau_w 0];
```

```
G_w_cont = tf(num_w,den_w);
G_w_d = c2d(G_w_cont,Ts,'tustin');

%% dSPACE parameters

I_scaling = 10;                      %current scaling factor;
U_scaling = 1627;                    %dc voltage scaling factor;
enc_lines = 2048;
dt_dz = 0.15;
i_max = 3*Isn;
n_max = fn*60/pb*1.2;
Ud_max = 750;
Ud_min = 100;
```

B

Simulink Models

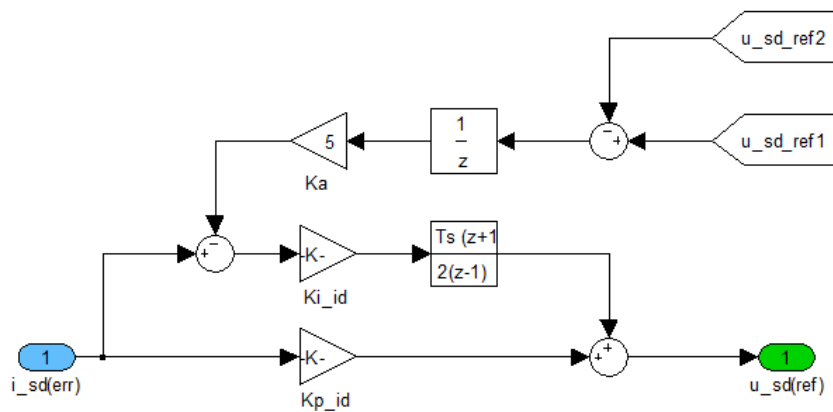Exampled models derived in MATLAB/Simulink environment are presented below.

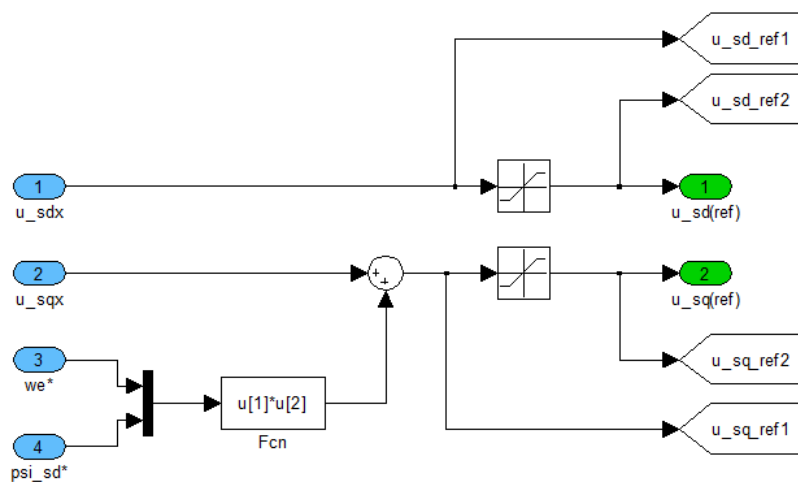**Figure B.1:** *One of the PI controllers - d-current regulator.*

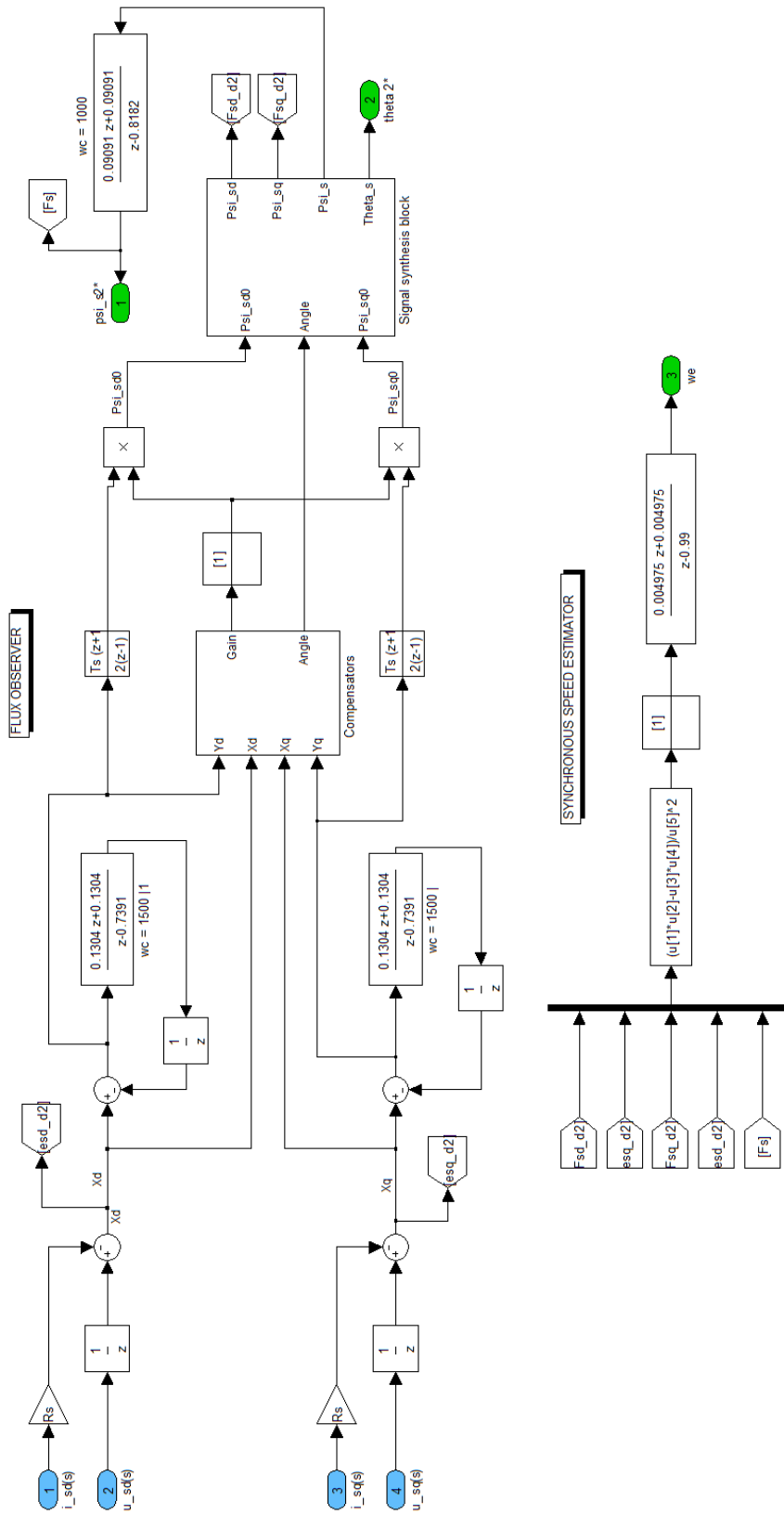**Figure B.2:** *Voltage decoupling.*

Figure B.3: *Flux observer based on AAIA, together with synchronous speed estimation.*
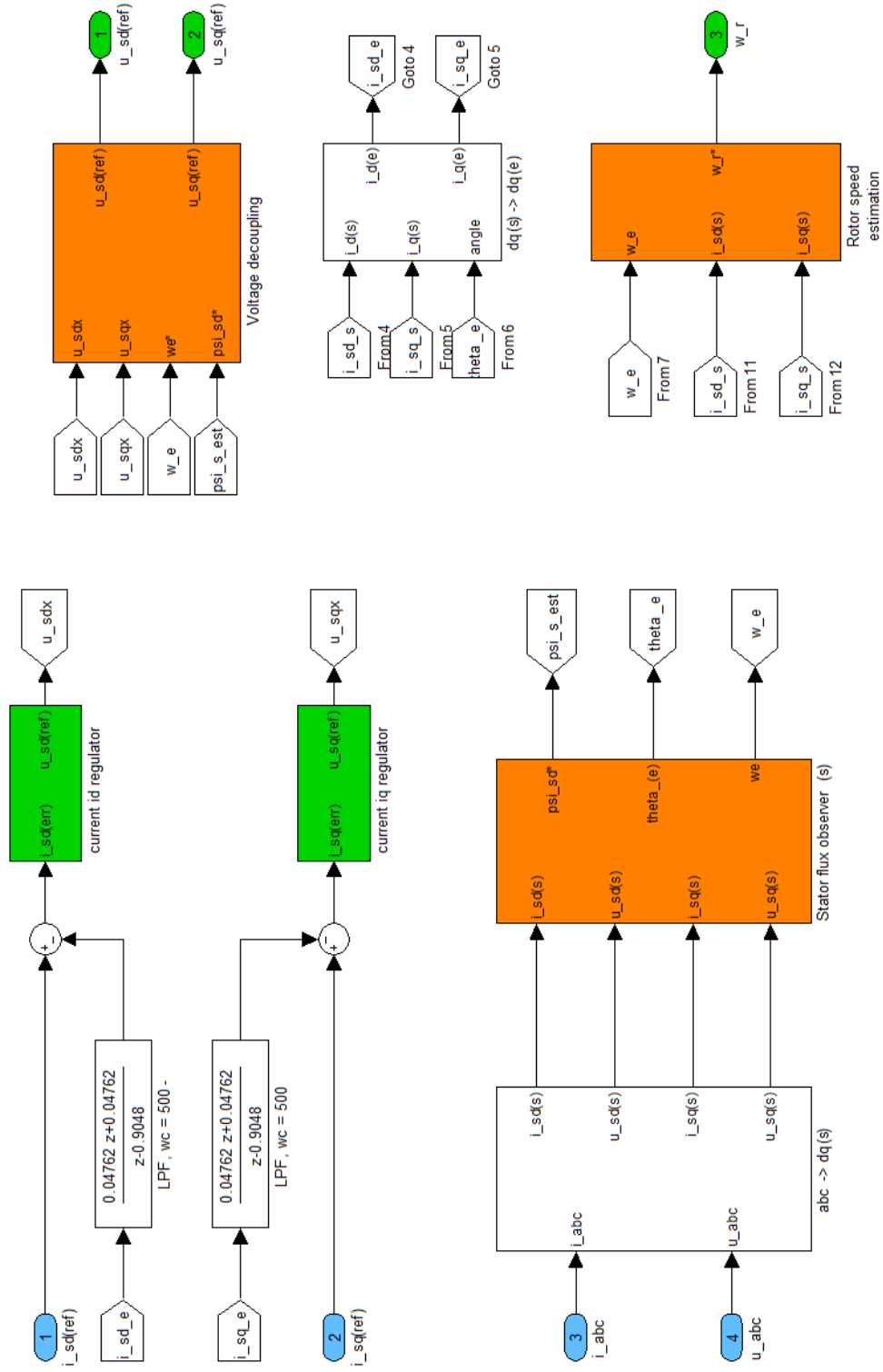
Figure B.4: *Stator field oriented control subsystem. Presentation of current controllers, voltage decoupling, speed and flux estimators.*
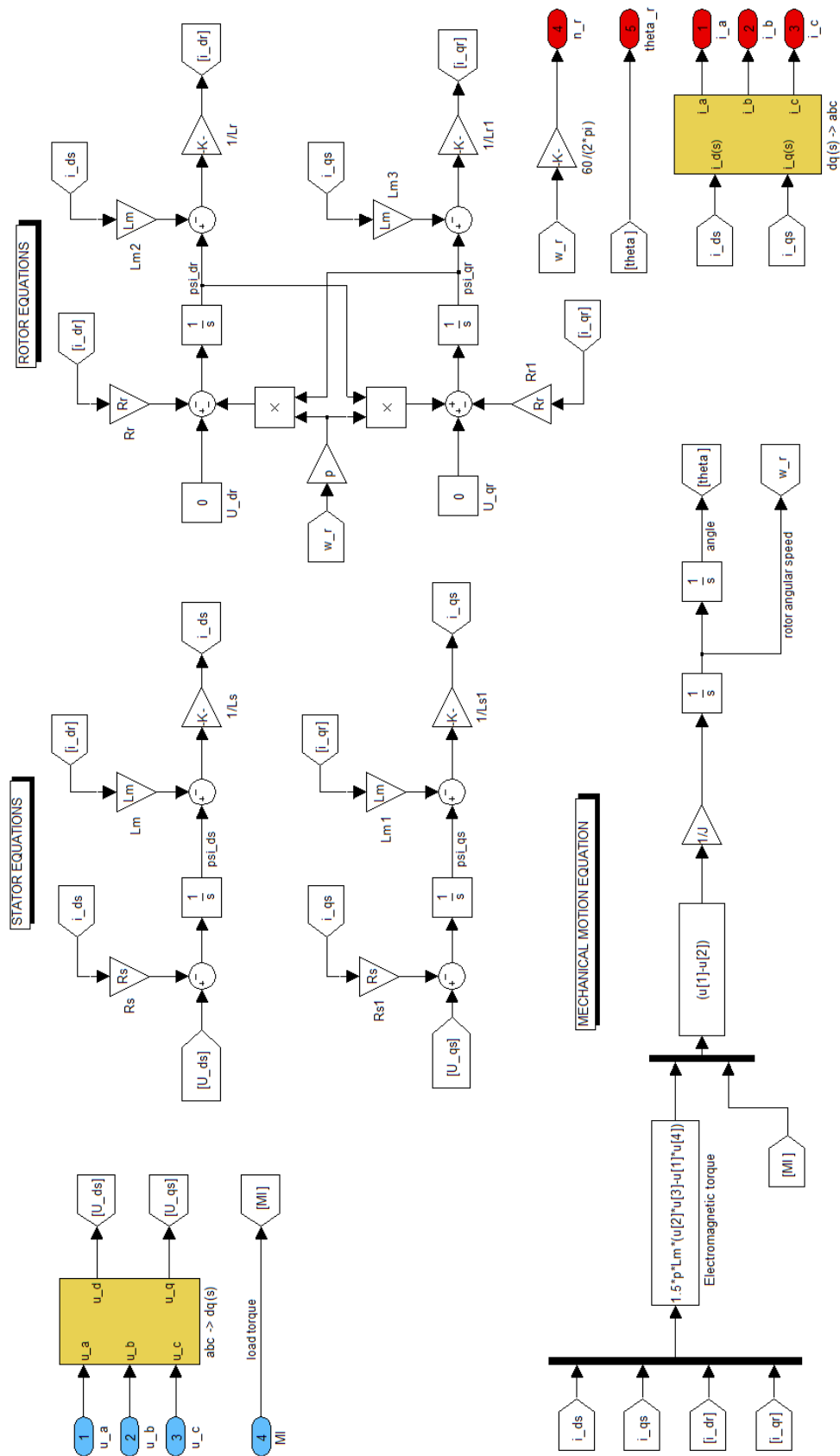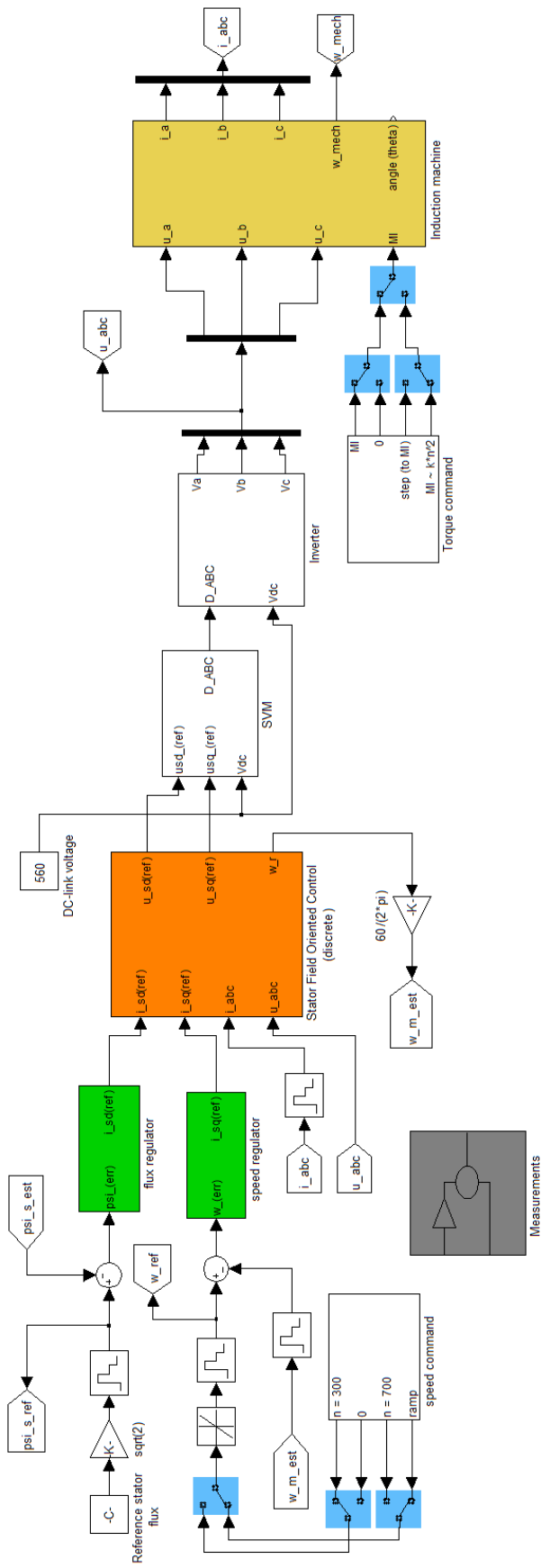
Figure B.5: *Asynchronous motor model.*

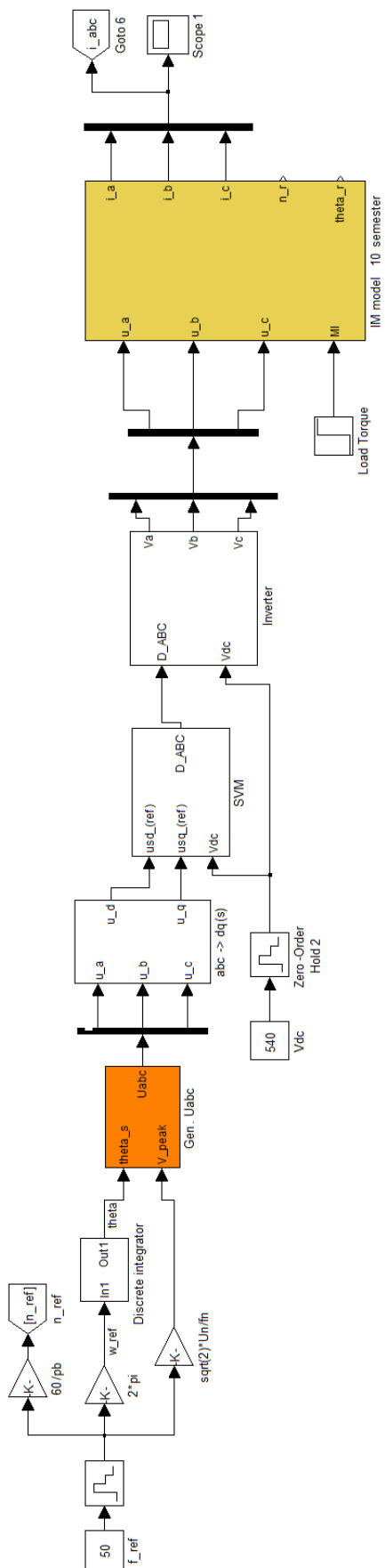**Figure B.6:** *System with field oriented control.*

Figure B.7: *System with scalar control.*

C

Hardware and Software Characteristics

In the following appendix, information about the hardware and software specification, utilised during experiments, are listed [29].

C.1 Hardware

ABB three-phase induction motor type M2AA100LA:

- rated power: $2.2kW$

- rated voltage: $380..420V$ rms (Y)

- rated frequency: $50Hz$

- rated current: $5.0A$ rms

- rated power factor: 0.81

- rated speed: $1430rpm$

Motor is supplied with the Danfoss VLT5004 frequency inverter. Its parameters are given below:

- rated voltage: input = three-phase AC $380V$, output: three-phase AC $380V$

- rated output frequency: $0..132Hz$

- rated current: input = $5.3A$, ouput = $5.6A$

- rated power: $4.3kVA$

- switching frequency: $3..5kHz$

It is loaded with Siemens PMSM type ROTEC 1FT6084-8SH7, which is characterised by the following rated data:

- rated power: $9.4kW$

- rated torque: $20Nm$

- rated current: $24.5A$

- rated frequency: $300Hz$

The load is supplied with Siemens SIMOVERT MC DC inverter type 6SE7022-6TC51-ZC23:

- rated voltage: input = $510..650V$ DC, output = [three-phase AC 0..0.64] x input

- rated output frequency: $0..400Hz$

- rated current: input = $30.4A$ DC, ouput = $25.5A$ rms

- rated power: $16.8..20.3kVA$

- switching frequency: $5..10kHz$

Siemens inverter is previously rectified by Siemens SIMOVERT MC RRU regenerative rectifier type 6SE7028-6EC85-1AA0:

- rated voltage: input = $380..460V$ AC 15%, output = $510..620V$ DC 15% (1.35x input)

- rated current: input = $68A$ DC, ouput = $86A$ DC ($79A$ DC in regeneration mode)

DS1103 PPC Controller Board owns the following characteristics:

- A/D Conversion:

    - 4 parallel A/D-converters, multiplexed to 4 channels each, 16-bit resolution, $4\mu s$ sampling time, $10V$ input voltage range (ADC Unit)
    - 4 parallel A/D-converters with 1 channel each, 12-bit resolution, $800ns$, sampling time $10V$ input voltage range (ADC Unit)
    - 2 parallel A/D converters, multiplexed to 8 channels each, 10-bit resolution, $6\mu s$ sampling time $10V$ input voltage range (Slave DSP ADC Unit)

- Digital I/O:

    - 32-bit input/output, configuration byte-wise (Bit I/O Unit)
    - 19-bit input/output, configuration bit-wise (DSP Bit I/O-Unit providing)

- D/A Conversion: 2 D/A converters with 4 channels each, 14-bit resolution 10 V voltage range

- Incremental Encoder Interface:

    - 1 analog channel with 22/38-bit counter range
    - 1 digital channel with 16/24/32-bit counter range
    - 5 digital channels with 24-bit counter range

- Serial I/O: standard UART interface, alternatively RS-232 or RS-422 mode

- Timers:

    - 32-bit downcounter with interrupt function (Timer A)
    - 32-bit upcounter with pre-scaler and interrupt function
    - 32-bit downcounter with interrupt function (PPC built-in Decrementer)
    - 32/64-bit timebase register (PPC built-in Timebase Counter)

- Timing I/O:

    - 4 PWM outputs accessible for standard Slave DSP PWM Generation

    - 3 x 2 PWM outputs accessible for Slave DSP PWM3 Generation and Slave DSP PWM-SV Generation

    - 4 parallel channels accessible for Slave DSP Frequency Generation

    - 4 parallel channels accessible for Slave DSP Frequency Measurement (F2D) and Slave DSP PWM Analysis (PWM2D)

C.2   Software

Real Time Interface (RTI) for DS1103 PPC Controller Board is designed as an additional library for MATLAB/Simulink. Necessary components assuring proper working and connecting derived algorithm, are placed in *MEASURE & CONTROL* subsystem, created and provided by Aalborg University. Its structure is depicted in Fig. C.1.

The block (Fig. C.1) consists of couple of modules. Each of them is used to ensure, that loaded program and entire application run properly. **Control block** allows enable or disable to start running the inverter. Also if any fault occurs, formula built inside the block results in stopping the converter. **Current Measurement block** gives information about actual currents flow from inverter to the supplied motor. Similarly behaves **DC Link Voltages Measurement block**, provides value of voltage supplied to the inverter. That value is used to create three phase voltages, used to supply the engine. As there is no feedback from voltage sensors, DC voltage is employed as the basis for the algorithm. **Speed Measurement block** uses advantage of encoder mounted on the shaft, giving actual rotational speed. The last subsystem - **SC Protection block** - consists of couple of protections, preventing the system from failing. There are overvoltage, overspeed, shortcircuit and undervoltage protections. If any of these failures occur, it results in generating signal passed to **Control block**, which stops entire system.

Online monitoring and manipulating of the control algorithm is provided by the CONTROLDESK. It also affords capturing data, which later can be visualised and edited in MATLAB.
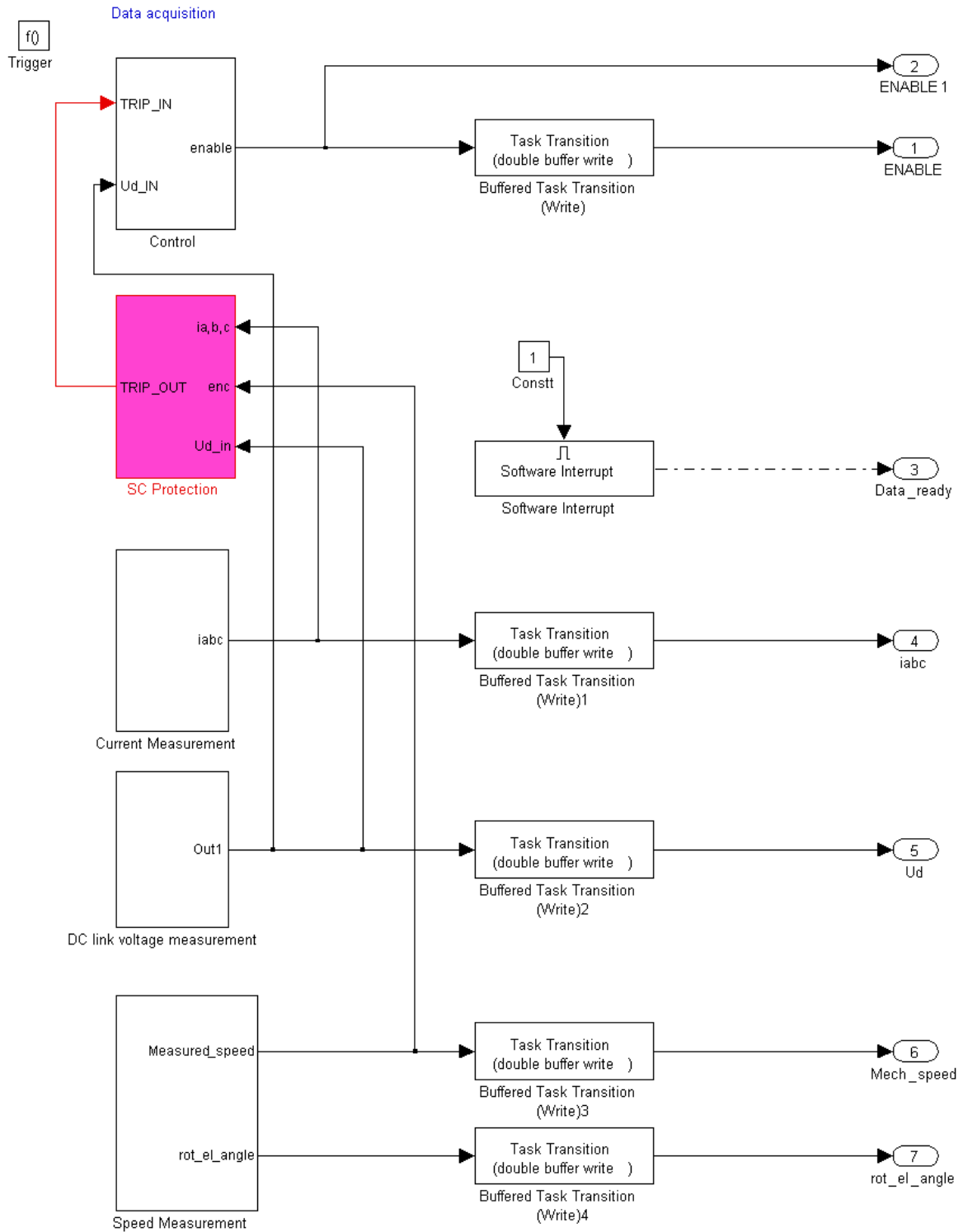
Figure C.1: *Block diagrams represented inside of the MEASURE&CONTROL subsystem.*